Theoretical perspectives on ultrafast and non-linear spectroscopy

Vinas Boström, Emil

2018

Document Version:
Publisher's PDF, also known as Version of record

Theoretical perspectives on ultrafast and non-linear spectroscopy

Theoretical perspectives on ultrafast and non-linear spectroscopy

by Emil Viñas Boström

LUND
UNIVERSITY

Thesis for the degree of Doctor of Philosophy
Thesis advisors: Assoc. Prof. Claudio Verdozzi and Prof. Anders Mikkelsen
Faculty opponent: Prof. Angel Rubio

To be presented, with the permission of the Faculty of Science of Lund University, for public criticism in the Rydberg lecture hall at the Department of Physics on Tuesday, the 5th of June 2018 at 9:00.

Organization
LUND UNIVERSITY

Department of Physics
Box 118
SE–221 00 LUND
Sweden

Document name
DOCTORAL DISSERTATION

Date of defence
2018-06-05

Sponsoring organization

Author(s)
Emil Viñas Boström

Title and subtitle
Theoretical perspectives on ultrafast and non-linear spectroscopy

Abstract
In this thesis we discuss a theoretical description of ultrafast and non-linear spectroscopy. Due to the high intensities and ultrashort pulse durations involved in such experiments, it is necessary to use an explicitly time-dependent formalism. In addition, many of the systems we have considered exhibit strong interactions between the constituent particles, such as electron-electron, electron-nuclear and electron-photon interactions. To properly account for such interactions we have made extensive use of effective models, designed to capture the qualitative aspects of the systems.

The thesis is based on six papers, that can be broadly categorized as follows: In Papers III and VI we study the non-linear interaction of light and matter. In Paper III we look at the multi-photon photo-emission from InAs nanowires, and in particular at the polarization dependence of the photo-emission signal on the crystal structure. In Paper VI we discuss second harmonic generation in a two-level system, and compare the fluorescence spectra from a quantum and semi-classical treatment of radiation.

The remaining four papers are concerned with ultrafast dynamical processes: In Papers I and II we study atomic desorption from a surface, resulting from strong electron-nuclear interactions. To account for these interactions we consider a finite system that can be solved using exact diagonalization. We show that the desorption yield can be controlled by using a protocol with two ultrashort pulses and varying their delay. To assess finite size effects we compare the exact solution of the finite system to an approximate solution of a semi-infinite system based on non-equilibrium Green's functions and Ehrenfest dynamics. In Paper V we study Auger decay in a real-time description, and propose a protocol to induce the quantum Zeno effect by driving the system during decay. The Zeno effect leads to an increase in the Auger lifetime, that is experimentally measurable and can be controlled by varying the intensity of the driving field. In Paper IV we discuss the role of electron-electron interactions for charge-separation in donor-acceptor systems. We identify a regime where the charge-separation is driven solely by electronic correlations, that are captured by treating interactions to first order beyond a mean-field description.

Key words
Non-linear optics, ultrafast dynamics, multi-photon absorption, second harmonic generation, desorption, Auger decay, charge-separation, exact diagonalization, DMRG, DFT, non-equilibrium Green's functions, GKBA, *GW*

Classification system and/or index terms (if any)

Supplementary bibliographical information

Language
English

ISSN and key title

ISBN
978-91-7753-651-2 (print)
978-91-7753-652-9 (pdf)

Recipient's notes

Number of pages
125

Price

Security classification

Theoretical perspectives on ultrafast and non-linear spectroscopy

by Emil Viñas Boström

LUND
UNIVERSITY

A doctoral thesis at a university in Sweden takes either the form of a single, cohesive research study (monograph) or a summary of research papers (compilation thesis), which the doctoral student has written alone or together with one or several other author(s).

In the latter case the thesis consists of two parts. An introductory text puts the research work into context and summarizes the main points of the papers. Then, the research publications themselves are reproduced, together with a description of the individual contributions of the authors. The research papers may either have been already published or are manuscripts at various stages (in press, submitted, or in draft).

Cover illustration front: Schematic illustration of the optical excitation of fullerene C_{60} by an infrared laser pulse (adapted from Paper IV).

Faculty of Science, Department of Physics

ISBN: 978-91-7753-651-2 (print)
ISBN: 978-91-7753-652-9 (pdf)

Printed in Sweden by Media-Tryck, Lund University, Lund 2018

To Mildred and Florinda

Acknowledgements

During my time as a PhD student I have had the great fortune to work with many kind, intelligent and supportive people, to whom I am very grateful. None of this work would have been possible without you, and it has been my true pleasure to work in such a dynamic environment. There are a few people to whom I am especially thankful, and who I want to mention below.

I would first like to express my deepest gratitude to Claudio Verdozzi, who has not only taught me what I know about solid state physics and how to conduct research, but who has always been so generous with his time and let me disturb him with big and small questions. You have helped and supported me with issues both related and unrelated to our work, and taught me a great deal not only about science and theory, but also about music, food, literature and life. In addition, we have had a lot of fun together, both when discussing scientific problems at your blackboard and when telling jokes in your office. I would not be where I am today and know the things I do if it was not for you.

In the same breath I would like to express my warm thanks to Anders Mikkelsen, who has helped and supported me both in our scientific work, and with more practical things such as how to write a grant application. I have learned much from your deep knowledge and your physical insight, as well as your great ability to connect the sometimes abstract work we have done with experimental realizations. I am also thankful for the opportunities you have given me to interact with and learn from other people in your research group, and for the visits I was able to take to the laser lab.

I would also like to thank Carl-Olof Almbladh for his kind interest in my work, and his insights and helpful comments about the problems we have pursued. I have much enjoyed working with you in our recent collaboration, and I appreciate your patience in explaining to me many things which to you must seem trivial. I am also grateful to Ulf von Barth who has always shown an interest in my work, who first taught me about the joys of quantum mechanics when I was a student, and for many interesting scientific discussions. In particular I am grateful to you for introducing me to Claudio, which gave me the opportunity to pursue this PhD.

I would like to extend a deep thank you to Gianluca Stefanucci who welcomed me to come and work with him in Rome. For me this visit was highly rewarding both scientifically and personally, and I am very grateful for the things you have taught me and for getting to know you. The same gratitude goes to Enrico Perfetto both for helping me with my work, and for giving me inside tips about where to find the best pizza in Rome. Thank you both for taking care of me during this time, for our interesting collaboration, and for inspiring me with your genuine interest in physics.

I would like to thank Mathieu Gisselbrecht for his enthusiasm and inspiring interest in physics, and for all the interesting discussions we have had over lunch in relation to our collaboration. I would like to thank Tomas Brage, who has been a great help and support for me when I was a student and went to study abroad, later when I worked as a teaching assistant, and more recently when collaborating on scientific work. A warm thank you goes to Martin Stankovski for taking much of his valuable time to share his knowledge about electronic structure calculations with me, and for being there with support and advice both regarding scientific and personal matters. I want to thank Andrea D'Andrea for our recent collaboration and his insightful scientific comments.

I would also like to thank the fellow PhD students working in our research group: Miroslav Hopjan, Daniel Karlsson and Alexey Kartsev. Thank you for taking me in and helping me to get started when I first came here, and for helping me out with both small and large issues. In particular I would like to thank Miroslav who I have collaborated with on several projects, went on conference trips together with, and who has helped me a lot both with day to day work and with reading and commenting scientific manuscripts. I would also like to thank Pernilla Helmer who has worked with us the last year. I have learned much from our discussions and your curious questions.

Finally a great thanks to all the people working at our division. In particular I would like to thank the people I have shared an office with: Gunnar Eriksson, Fikeraddis Damtie and Tineke van den Berg. We have had much fun together, both at and outside of work, and I feel very lucky to have had the opportunity to meet with you so often. I would also like to thank Peter Samuelsson, Andreas Wacker, Stephanie Reimann, Gillis Carlsson and Ferdi Aryasetiawan for your help and good collaboration during my teaching duties, and for everything I have learned from you during courses, seminars and scientific discussions.

I want to thank Katarina Lindqvist who has always been so kind and helpful: I have enjoyed our coffee breaks and lunchtime discussions, and your warm and happy temper. I would also like to thank Cecilia Jarlskog for her genuin interest in and truly inspiring love for physics. Finally I want to thank Florido Paganelli for all his help over the years, and in particular for his help in saving this thesis.

Slutligen så vill jag tacka mina föräldrar and min familj. Ni har alltid funnits där med hjälp och stöd oavsett hur stora eller små problem jag stött på. Tack mamma och pappa för att ni har lärt mig att värdesätta skola och utbildning, och därigenom inspirerat mig att fortsätta studera. Tack till mina systrar Emma och Amanda för att ni alltid finns där och muntrar upp mig. Tack också till mormor och morfar för att ni alltid har funnits där och stöttat mig, och för den glädje och värme ni sprider omkring er. Jag vill också tacka min svärmor Anna, för din nyfikenhet, din uppmuntran och all din generositet.

Jag vill också tacka mina vänner för att ni finns där med välkomna distraktioner när arbetet blir för mycket. Tack speciellt till Tobias för din entusiasm, din humor och att för att du alltid har tid att prata om stort och smått. Tack också till Lena, både för allt roligt vi haft när vi försökte lära oss fysik tillsammans, och för allt roligt vi fortfarande har.

Tack allra sist till Florinda för att du alltid finns där och står ut med mig. Tack för att du är den du är och för att du både uppmuntrar och utmanar mig. Jag lär mig ständigt nya saker av dig, och jag uppskattar både din humor och din fantastiska intelligens. Jag hade aldrig klarat detta utan dig.

Contents

List of publications

This thesis is based on the following publications, referred to by their Roman numerals:

I **Time-resolved spectroscopy at surfaces and adsorbate dynamics: Insights from a model-system approach**

E. Viñas Boström, A. Mikkelsen and C. Verdozzi
Physical Review **B** 93, 195416 (2016)

We introduce a model to study atomic adsorbates at a surface. The model was used to study photo-induced desorption resulting from strong electron-nuclear interactions. We find that the desorption yield can be controlled by using a two-pulse protocol and varying the delay between the pulses. The change in desorption yield could be attributed to a reduction of the bond kinetic energy due to plasmon screening. To analyze the results in a single-particle picture we constructed a density functional theory for electrons and nuclei, and extracted the exact Kohn-Sham potentials.

Contribution: I developed the part of the code that treat real-space nuclear motion, and performed all the simulations. I did most of the figures, wrote the first draft of the paper, and contributed in the final writing and submission.

II **Nonequilibrium Green's functions and atom-surface dynamics: Simple views from a simple model system**

E. Viñas Boström, M. Hopjan, A. Kartsev, C. Verdozzi and C.-O. Almbladh
Journal of Physics: Conference Series **696**, 012007 (2016)

We combine the non-equilibrium Green's function method with Ehrenfest dynamics, and study atomic desorption from a surface. We benchmark the approximate electronic and nuclear dynamics towards exact results obtained in a finite system. We find that the electronic dynamics is well reproduced by a perturbative treatment, while the Ehrenfest dynamics fail in the description of wavepacket splitting. Using the embedding technique we extend the system to macroscopic size, and compare with the results of the finite system. In the limit of strong adsorbate-surface coupling, we find that finite size effects are small.

Contribution: I performed all simulations for the time-evolution, and did most of the figures. I wrote half of the first draft and contributed in the final writing of the paper.

III **Spatial Control of Multiphoton Electron Excitations in InAs Nanowires by Varying Crystal Phase and Light Polarization**

Erik Mårsell, **E. Viñas Boström**, A. Harth, A. Losquin, C. Guo, Y.-C. Cheng, E. Lorek, S. Lehmann, G. Nylund, M. Stankovski, C. L. Arnold, M. Miranda, K. A. Dick, J. Mauritsson, C. Verdozzi, A. L'Huillier and A. Mikkelsen
Nano letters 18 (2), 907 (2017)

We study multi-photon photo-emission from InAs nanowires grown selectively in the zincblende and wurtzite phase. We find that the polarization dependence of the photo-emission signal in the two crystal phases differ: For the zincblende segment a maximum is found for polarization perpendicular to the nanowire axis, while for the wurtzite segment a maximum is found when the polarization is parallel to the nanowire axis. The behavior of the zincblende segment is explained by a field enhancement due to the nanowire morphology, while the behavior of the wurtzite segment is due to the crystal structure. This is substantiated by DFT and *GW* calculations.

Contribution: I performed the electronic structure calculations and the Wannier interpolation of the dipole matrix elements and energies. I implemented the calculation of absorption rates up to third order. I wrote the first draft of the theory section of the paper, and contributed in the final writing of the paper.

IV **Charge Separation in Donor-C_{60} Complexes with Real-Time Green Functions: The Importance of Nonlocal Correlations**

E. Viñas Boström, A. Mikkelsen, C. Verdozzi, E. Perfetto and G. Stefanucci
Nano letters 18 (2), 785 (2017)

We investigate the role of electron-electron interactions for charge-separation in a prototypical donor-acceptor system. We consider a two-level donor coupled to a C_{60}-molecule described by a Pariser-Parr-Pople Hamiltonian, and compare results from time-dependent Hartree-Fock and non-equilibrium Green's functions within the second Born approximation. We distinguish two regimes where the role of electronic interactions is different: If the donor and acceptor levels are close to resonance, charge-separation can be driven solely by electronic correlation. If the levels are far from resonance, the charge-separation needs to be assisted by nuclear motion.

Contribution: I performed all simulations, and implemented Ehrenfest dynamics to treat the nuclear motion. I wrote the first draft of the paper and contributed to its final writing.

v **Zeno-clocking the Auger decay**

E. Viñas Boström, M. Gisselbrecht, T. Brage, C.-O. Almbladh, A. Mikkelsen and C. Verdozzi
Submitted, arXiv:1804.06605

We study the real-time dynamics of Auger decay in a model atom. We propose a protocol to induce the quantum Zeno effect by driving the system during decay, and show that the lifetime of the Auger decay can be substantially increased. We apply the protocol to atomic Li and hollow Li^+, and find that in these particular systems the lifetimes can be approximately doubled. In the presence of two decay channels of different symmetry, we find that the driving induces entanglement between the separate continua.

Contribution: I wrote the code and performed all simulations. I wrote the first draft of the paper and contributed to its final writing.

vi **Multi-photon effects in a two-level system: A time-dependent study of fluorescence spectra**

E. Viñas Boström, A. D'Andrea and C. Verdozzi
Draft

We study second harmonic generation of a two-level atom in the strong coupling regime. By defining a parity in the coupled electron-photon system we show that second harmonic generation may appear in a non-perturbative treatment, even though it is parity forbidden in perturbation theory. We identify signatures in the fluorescence spectrum of the atom that distinguish a semi-classical treatment of radiation from a quantum treatment.

Contribution: I implemented the electron-photon coupling and performed all simulations. I wrote the first draft of the paper and contributed to its final writing.

List of acronyms

ED	Exact diagonalization
DMRG	Density matrix renormalization group
tDMRG	Time-dependent density matrix renormalization group
DFT	Density functional theory
TDDFT	Time-dependent density functional theory
LDA	Local density approximation
ALDA	Adiabatic local density approximation
NEGF	Non-equilibrium Green's functions
KBE	Kadanoff-Baym equations
GKBA	Generalized Kadanoff-Baym ansatz
2B	Second Born approximation
HF	Hartree-Fock
IR	Infrared
XUV	Extreme ultraviolet
RWA	Rotating wave approximation
SHG	Second harmonic generation
QZE	Quantum Zeno effect
HOMO	Highest occupied molecular orbital
LUMO	Lowest unoccupied molecular orbital
CT	Charge-transfer

Popular summary

Light can be used for many things, from transmitting radio signals and sending information in optical fibers, to lighting up houses and providing energy through solar power. The light to which we as humans are most familiar is the small window of wavelengths between 400 and 700 nanometers (one nanometer is a billionth of a meter), that correspond to all visible colors between violet and red. A way to analyze the composition of light is to let it interact with matter: For example, when white light emitted from the sun or a light bulb passes through a prism, the wavelengths corresponding to different colors are separated from each other and form all the colors of the rainbow. This argument can also be reversed: By shining light on a object, and observing the amount of light that is reflected, transmitted or absorbed, we can learn about the properties of matter. The method of shining light on a material to extract information about its internal structure is called *spectroscopy*, and is the topic of this thesis. Spectroscopic techniques are of large relevance for everyday life, and are used in diverse circumstances such as medicine, chemistry and astronomy.

To understand what information we can obtain using spectroscopic methods, we first discuss some properties of matter. For large objects the properties of a material correspond to a *statistical average* of the properties of the individual particles making up the material. As an example, the current through a system is related to the average velocity of the electrons, and the heat capacity is related to the average energy. The reason why only the statistical properties are important in these materials is because they contain a large number of particles: The typical number of particles in an object of volume 1 cm^3 is around 10^{23} (about one million billion billions), and therefore adding one particle more or less makes no difference. For very small objects, such as atoms and so-called nanostructures, the number of particles is much smaller. Therefore, it is not sufficient to consider only the statistical average of an object, since we must also describe its *statistical fluctuations*. This has the implication that for small objects we can not make definite predictions about the value a measurement of a given property such as the current would return, but only predict the *probability* to measure a certain value.

Another important aspect of nanoscale systems is that the motion of a particle depends strongly on the position of all other particles. Since electrons carry a negative charge, two electrons that come close tend to repel each other. The repulsive interaction makes a description of systems with many electrons much more demanding, since we can no longer describe the motion of each particle separately but have to consider the system as a whole. Therefore, it is often necessary to describe interactions in some approximate way. A common method to do this is to say that a given electron only feels the *average charge* coming from all other electrons, and only try to describe the motion of this particular electron. This approach works well in many circumstances, but also fails in many important cases. A way to partially get around the problem of considering many interacting particles is to

use an *effective* description of matter. This means that we neglect most of the particles in a material, and only try to describe the motion of those particles that are expected to be most important. Usually this means that we miss some aspects of the real system, but with the advantage that the description of the reduced system can be significantly improved.

In the first part of this thesis we will study the effects of interactions between light and matter as a measurement tool to understand the energy structure of matter. For large objects, the energy of a system is a continuous variable, meaning that it can take any value in a given interval. As it turns out, this is no longer true for small objects, where the energy can only take specific *discrete* values. This effect is known as *quantization*, and comes from the fact that particles confined to a small volume start to behave like waves. The most famous example of quantum effects is Bohr's model of an atom, where the electrons can only orbit the nucleus at a set of fixed distances. This has the consequence that the energy required to move an electron from one orbit to another has a specific value, and therefore the atom can only absorb energy corresponding to these quanta of energy. The energy difference between different orbitals can be found by shining light on the atom, and measuring which wavelengths are absorbed. We have considered a similar experiment where the atom is replaced by a so-called nanowire, to extract information about its energy levels.

In addition to giving information about an object, light can be used to initiate time-dependent processes in a material. Much like the signal from a remote control is used to active a television, short pulses of light can be used to start atomic processes. Although conceptually similar, the time-scales on which these processes occur are very different, and the typical time it takes for an electron to move inside a material is around one femtosecond (a millionth billionth of a second). To study processes on this time-scale is therefore very demanding, and only recently has the necessary technology been developed. One method to investigate the fast electronic motion is by shining two or more pulses of light on a material. A way to think of this method is that the first pulse gives a kick to the system that forces it to react, while the second pulse takes a snapshot of the instantaneous configuration. If the time between the two pulses is varied, these snapshots can be added one after another like the frames of movie, which allows us to observe in real-time how the system evolves.

By observing and understanding the electronic motion we can also hope to control it. In this thesis we have attempted to control very fast processes, where for example an atom initially stuck to a surface is released, or a decaying atom is hindered from doing so. We have also studied the factors contributing to an efficient conversion of light energy to electric currents in a model solar cell. Even though these results may not be directly applicable in a technological context at the moment, manipulating such basic processes is a first step towards a more complete control of fast electronic dynamics. In the future the control of electronic and atomic motion can hopefully be used to construct faster electronic components, enhance chemical reactions, and improve the efficiency of solar cells.

Populärvetenskaplig sammanfattning

Ljus kan användas till många saker, allt från att sända radiosignaler och skicka information i optiska fibrer, till att lysa upp hem och utvinna energi via solceller. Det ljus vi är mest vana vid som människor är ett intervall av våglängder mellan 400 och 700 nanometer (en nanometer är en miljarddels meter), som svarar mot alla synliga färger mellan rött och violett. Ett sätt att undersöka sammansättningen hos ljus är genom att låta det växelverka med materia: När vitt ljus exemplvis från solen passerar genom ett prisma, bryts de våglängder som svarar mot olika färger ut från varandra och bildar alla regnbågens färger. På motsvarande sätt kan vi genom att belysa ett föremål få information om materiens egenskaper, genom att mäta den andel av ljuset som reflekteras, transmitteras eller absorberas. Den typ av experiment som använder ljus för att extrahera information om ett föremåls interna struktur kallas för *spektroskopi*, och är ämnet för denna avhandling. Spektroskopiska tekniker är viktiga för många områden i vårt vardagsliv, och används i vitt skilda sammanhang såsom inom medicin, kemi och astronomi.

För att bättre förstå den information vi kan få via spektroskopiska metoder, ger vi först en kort bakgrund till ett antal egenskaper hos materien. För stora föremål svarar egenskaperna hos ett material mot det *statistiska medelvärdet* av egenskaperna hos de partiklar som materialet består av. Exempelvis är den elektriska ström som passerar genom ett system relaterad till medelhastigheten hos elektronerna. Anledningen till varför endast de statistiska egenskaperna är viktiga i stora föremål är att de består av ett stort antal partiklar: Det typiska antalet partiklar i ett föremål av storleken 1 cm^3 är omkring 10^{23} (cirka en miljon miljarders miljarder), och det gör därför ingen skillnad med en partikel mer eller mindre. För väldigt små föremål, såsom atomer och så kallade nanostrukturer, är antalet partiklar mycket mindre. I sådana material är det därför inte tillräckligt att bara bekymra sig om en egenskaps statistiska medelvärde, utan vi måste också beskriva dess *statistiska fluktuationer*. Detta medför att vi för små föremål inte kan göra definitiva förutsägelser om resultatet av en mätning (av exempelvis en egenskap som den elektriska strömmen), vi kan bara förutsäga *sannolikheten* att mäta ett givet värde.

En ytterligare egenskap hos nanosystem är att rörelsen hos en given partikel är starkt beroende av positionen hos alla de andra partiklarna. Eftersom elektroner har negativ elektrisk laddning, så kommer två elektroner som är nära varandra att repellera varandra. Då vi inte längre kan betrakta rörelsen hos varje enskild elektron som oberoende av de andra, måste vi istället betrakta systemet som en sammansatt helhet. Den repulsiva växelverkan gör det därför betydligt svårare att behandla ett system med många elektroner, och det är därför vanligt att använda en approximativ beskrivning av växelverkan. En vanlig approximativ metod är att anta att en given elektron bara känner av *medelvärdet* av laddningen från de övriga elektronerna, och därefter endast beskriva rörelsen hos den enskilda elektronen. Detta förhållningssätt fungerar bra för många system, men misslyckas också i många viktiga fall.

Ett annat sätt att komma runt problemet att beskriva växelverkande partiklar kan då vara att använda en *effektiv* beskrivning av systemet. Det innebär att vi ignorerar de flesta partiklarna i materialet, och endast försöker beskriva rörelsen hos de partiklar som förväntas vara viktigast för en given process. I praktiken innebär detta att vi utelämnar vissa aspekter hos det ursprungliga systemet, men det har fördelen att det reducerade systemet kan beskrivas mer detaljerat.

I den första delen av denna avhandling betraktar vi växelverkan mellan ljus och materia som ett verktyg för att förstå ett föremåls energistruktur. För stora föremål är systemets energi en kontinuerlig variabel, vilket innebär att den kan ta vilket värde som helst i ett givet intervall. Det visar sig att för små föremål är detta inte längre fallet, och i sådana system kan energin istället bara anta vissa *diskreta* värden. Denna effekt kallas *kvantisering*, och har sitt ursprung i det faktum att partiklar som stängs in i en liten volym börjar att bete sig som vågor. Det mest kända exemplet på sådana kvanteffekter är Bohrs atommodell, där en elektrons banrörelse kring atomkärnan endast kan ske på vissa specifika avstånd från kärnan. Detta medför i sin tur att energin som krävs för att flytta en elektron från en bana till en annan har ett givet specifikt värde, och att atomen därmed bara kan absorbera ljus med en energi som svarar mot dessa specifika värden. Energiskillnaden mellan olika elektronbanor kan mätas genom att belysa atomen, och undersöka vilka väglängder av ljuset som absorberas. Vi har studerat ett liknande exempel, där atomen bytts ut mot en så kallad nanotråd, för att på så vis kunna extrahera information om nanotrådens energistruktur.

Utöver att ge information om ett föremål, så kan ljus användas för att initiera tidsberoende processer i ett material. På samma sätt som signalen från en fjärrkontroll används för att sätta på en TV, kan korta ljuspulser användas för att sätta igång atomära processer. Trots sina likheter så sker dessa processer på väldigt olika tidsskalor, då den typiska tiden det tar för en elektron att förflytta sig inuti ett material är omkring en femtosekund (en miljondels mijarddel av en sekund). Att studera atomära processer är därför väldigt komplicerat, och den teknologi som krävs för att göra det har inte utvecklats förrän nyligen. En metod för att undersöka elektroners rörelse är genom att belysa ett material med två eller flera ljuspulser. Vi kan förstå hur denna metod fungerar genom att betrakta den första pulsen som en knuff, vilken tvingar systemet att röra och anpassa sig, och den andra pulsen som en kamera som tar en ögonblicksbild av systemets konfiguration. Genom att variera tiden mellan de två pulserna får vi en mängd sådana bilder, vilka kan läggas efter varandra som bildrutorna i en film så att vi kan betrakta systemets utveckling i realtid.

Genom att observera och förstå hur elektroner rör sig, är förhoppningen att vi ska kunna kontrollera deras rörelse. I den här avhandlingen har vi försökt att kontrollera ett antal mycket snabba processer, där exempelvis en atom adsorberad vid en yta lossnar, eller en atom hindras från att sönderfalla. Vi har också undersökt vilka faktorer som bidrar till en snabb omvandling av ljusenergi till elektrisk energi i en prototypisk solcell. Även om dessa resultat för tillfället inte kan tillämpas direkt i en teknologisk eller industriell kontext, så

är möjligheten att manipulera sådana grundläggande processer ett första steg mot en mer fullskalig kontroll av elektroners dynamik. I framtiden kan kontroll av elektroniska och atomära processer förhoppningsvis användas för att konstruera snabbare elektriska komponenter, snabba på kemiska reaktioner, och förbättra effektiviteten hos solceller.

Chapter 1

Introduction

Physics is an empirical science, and as such, it relies on the comparison of measurements and theoretical predictions. In a conceptual sense, we can say that physics proceeds in the following manner: Starting from a few basic axioms, we propose an hypothesis that can be either verified or falsified by a measurement. If the statement is falsified it is rejected, while if verified it is taken as the basis for new hypotheses. By progressing in this manner the valid hypotheses form an increasingly intricate theory that can ultimately be applied to explain a vast range of experiments.

A more pragmatic perspective on the physical science is one of control: By understanding the working principles of matter, we can design objects and materials that behave in a predetermined manner. As our knowledge of the physical world grows, we can construct more and more advanced technologies that can help benefit our daily life. Of this we see examples everywhere, from trains and airplanes relying on the principles of classical mechanics and electrodynamics, to light emitting diodes and solar harvesting materials that work according to the principles of quantum mechanics. As time progresses the branches of physics move towards increased maturity, where understanding of new processes go hand in hand with their control and application. In light of this, we start by addressing three fundamental questions: Firstly, what are the measurements and physical processes we aim at describing? Secondly, what are the theoretical challenges in trying to do so? And finally, how can these processes be controlled and used in technological applications?

This thesis is concerned with the class of measurements known as spectroscopies. By this we mean experiments where an external electromagnetic wave is used to excite a system, and information about the system is acquired by recording either the outgoing electromagnetic field or some emitted particles. In many contexts, it is possible to a good degree to assume that the field is so weak that it will only cause a small disturbance in the sample. Under such

conditions a description of the process becomes significantly simpler, since it is possible to describe the coupled system through perturbation theory. A special case is the theory of linear response, where the perturbing field is treated only to lowest (linear) order.

In the linear regime the electromagnetic wave can be seen as a probe of the energy structure of the system. As an example, consider an atom in its ground state. If subjected to monochromatic light of frequency ω, it can change its internal state by absorbing energy from the field. This is however only possible if the frequency of the field matches the difference in energy between two atomic energy states. By recording the spectral energy density of the electromagnetic field after its interaction with the system, we can define the absorbed energy per frequency $s(\omega)$. This type of experiment is known as photo-absorption (PA) spectroscopy, and gives direct information about the atomic states through the transition energies encoded in $s(\omega)$. A similar way to probe a system, commonly used for solid state materials, is to subject the system to electromagnetic radiation and measure the energy of the emitted electrons. In this case the final state will consist of a free electron with momentum $\mathbf{k}$, and an ionized system with one electron removed. By measuring the energy $s(\omega, \mathbf{k})$ of the photo-electron, in an experiment known as angle-resolved photo-electron spectroscopy (ARPES), we get information about the momentum resolved energy structure of the sample.

For traditional continuous wave lasers the theoretical predictions obtained from linear response is often in good agreement with the experimental results. However, for experiments performed using intense *pulsed* lasers the instantaneous field strength of the electromagnetic wave is many times of the same order as the binding energies of atomic and solid state systems. Under such conditions it is necessary to take into account the non-linear effects of light-matter interactions, such as wave mixing, multi-photon absorption and high harmonic generation. For even stronger fields, where the field strength becomes comparable with the characteristic energy scales of the sample, it is also necessary to take explicitly into account the renormalization of material properties due to the presence of the field. With present technologies it is possible to create pulses with a duration ranging from ps to as, and photon energies from 1 eV to more than a hundred eV.

Using pulsed lasers it is also possible to study the time-evolution of a system resulting from external perturbations. Examples of such dynamical processes is the time-dependent current through the system, or the motion of electrons and nuclei in a solid material. In macroscopic systems it is typically possible to distinguish between two regimes of the time-evolution: At early times, shortly after the perturbation is switched on, the system responds in an oscillatory fashion. This is commonly referred to as the *transient* regime. At later times the oscillations are damped away due to dissipation in the material, and the system reaches the *steady state* regime. The duration of the transient regime is dependent on the mechanisms responsible for dissipation, and can be estimated from the typical energy scale of the relevant process. For electrons the typical energy ϵ_e is on the order of electron volts,

giving a characteristic time scale of $\tau_e \sim \hbar/\epsilon_e$ of femtoseconds. Correspondingly, the typical energy ϵ_n of nuclear vibrations (phonons) is meV, giving a characteristic time τ_n on the order of picoseconds.

Today it is possible to realize laser pulses with durations on the attosecond time-scale, which can be used as instantaneous probes of a dynamic electronic system. One common method for this is the so-called pump-probe scheme, which consists of an intense pump pulse exciting the system and a weaker probe pulse that performs a PA measurement. In experiments the delay τ between the pump and the probe is varied, and the probe field is measured. This signal contains contributions from dipole oscillations in the sample, which encode information about the current state of the system. By forming the difference of the probe signals with and without the pump field present, we can construct a spectrum of differential absorption that gives information about which states are populated by the pump and how these populations evolve in time. In this way, it is possible to directly measure the properties of an excited system.

A theory of ultrafast and non-linear spectroscopy needs to deal simultaneously with the time-dependence and non-linear features of the electromagnetic field. For systems in equilibrium, it is often possible to use a description based on perturbation theory, while for non-equilibrium problems the time-dependence of the field needs to be explicitly accounted for. In addition, there are two aspects of the system itself that may complicate a theoretical description, namely the size of the system and the presence of internal particle-particle interactions. For systems with weak interactions the problem can often be adequately described in an effective single-particle picture, where the interactions are taken into account in an approximate manner. This is beneficial, since the effort needed to solve a single-particle problem scales linearly with the system size. In this thesis we have considered two such methods, namely density functional theory (DFT) and the non-equilibrium Green's function (NEGF) method. For stronger interactions the motion of each particle is dependent on the position of every other particle, and an independent particle description is no longer valid. Under such circumstances, it is preferable to use a method that includes interactions in a non-perturbative way. To treat strongly interacting systems we have used two numerically exact methods, the exact diagonalization (ED) and density matrix renormalization group (DMRG) method. Although exact, these methods are of more limited scope than DFT and NEGF, as will be discussed in detail in the next chapter.

To theoretically describe a system we first need to determine the equations governing its dynamics. To this end we have considered two conceptually different approaches. The first is the so-called *ab initio* approach, where the idea is to base the description on an equation of motion taking explicit account of all constituent particles of the material. In this way, all physical processes of the system are contained in the descrption, and very little is assumed about the details of the system before a calculation is performed. The second approach to describe a system is to formulate a set of effective equations for the most relevant degrees

of freedom. We will refer to this as a model approach, since it only aims at describing the qualitative features of a system. Although this approach is more limited in scope than the *ab initio* theories, it many times offers a greater conceptual clarity. In addition, since the effective equations are determined by a small number of parameters, it is easier to identify the key mechanisms behind a process. Inherent in this approach is that we do not aim to make detailed predictions about specific physical systems, but instead we focus on the general aspects of a given physical process.

In this thesis we look at some conceptual questions relevant to the fields of non-linear and ultrafast spectroscopy. A first major topic is the role of strong interactions: In many of the systems we have studied, the dynamics are driven by interactions between different particle species. In Paper I, we study atomic desorption from a surface, which is induced by electron-nuclear interactions. In Paper IV, we look at the role of electron-electron interactions for charge-transfer in a prototypical donor-acceptor system, and in Paper VI we discuss second harmonic generation in a two-level system with strong electron-photon interactions.

Another key topic is the control of dynamical processes, which is discussed in a number of different contexts: In Papers I and II we show that subjecting an adsorbed atom to external laser pulses can induce desorption, and in particular that the desorption yield can be controlled by using two pulses with varying delay. In Paper III we investigate the non-linear photo-emission signal from InAs nanowires. We found that the signal depends both on the crystal phase of the material and on the polarization of the incident field, which allows for a spatial control of the non-linear response by varying the crystal structure or the polarization. In Paper V we study the Auger effect of an isolated atom, and show that the lifetime of the process can be controlled by inducing the quantum Zeno effect. This is interesting since it in principle allows for very fast processes to be studied on an artificially longer time-scale.

Finally, we mention a few practical applications: The desorption process is of technological importance since it appears in many catalytic devices. However, in a more general sense it corresponds to the breaking an interatomic bond, and could therefore be of relevance also to photo-switches in molecular systems. The charge-transfer process is of high relevance since it constitutes the initial step of any light-harvesting device. To understand this process is important to identify suitable materials for solar devices. Systems where charge-separation is driven by electron correlation could also be of particular interest, since they are expected to relax faster than systems driven by nuclear effects.

The thesis is organized as follows: In the two initial chapters (2 and 3) we give an introduction and background to the theoretical frameworks used in the papers, with the aim of being reasonably self-contained while not including too much detail. The following two chapters (4 and 5) give an introduction to the physical processes studied in the papers. In chapter 6 we summarize the main results and discuss some possible routes of further research.

Chapter 2

Wavefunction based methods

To make theoretical predictions about a physical system we need to formulate a set of equations governing its dynamics, and use their solution to extract some information of interest. In the low-energy regime of atomic, nanoscale and solid state systems, the fundamental equation of motion is the many-body Schrödinger equation, and the result of its solution the many-particle state vector. We start this chapter by discussing two numerically exact ways of solving the many-body Schrödinger equation, namely the exact diagonalization (ED) method (Sec. 2.1) and the density matrix renormalization group (DMRG) method (Sec. 2.2). Both these methods are limited in scope by an unfortunate scaling of the computational effort either with the system size (in the case of ED), or with the system dimension (in the case of DMRG). However, when applicable, they give the exact solution of the Schrödinger equation. We then introduce density functional theory (Sec. 2.3), which reformulates the many-body problem in terms of an effective one-particle theory and allows us to address larger systems. Although exact in principle, the performance of this theory depends crucially on a quantity known as the exchange-correlation potential, which in practice has to be approximated. In the final section (Sec. 2.4), we derive and discuss the semi-classical Ehrenfest approximation.

2.1 Exact diagonalization

The many-body Schrödinger equation is easy to write down but tricky to solve. Given a Hamiltonian $H(t)$ it reads (in units where $\hbar = 1$)

$$i\frac{\partial}{\partial t}|\Psi(t)\rangle = H(t)|\Psi(t)\rangle, \tag{2.1}$$

where $|\Psi(t)\rangle$ is the many-particle state vector at time t. In principle the Schrödinger equation describes the dynamics of any non-relativistic system, and in this section we will discuss how to solve it both for purely electronic systems as well as for systems of interacting electrons and bosons. We start by defining the Hamiltonian for a system of interacting electrons. The most general form we will consider is

$$H(t) = \sum_{ij\sigma} t_{ij}(t) c^\dagger_{i\sigma} c_{j\sigma} + \frac{1}{2} \sum_{ijlm\sigma\sigma'} U_{ijml} c^\dagger_{i\sigma} c^\dagger_{j\sigma'} c_{l\sigma'} c_{m\sigma}, \tag{2.2}$$

where $c_{i\sigma}$ destroys an electron in the orbital $|i\rangle$ with spin projection σ. The diagonal elements of the matrix $t_{ij}(t)$ describe the orbital energies and possible local potentials, while the off-diagonal elements describe the hopping between different orbitals and possible interactions with an external electromagnetic field. The tensor U_{ijlm} contains the two-particle Coulomb interaction, and in order for H to be Hermitian it must hold that $t_{ji}(t) = t^*_{ij}(t)$ and $U_{mlij} = U^*_{ijml}$.

What prevents an easy solution of the Schrödinger equation is the presence of interactions, which couple states where more than one particle has changed its state. To illustrate this point we temporarily assume that the Hamiltonian consists only of one-body operators,

$$H = \sum_{ij} t_{ij} c^\dagger_i c_j, \tag{2.3}$$

and ignore the spin degree of freedom. If the matrix t_{ij} is non-singular, H can be diagonalized by a unitary transformation $c_j = \langle j|k\rangle a_k$ of the creation and annihilation operators, where a_k destroys a particle in the eigenstate $|k\rangle$ of the matrix t_{ij}. Since the Hamiltonian is diagonal in the basis $|k\rangle$, the ground state for a system with N particles is given by the single Slater determinant

$$|\Psi_0\rangle = |k_1, k_2, \ldots, k_N\rangle, \tag{2.4}$$

where $|k_1\rangle$ to $|k_N\rangle$ are the N states of lowest energy. To find the ground state of a system of non-interacting electrons described by L orbitals it is therefore sufficient to solve a single matrix equation of size $L \times L$, which scales linearly with the size of the system. A similar simplification occurs also for time-dependent systems of non-interacting particles. The time-evolved state vector is then given by

$$|\Psi(t)\rangle = \mathcal{T} e^{-i\int_0^t dt' H(t')} |\Psi_0\rangle = |k_1(t), k_2(t), \ldots, k_N(t)\rangle, \tag{2.5}$$

where we have defined $|k(t)\rangle = \mathcal{T} e^{-i\int_0^t dt' H(t')} |k(0)\rangle$ and $\mathcal{T}$ is the time-ordering operator. The many-particle state $|\Psi(t)\rangle$ can therefore be obtained by separately time-evolving the single-particle states $|k\rangle$, and the time-dependent problem is also reduced to considering matrices of size $L \times L$.

For the general Hamiltonian in Eq. 2.2, no such simplification is possible, and to solve the Schrödinger equation we must work with the full basis of many-body states. We consider a system described by the L single-particle orbitals $|i\rangle$ and with $N = N_\uparrow + N_\downarrow$ particles, where $N_\uparrow$ and $N_\downarrow$ are the number of particles with spin up and down respectively. The basis of many-body states can be written like $|n_{i_1\sigma}, n_{i_2\sigma}, \ldots, n_{i_L\sigma}\rangle$, where $N_\uparrow$ ($N_\downarrow$) of the occupation numbers $n_{i\uparrow}$ ($n_{i\downarrow}$) are equal to one and the rest are zero. The number of ways in which the non-zero occupation numbers can be distributed gives the number of possible configurations N_e, that can be written as

$$N_e = \binom{L}{N_\uparrow}\binom{L}{N_\downarrow}. \tag{2.6}$$

In matrix form the electronic Schrödinger equation therefore becomes an eigenvalue problem of size $N_e \times N_e$. In the half-filled case $N_\uparrow = N_\downarrow = L/2$, we find for large L that $N_e \sim 4^L/(\pi L/2)$. The size of the problem therefore grows exponentially with L, and already for a moderate system size $L = 12$ the number of states is $N_e = 853776$. This scaling was referred to by Kohn as the exponential wall [1], and prohibits the application of exact diagonalization methods to systems larger than $L \approx 20$.

2.1.1 Electron-boson systems

We now add a degree of complexity and consider a system of interacting electrons and bosons. Depending on the particular features of the system we want to model, different forms of the Hamiltonian might be appropriate. The most general Hamiltonian we consider is

$$H(t) = H_e(t) + H_{e-b}(t) + H_{e-n}, \tag{2.7}$$

where $H_e(t)$ is the electronic Hamiltonian given in Eq. 2.2, and $H_{e-b}(t)$ and H_{e-n} are detailed below. For bosons corresponding to quanta of harmonic vibration, such as phonons, plasmons and photons, the Hamiltonian can be written like

$$H_{e-b}(t) = \sum_k \omega_k b_k^\dagger b_k + \sum_{ijk\sigma} g_{ijk}(t) c_{i\sigma}^\dagger c_{j\sigma}(b_k^\dagger + b_k). \tag{2.8}$$

Here b_k destroys a quantum of energy ω_k in the bosonic mode k, and the electron-boson coupling satisfies $g_{jik}(t) = g_{ijk}^*(t)$ in order for H_{e-b} to be Hermitian. To describe nuclear motion beyond the harmonic regime, it is more convenient to treat the nucleus in first quantization with a Hamiltonian

$$H_{e-n}(t) = \frac{p^2}{2M} + V(x) + \sum_{ij\sigma} g_{ij}(x) c_{i\sigma}^\dagger c_{j\sigma}. \tag{2.9}$$

Here p and x are momentum and position operators in first quantization, M is the nuclear mass, $V(x)$ an external nuclear potential, and $g_{ji}(x) = g^*_{ij}(x)$ the electron-nuclear interaction. The physics of coupled electron-boson systems will be discussed in detail in Chapters 4 and 5, and in the following we will focus on the computational aspects.

To solve the Schrödinger equation we want to write the Hamiltonian in matrix form using a complete basis of many-body states. A single boson mode k is described by the basis $|n_k\rangle$, where in principle $n_k = 0, 1, \ldots, \infty$. However, since we will work at zero temperature and finite coupling strength g_{ijk}, only a finite number of states will be significantly populated. We therefore truncate the boson space at some maximum number N_k, so that $n_k = 0, 1, \ldots, N_k$, and treat N_k as a convergence parameter. For K boson modes the procedure is identical, and gives the full boson basis $|n_{k_1}, n_{k_2}, \ldots, n_{k_K}\rangle$, with $n_{k_i} = 0, \ldots, N_{k_i}$. The size of the bosonic configuration space is then given by

$$N_b = N_{k_1} N_{k_2} \cdots N_{k_K}. \tag{2.10}$$

For the nuclear mode we use the real-space basis $|x\rangle$ corresponding to a continuous spectrum. In our calculations we restrict the coordinate to a finite interval $[x_{min}, x_{max}]$, and discretize the interval onto a finite grid $|x_n\rangle$ of size N_n. The basis states are then given by the coordinates $x_n = x_{min} + (n-1)x_{max}/N_n$, where $n = 1, 2, \ldots, N_n$. The length of the interval and the number of grid points have to be treated like convergence parameters. The full electron-boson problem can now be described in the basis

$$|\psi_m\rangle = |n_{i_1\sigma}, n_{i_2\sigma}, \ldots, n_{i_L\sigma}\rangle \otimes |n_{k_1}, n_{k_2}, \ldots, n_{k_K}\rangle \otimes |x_n\rangle, \tag{2.11}$$

for which the size is $N_{tot} = N_e N_b N_n$. In the next section we discuss how to handle this problem numerically.

2.1.2 Numerical implementation

The most direct method to solve the Schrödinger equation in matrix form is through exact diagonalization of the Hamiltonian. In equilibrium this corresponds to solving the eigenvalue problem

$$H(0)|\Psi(t)\rangle = E|\Psi(t)\rangle, \tag{2.12}$$

which gives N_{tot} eigenvalues and eigenvectors that we label by ϵ_λ and $|\psi_\lambda\rangle$. However, in most cases we are only interested in finding the ground state of a system, and therefore a full diagonalization is unnecessary. There are several numerical methods specialized in obtaining only one or a few eigenstates of a matrix, and in our calculations we have used the shift-invert method that extracts the eigenstates closest to a predefined energy ϵ from the poles of the resolvent $(H - \epsilon)^{-1}$. The groundstate is the eigenvector corresponding to

the eigenvalue with lowest energy, and for a non-degenerate ground state we take $|\Psi(0)\rangle = |\psi_0\rangle$. If the ground state is degenerate, then the states of the ground state manifold can be distinguished by looking at their eigenvalues with respect to some other operator, such as the total spin.

To solve the time-dependent Schrödinger equation, we start by considering the time-evolution of the system in a small interval $[t, t+dt]$. We can then write

$$|\Psi(t+dt)\rangle = \mathcal{T} e^{-i\int_t^{t+dt} H(t')dt'} |\Psi(t)\rangle \approx e^{-iH(t+dt/2)dt} |\Psi(t)\rangle, \tag{2.13}$$

which is correct to order $\mathcal{O}(dt^2)$ in the time step. To evaluate this expression we note that the time-evolution operator can be expanded in a series, $e^{-iHdt} = \sum_k (-idt)^k H^k/k!$, and so the state at time $t+dt$ is given as an expansion in the vectors $H^k|\psi(t)\rangle$. For small dt it is reasonable to assume that the time-evolution can be obtained from a truncated expansion. This observation forms the starting point for time-evolution schemes based on the Lanczos algorithm [2], which we outline in the following.

The Lanczos algorithm is a unitary transformation that maps the Hamiltonian onto a real tridiagonal matrix $T = U^\dagger H U$. The columns $|U_k\rangle$ of the transformation matrix U are known as the Lanczos vectors, and are constructed from the vectors $H^k|\Psi\rangle$ by Gram-Schmidt orthogonalization. In practice it is common to consider the space $\mathcal{K}_{N_L}$, known as the Krylov subspace of order N_L, which is spanned by the first N_L vectors $|U_k\rangle$. Intuitively this corresponds to truncating the expansion of e^{-iHdt} after N_L terms, while still retaining the unitarity of the time-evolution operator. In the Krylov subspace we can approximate the time evolution by

$$|\Psi(t+dt)\rangle \approx \sum_{i=1}^{N_L} |U_i\rangle\langle U_i| e^{-iT(t+dt/2)dt} |U_0\rangle = \sum_{i,\lambda=1}^{N_L} |U_i\rangle\langle U_i|\lambda\rangle e^{-i\epsilon_\lambda dt}\langle\lambda|U_0\rangle, \tag{2.14}$$

where ϵ_λ and $|\lambda\rangle$ are the eigenvalues and eigenvectors of T. For short time-steps dt this reproduces the full time evolution while only requiring the diagonalization of a matrix of order $N_L \times N_L$, and even for a very large basis it is typically enough to take $N_L \approx 10$. However, both dt and N_L have to be treated as convergence parameters.

2.2 Density matrix renormalization group

It is known from quantum statistical physics that to describe a macroscopic system only a few parameters are needed, such as temperature, entropy and internal energy. On the other hand, as we have seen in the previous section, a microscopic description of large systems involve a very large number of states and observables. It is then interesting to ask how the large set of observables in the microscopic description reduces to only a few at

the macroscopic scale? A large part of this answer came with Wilsons formulation of the renormalization group (RG) method [3, 4], in which a system is systematically rescaled from a microscopic to macroscopic description. This allows among other things for an identification of relevant and irrelevant variables, where only the relevant variables remain non-zero in the macroscopic limit.

The basic idea of RG methods is to find an optimal set of states to describe the low energy excitations of a system, by starting from a small system and successively increasing its size. In the original RG algorithms this was done by taking a system B (called a block) described by a number of states m, and coupling it to another identical block to form the product BB described by m^2 states. The Hamiltonian of the block BB is then diagonalized and the m states with lowest energy are kept. In a following renormalization step the Hamiltonian is projected onto the subspace of these m states, and the algorithm starts over with $B = BB$, again described by m states. It was soon realized that this algorithm performs quite poorly for many systems. One way to improve upon this situation is to increase the size of the block B more slowly, by adding only one site at a time instead of joining two identical blocks. From a physical point of view this approach has the advantage that the states kept will not have nodes where the states of the next iteration is close to a maximum, which is a problem encountered with the original algorithm when applied for example to a one-dimensional tight-binding model [5].

A crucial step forward came with the realization of White [6, 7], that in order to properly describe a system in the thermodynamic limit one should not consider an isolated system, but rather a system coupled to an environment. The optimal states to keep in representing the system are the m eigenstates of the reduced density matrix with the highest eigenvalues. This is motivated as follows: Consider the coupled system and environment to be in a definite state $|\psi\rangle$, where the system is described by the n_i states $|i\rangle$ and the environment by the n_j states $|j\rangle$. Then we can write $|\psi\rangle = \sum_{ij} \psi_{ij}|i\rangle|j\rangle$. We now want to find a set of m states $|u^\alpha\rangle$, that represents the state $|\psi\rangle$ in an optimal way. More precisely, we want to find the states that minimize the difference $S = ||\psi\rangle - |\tilde{\psi}\rangle|^2$, where $|\tilde{\psi}\rangle$ is defined by $|\tilde{\psi}\rangle = \sum_{\alpha j} a_{\alpha j}|u^\alpha\rangle|j\rangle$. It can be shown that the states that minimize S are the m eigenstates of the reduced density matrix $\rho_{ii'} = \sum_j \psi_{ij}\psi_{i'j}$ with the largest eigenvalues.

To implement this procedure we define B_ℓ to be a block of size ℓ, B_ℓ^R to be its parity transformed reflection, and $\bullet$ to be a single site. The density matrix renormalization group (DMRG) algorithm introduced by White for an infinite system is then as follows [7], for the step going from ℓ to $\ell + 1$: Start by constructing the superblock $B_\ell \bullet \bullet B_\ell^R$ and find its ground state. Calculate the reduced density matrix of the subsystem $B_\ell\bullet$, by tracing out the degrees of freedom of the environment $\bullet B_\ell^R$, and find its m eigenstates $|u^\alpha\rangle$ with highest weight. Renormalize the Hamiltonian of the system $B_\ell\bullet$ by transforming it to the new basis $|u^\alpha\rangle$. Define $B_{\ell+1} = B_\ell\bullet$ and start the next step of the algorithm.

For a finite system with L orbitals this algorithm should only be carried out a finite number of times, until the size of the superblock reaches the size of the system. After the system has reached its target size the ground state is iteratively improved by a method called sweeping, in which the size ℓ of the left block is varied between 1 and $L-3$ with the superblock being $B_\ell \bullet \bullet B^R_{L-\ell-2}$. After each change in B_ℓ the Hamiltonian is again renormalized by the eigenstates of the reduced density matrix, and the algorithm is continued until the difference in the ground state between two consecutive steps is smaller than a specified convergence parameter. When convergence has been reached the ground state of the full system is typically obtained as the ground state of the superblock $B_{L/2-1} \bullet \bullet B^R_{L/2-1}$. By increasing m the difference with the real ground state of the system can be made arbitratily small. The matrix of the Hamiltonian to be diagonalized in each step will be of size $(mn)^2$, where n is the size of the Hilbert space of a single site.

How can we estimate the number of states m needed to describe a system of size L? A hand-waving argument based on entropy goes as follows [8]: The entropy S_L corresponding to the density matrix of a block B_L is given by $S_L = \operatorname{Tr} \rho_L \ln \rho_L$, and its maximal value $S_L^{max} = \ln m$ is obtained when all eigenvalues of ρ_L are equal to m. The number of states needed to represent a system of maximal entropy is therefore $m = e^{S_L^{max}}$. For ground states it can be shown that the entropy scales according to an area law [9], meaning that $S \sim L^{d-1}$ with d the dimension of the system. This implies that for a one-dimensional system m is largely independent of the system size, while in two dimensions $m \sim e^L$. This limits the DMRG algorithm to one-dimensional systems, or to rather small systems in higher dimensions. In practice it is enough to take $m \approx 100$ for most 1D systems, which for a chain with $L = 100$ gives a Hamiltonian of size 160000. This can be compared with the size $N_{tot} \sim 10^{29}$ of the many-body Hilbert space for the same system.

The DMRG method can be extended to also treat time-dependent problems. Here we encounter the problem that the states $|m\rangle$ describing the DMRG ground state $|\Psi(0)\rangle$ is in general not adapted to describe the time-evolved state $|\Psi(t)\rangle$, since $|\Psi(t)\rangle$ can explore parts of the Hilbert space not well represented by $|m\rangle$. To tackle this issue usually one of two strategies are followed: Firstly, we can enlarge the Hilbert space during the time evolution, to take into account the extended Hilbert space explored by the state $|\Psi(t)\rangle$. Secondly, we can try to use the time-independent DMRG formalism to adapt the basis in time. Since a full discussion of these strategies are quite lengthy, we refer the interested reader to [10]. We note however one particular feature of time-dependent DMRG (tDMRG). Due to an accumulation of the truncation error introduced by the renormalization procedure, after a certain time t_r known as the runaway time, the precision of the tDMRG results decreases by orders of magnitude. The runaway time increases with m but decreases with the time-step dt (for a fixed final time), so in practice the length of a tDMRG simulation is limited by the value of m and the time-scale of the dynamics.

2.3 Density functional theory

As mentioned in the introduction to this chapter, it is possible to reformulate the many-body problem posed by the Schrödinger equation in terms of an effective single-particle problem. This leads to a great numerical simplification (as discussed in Sec. 2.1), since instead of considering the full basis of many-body states it is enough to work with a basis of single-particle states. Below we discuss the details of this reformulation, which is known as density functional theory (DFT) in its ground state version, and time-dependent density functional theory (TDDFT) in the non-equilibrium case. Before delving into the theory itself, it is worth mentioning that an important idea implicit in DFT is that of reduction. As discussed by Kohn in his Nobel lecture [1], already for systems of moderate size the state vector contains so many components that even if it could be found, it can not be stored on any foreseeable computer. A key aspect of DFT is therefore that it reduces the problem to concern the electronic density $n(\mathbf{r})$, that even for large systems is a manageable quantity.

The ground state version of DFT was formulated in two seminal papers by Hohenberg and Kohn [11] and by Kohn and Sham [12]. In the first paper a one-to-one mapping is established between the ground state electron density and state vector of the system, which is known as the Hohenberg-Kohn theorem. This proof was extended to degenerate ground state manifolds by Levy [13]. In the second paper it is argued how the exact electron density of an interacting system can be obtained from that of an auxiliary non-interacting system, through what is now known as the Kohn-Sham construction. Since the original works the DFT framework have been extended in several directions. How to treat non-collinear spins was described by von Barth and Hedin [14], and Vignale and Rasolt [15] extended the theory to describe currents and magnetic fields. The theory was adapted to lattice models by Gunnarsson and Schönhammer [16]. For time-dependent problems the corresponding mapping from electron density to state vector was first proven by Runge and Gross [17] and later generalized by van Leeuwen [18]. The first application to time-dependent lattice problems was done by Verdozzi [19], and the questions of representability were thoroughly addressed by Tokatly for current DFT [20] and Farzanehpour and Tokatly for DFT [21].

2.3.1 Ground state density functional theory

In this section we prove Levy's version of the Hohenberg-Kohn theorem, following the procedure outlined in [13, 22], and show how to construct the Kohn-Sham system. We consider a general electronic Hamiltonian of the form $H = T + U + \sum_i v(\mathbf{r}_i)$, where T is the kinetic energy operator, U the electron-electron interaction, and v an external potential. We start by defining the energy functional $E[n] = F[n] + \int d\mathbf{r} v(\mathbf{r}) n(\mathbf{r})$, which depends on

the electron density $n(\mathbf{r})$ at all points in space. Here

$$F[n] = \min_{|\Psi\rangle \in M} \langle \Psi | T + U | \Psi \rangle, \tag{2.15}$$

and M is the set of states that give the expectation value $\langle n \rangle = n$. If we pick $|\Psi\rangle$ to be a state for which F attains its minimum, then

$$E[n] = F[n] + \int d\mathbf{r} v(\mathbf{r}) n(\mathbf{r}) = \langle \Psi | H | \Psi \rangle \geq E_0. \tag{2.16}$$

The inequality follows from the variational principle since the density that minimizes F may not be that which minimizes E. Now pick a ground state $|\Psi_0\rangle$ of the full Hamiltonian, and call the corresponding density n_0. Then

$$E_0 = \langle \Psi_0 | T + U | \Psi_0 \rangle + \int d\mathbf{r} v(\mathbf{r}) n_0(\mathbf{r}) \geq F[n_0] + \int d\mathbf{r} v(\mathbf{r}) n_0(\mathbf{r}) = E[n_0] \tag{2.17}$$

Combining the inequalities we see that $E[n] \geq E_0$ for any density $n(\mathbf{r})$, and that $E[n_0] = E_0$ for the true ground state density $n_0(\mathbf{r})$. This allows us to find both the ground state energy and state vector by minimizing $E[n]$ [13].

It was realized by Kohn and Sham that it is possible to derive a set of single-particle equations that reproduce the exact ground state density of the interacting system. For this purpose we write the total energy like $E[n] = T_0[n] + E_H[n] + E_{ext}[n] + E_{xc}[n]$, where T_0 is the kinetic energy of a non-interacting system, E_H is the Hartree energy and E_{ext} the external energy. The remaining contribution E_{xc} is called the exchange-correlation energy and contains all interaction effects beyond the mean-field level. Since the energy satisfies the variational principle it must hold that

$$\delta E[n] = \int d\mathbf{r} \left(\frac{\delta T_0}{\delta n} + v + v_H[n] + v_{xc}[n] \right) \delta n(\mathbf{r}) = 0. \tag{2.18}$$

Here the potentials are defined as functional derivatives with respect to the density, so $v = \delta E_{ext}/\delta n$, $v_H = \delta E_H/\delta n$, and $v_{xc} = \delta E_{xc}/\delta n$. The equation above is the same as we would find by calculating the energy from the ground state of the Hamiltonian $H = T + \sum_i v_{KS}[n](\mathbf{r}_i)$, where $v_{KS} = v + v_H + v_{xc}$ is known as the Kohn-Sham potential. Instead of solving the full many-body Schrödinger equation we can therefore solve the set of single-particle equations

$$\left[T + v_{KS}[n](\mathbf{r}) \right] \psi_i(\mathbf{r}) = \epsilon_i \psi_i(\mathbf{r}). \tag{2.19}$$

These equations are known as the Kohn-Sham equations, and a few remarks about them are in order. First we note that since v_{KS} depends on the density, the equations must be solved self-consistently with $n(\mathbf{r}) = \sum_i |\psi_i(\mathbf{r})|^2$ constructed from the N states of lowest energy

(for a system with N particles). Secondly, the energies ϵ_i and orbitals ψ_i have no physical meaning, since they are the solutions of an auxiliary problem. The exception is the energy of the highest occupied orbital, that was shown by Almbladh and von Barth to equal the exact ionization energy of the system [23]. However, in practice the Kohn-Sham energies are usually considered to be a good approximation to the exact single-particle excitations of the system. Thirdly, since v_{xc} is defined by a derivative, there is in the general case no guarantee that it exists. The Kohn-Sham construction tells us that if there is such a potential, it is given by v_{xc}, but gives no information about its existence. This is known as the v-representability problem of DFT, and is in the general case as of yet unsolved.

Although the Kohn-Sham equations look deceptively simple, obtaining the exact exchange-correlation potential is as hard a problem as solving the many-particle Schrödinger equation. This is since the construction of v_{xc} requires a full knowledge of the energy of the interacting system. Also, the potential at a given point $\mathbf{r}$ depends on the density profile at all points in space. In practice it is therefore necessary to approximate v_{xc} somehow. If we assume that the density $n(\mathbf{r})$ varies slowly with position, the dependence of v_{xc} on the density can be shown to be local [11, 12]. Assuming this is true in general we obtain the so-called local density approximation (LDA), where we write $v_{xc}[n](\mathbf{r}) = v_{xc}(n(\mathbf{r}))$ and approximate $v_{xc}(n(\mathbf{r}))$ with the potential of a uniform electron gas of density n. A strength of the DFT formulation is that for many systems the dominating contributions to the total energy comes from the kinetic and Hartree energies, which means E_{xc} is expected to give a small contribution. Under these circumstances we expect the LDA to perform well, which is also verified by comparison to experiment. There are also many systems for which the LDA is not valid due to strong electron-electron interactions, and they are referred to as strongly correlated materials.

2.3.2 Time-dependent density functional theory

The DFT framework is extended to time-dependent problems by the Runge-Gross theorem [17]. We assume that the electronic Hamiltonian is of the form $H = T + U + \sum_i v(\mathbf{r}_i, t)$, and that the density $n(\mathbf{r}, t)$ and external potential $v(\mathbf{r}, t)$ are analytic functions of time. The theorem then states that the density of an interacting system can be found by solving the equations

$$i\frac{\partial}{\partial t}\psi_i(\mathbf{r}, t) = \left[T + v_{KS}[n](\mathbf{r}, t)\right]\psi_i(\mathbf{r}, t), \tag{2.20}$$

where $n(\mathbf{r}, t) = \sum_i |\psi_i(\mathbf{r}, t)|^2$. To obtain the exact time-dependent density the potential v_{KS} has to be chosen according to $v_{KS} = v + v_H + v_{xc}$, where in analogy with the ground state case the exchange-correlation part is given by $v_{xc} = \delta A_{xc}/\delta n$ and A_{xc} is the exchange-correlation part of the action integral [17]. A few remarks are again in order. Firstly, the

time-dependent Kohn-Sham equations have to be solved with the initial conditions that the density $n(\mathbf{r}, 0)$ and current $\mathbf{j}(\mathbf{r}, 0)$ are the same in the interacting and Kohn-Sham systems [17, 18]. Secondly, the value of v_{xc} at a particular point $(\mathbf{r}, t)$ depends on the density at all points $\mathbf{r}$ and all previous times $t' < t$. In this sense, the exact v_{xc} is said to contain the memory of the system, which makes it extremely difficult to find. In reality it is therefore common practice to assume that the potential depends only on the (time and space) local density, $v_{KS}[n](\mathbf{r}, t) = v_{KS}(n(\mathbf{r}, t))$, which is known as the adiabatic local density approximation (ALDA). This approximation is expected to perform well for systems where the density varies slowly both in time and space.

2.3.3 Multi-component systems

In many situations it is important to not only consider the dynamics of electrons, but also other degrees of freedom such as the motion of atomic nuclei or the presence of photon fields. It is therefore of interest to extend the DFT and TDDFT frameworks to multi-component systems treating both electrons and bosons on the same footing. In fact, the development of multi-component theories is a topic of intense research, with present works extending the basic theory to electron-nuclear systems [24, 25] as well as electron-photon systems both in the non-relativistic [26, 27] and relativistic [28] limit.

In constructing a general density functional theory it is necessary to define a suitable set of basic variables, in terms of which the state of the system can be labeled. For the continuum theory discussed above a possible labelling is $|\Psi(v)\rangle$, where $v(\mathbf{r})$ is the external potential of the system. However, since by the Hohenberg-Kohn theorem the external potential $v(\mathbf{r})$ is in one-to-one correspondence with the electron density $n(\mathbf{r})$, an alternative way to label the states is by $|\Psi(n)\rangle$. Although not strictly true, an intuitive way of understanding this relationship is to consider the pair (v, n) as conjugate variables, and the transformation from $|\Psi(v)\rangle$ to $|\Psi(n)\rangle$ as a Legendre transform (for a detailed discussion see e.g. [28]). This reasoning allows us to identify possible extensions of the basic theory, by considering other pairs of conjugate variables. For example, in systems with an external vector potential $\mathbf{A}(\mathbf{r})$, for which the conjugate variable is the current density $\mathbf{j}(\mathbf{r})$, it is possible in a similar fashion as in basic DFT to show a one-to-one correspondence between the pair $(\mathbf{A}, \mathbf{j})$ [15]. This leads to a current DFT where the states are labeled by $|\Psi(\mathbf{j})\rangle$.

The same philosophy can be used when considering multi-component systems. Here we will discuss a model of lattice electrons coupled to a single nuclear coordinate, as was used in Paper I to study effects of electron-nuclear interactions during desorption. However, the theory can be straightforwardly extended to N mutually interacting nuclei, as discussed in

detail in Appendix B. We consider the Hamiltonian

$$H = \sum_i U n_{i\uparrow} n_{i\downarrow} + \sum_{ij\sigma} \left(T^{ext}_{ij}(t) c^\dagger_{i\sigma} c_{j\sigma} + h.c. \right) + \frac{p}{2M} + V^{ext}(x,t) \qquad (2.21)$$
$$+ \sum_{ij\sigma} H^{int}_{ij}(x) \left(c^\dagger_{i\sigma} c_{j\sigma} + h.c. \right),$$

where U is the electron-electron interaction and T^{ext} a complex external field of modulus one acting on the electrons. The nuclear system is described by the momentum p and coordinate x, with M the nuclear mass and V^{ext} an external nuclear potential. Finally the electron-nuclear interaction is given by H^{int}. For the desorption process considered in Paper I an important point is that the hopping amplitude can vary in time due to the motion of the atomic nucleus. In particular, for a large separation of the atoms (corresponding to a large x), the amplitude should tend to zero. To capture this effect in a non-interacting system, it is necessary that the Kohn-Sham potential T_{KS} have both a phase and modulus that can vary in time.

With this in mind, we now want to identify the conjugate variables of the external fields (T^{ext}, V^{ext}). For the nuclear system this is straightforward, since like in ordinary DFT the internal variable conjugate to $V^{ext}(x)$ is the nuclear density $\Gamma(x)$. For N nuclei, this should be replaced with the diagonal of the nuclear one-particle density matrix. For the electrons, we note that without the electron-nuclear coupling the variable conjugate to T^{ext} is the electronic current j. In presence of electron-nuclear interactions this is generalized to a complex electronic current Q [20], that is defined by $Q^\sigma_{ij}(t) = T^{ext}_{ij}(t)\rho^\sigma_{ij}(t) + \tilde{\rho}^\sigma_{ij}(t)$. Here ρ is the electronic one-particle density matrix, and the additional nuclear effects are contained in $\tilde{\rho}^\sigma_{ij}(t) = \langle \psi(t) | H^{ext}_{ij}(x) c^\dagger_{i\sigma} c_{j\sigma} | \psi(t) \rangle$. The real and imaginary parts of the complex current give respectively the bond kinetic energy K_{ij} and the electronic current density j_{ij}. A proof of the one-to-one mapping $(T^{ext}, V^{ext}) \leftrightarrow (Q, \Gamma)$ is given in Appendix B, and leads to the Kohn-Sham Hamiltonians

$$H^{KS}_e = \sum_{ij\sigma} \left(T^{KS}_{ij}[Q_{ij}, \Gamma](t) c^\dagger_{i\sigma} c_{j\sigma} + h.c. \right) \qquad (2.22a)$$

$$H^{KS}_n = \sum_k \frac{p^2}{2M} + V_{KS}[Q_{ij}, \Gamma](x,t). \qquad (2.22b)$$

These operators give rise to a set of coupled single-particle equations evolving under the effective potentials T_{KS} and V_{KS}. In Section 5.1 as well as in Paper I we discuss how to construct the exact potentials for a system during desorption.

2.4 Ehrenfest approximation

Due to the large mass difference between electrons and nuclei, it is in many circumstances not necessary to treat the electron and nuclear dynamics on the same footing. More precisely, in the limit where the nuclear mass M tends to infinity, the spread of the nuclear wavefunction and the characteristic nuclear velocity $v = p/M$ tend to zero, leading to a separation of the electronic and nuclear time-scales. In this limit the nuclear coordinates can be treated as classical variables, and we can solve for the electronic ground state for a fixed nuclear configuration. This is formalized by the Born-Oppenheimer approximation, where the total Hamiltonian H of the electron-nuclear system is separated according to

$$H = T_e + U_{e-e} + U_{e-n} + U_{n-n} + T_n = H_{BO} + T_n, \tag{2.23}$$

and where T and U are kinetic and interaction terms respectively. In the limit of infinite mass the nuclear kinetic energy $T_n \to 0$, and the Born-Oppenheimer Hamiltonian will depend parametrically on the nuclear coordinates by $H_{BO} = H_{BO}(\mathbf{R})$. Here $\mathbf{R} = \{\mathbf{R}_\nu\}$ is defined as a short-hand notation for the set of nuclear coordinates. Solving the Schrödinger equation for H_{BO} for all possible nuclear configurations gives rise to a number of potential energy surfaces $V_i(\mathbf{R})$, and the ground state energy E_0 will be at the minimum $\mathbf{R}_0$ of the lowest surface, $E_0 = V_0(\mathbf{R}_0)$.

To describe the dynamics of an electron-nuclear system, we would like to extend this reasoning to the time domain. In the limit of large but finite nuclear mass, we can approximate the wavefunction as a product state $|\Psi\rangle = |\phi_{\mathbf{R}}\rangle \otimes |\chi\rangle$, with $|\phi_{\mathbf{R}}\rangle$ the electronic and $|\chi\rangle$ the nuclear wavefunction. For slow perturbations, the electrons can be considered to be in their instantaneous ground state, and we can solve the Schrödinger equation for the electrons with the Born-Oppenheimer Hamiltonian together with the nuclear equation of motion

$$i\frac{\partial}{\partial t}|\chi_n(t)\rangle = [T_n + V_0(\mathbf{R})]|\chi_n(t)\rangle. \tag{2.24}$$

In this adiabatic approximation the nuclei therefore evolve on the ground state potential energy surface. For faster perturbations, the electrons may be excited to higher states, and it is necessary to replace the product wavefunction with the so-called Born-Oppenheimer expansion. This however reintroduces the same complexity to the problem as solving the original Schrödinger equation, and so reduces the efficiency of the approach.

A way to derive a set of semi-classical equations of motion for the coupled electron-nuclear system is to replace the product wavefunction of the Born-Oppenheimer approximation with the exact product wavefunction introduced by Abedi, Maitra and Gross [29]. Using $\mathbf{r} = \{\mathbf{r}_\mu\}$ to denote the set of electronic coordinates, the total wavefunction can be written as $\Psi(\mathbf{r}, \mathbf{R}, t) = \phi_{\mathbf{R}}(\mathbf{r}, t)\chi(\mathbf{R}, t)$, where the electronic wavefunction satisfies the partial

normalization condition $\int d\mathbf{r}|\phi_{\mathbf{R}}(\mathbf{r},t)|^2 = 1$. The electron and nuclear wavefunctions satisfy the equations [29]

$$i\frac{\partial}{\partial t}\phi_{\mathbf{R}}(\mathbf{r},t) = \left[H_e(\mathbf{r},\mathbf{R},t) - V(\mathbf{R},t)\right]\phi_{\mathbf{R}}(\mathbf{r},t) \tag{2.25a}$$

$$i\frac{\partial}{\partial t}\chi(\mathbf{R},t) = \left[\sum_\nu \frac{1}{2M_\nu}\left(-i\nabla_\nu + \mathbf{A}_\nu(\mathbf{R},t)\right)^2 - V(\mathbf{R},t)\right]\chi(\mathbf{R},t), \tag{2.25b}$$

where the scalar potential is given by $V(\mathbf{R},t) = \langle\phi_{\mathbf{R}}(t)|H_e(\mathbf{r},\mathbf{R},t) - i\partial_t|\phi_{\mathbf{R}}(t)\rangle$ and the vector potential by $\mathbf{A}_\nu(\mathbf{R},t) = -\langle\phi_{\mathbf{R}}(t)|i\nabla_\nu\phi_{\mathbf{R}}(t)\rangle$. These equations are in principle exact and equivalent to the Schrödinger equation for $|\Psi\rangle$, provided the scalar and vector potentials are known. Here however, we use them to derive the semi-classical limit of electron-nuclear dynamics.

If we let $M_\nu \to \infty$ and choose the gauge where $\langle\phi_{\mathbf{R}}(t)|\partial_t\phi_{\mathbf{R}}(t)\rangle = 0$, the electronic Hamiltonian is given by the Born-Oppenheimer expression $H_e(\mathbf{r},\mathbf{R},t) = H_{BO}(\mathbf{r},\mathbf{R}(t)) + v_{ext}(\mathbf{r},t)$. To find an equation of motion for the nuclear coordinates, we interpret the position and momentum in Eq. 2.25b as classical variables, and use the resulting Hamiltonian in the classical Hamilton equations. The equation of motion for $\mathbf{R}_\nu$ is then

$$M_\nu\frac{\partial^2\mathbf{R}_\nu}{\partial t^2} = -\nabla_\nu\epsilon(\mathbf{R},t) + \frac{\partial}{\partial t}\mathbf{A}_\nu(\mathbf{R},t) - \frac{\partial\mathbf{R}_\nu}{\partial t}\times\left(\nabla_\nu\times\mathbf{A}_\nu(\mathbf{R},t)\right). \tag{2.26}$$

This equation closely resembles that of a particle evolving under the Lorentz force, although with a different sign convention for $\mathbf{A}$ coming from Eq. 2.25b. It should however be noted that the potentials entering this equation are not due to external fields, but come from the interaction with the electrons. This equation can be propagated together with the electronic dynamics resulting from the Born-Oppenheimer Hamiltonian to give a semi-classical description of an electron-nuclear system. However, it is common to make the further assumption that the vector potential $\mathbf{A}$, corresponding to a geometric Berry connection, is zero. The resulting equation for $\mathbf{R}$ is known as the Ehrenfest approximation, and is used in Papers II and IV. The equations of motion for the nuclear coordinates are in the Ehrenfest approximation given by

$$M_\nu\frac{\partial^2\mathbf{R}_\nu}{\partial t^2} = -\nabla_\nu\langle H_e(\mathbf{r},\mathbf{R},t)\rangle. \tag{2.27}$$

Chapter 3

Correlator based methods

In the previous chapter we discussed methods for solving the many-body problem based either on the evaluation of the many-particle state vector, or the calculation of an effective set of single-particle states. In this chapter we take a different approach, and introduce the non-equilibrium Green's function method. In this method we are not concerned with finding the state of the system, but rather with the direct calculation of certain correlation functions related to experimental observables. This reduces the complexity of the problem, but at the expense of introducing a new quantity known as the self-energy, that like the exchange-correlation potential of DFT contains all complicated interaction effects. We start by defining the central quantity, the one-particle Green's function, and motivate its equation of motion (Sec. 3.1). In the following sections we discuss how to use the Green's function to extract experimental observables, and how to construct appropriate approximations to the self-energy. Then we discuss the generalized Kadanoff-Baym ansatz, an additional approximation that reduces the computational complexity of evaluating the Green's function. In the last section we combine density functional theory with the Green's function method, and outline how to perform simulations of realistic materials through the *GW* method (Sec. 3.2).

3.1 Non-equilibrium Green's functions

The fundamental idea behind Green's function based methods is that in order to extract experimentally relevant observables, a knowledge of the full state vector is not strictly necessary. Since most quantities of interest involve one or a few particles, and are obtained from the state vector by tracing out the remaining degrees of freedom, instead of first trying to calculate the state of the system and then remove all unwanted information, the Green's

function method proceeds to the direct calculation of observables.

Historically the Green's function was introduced as a mathematical tool for solving inhomogeneous differential equations, and have its name from its inventor George Green. The Green's functions used to study condensed matter systems are however not Green's functions in the strict mathematical sense, except when applied to non-interacting systems. Instead the many-body Green's functions are defined as correlation functions of field operators, and were originally introduced in the context of quantum electrodynamics (QED) by Schwinger [30] and Feynman [31]. In the QED framework the system is assumed to be at zero temperature and the Hamiltonian is independent of time, so the correlation functions can be evaluated in the interacting ground state. The formalism was later generalized to finite temperature by Matsubara [32], and to non-equilibrium systems by Kadanoff and Baym [33], Schwinger [34] and Keldysh [35]. The different flavors of Green's functions can be unified in an elegant manner by defining a Green's function with time arguments on a complex contour, where different choices of the contour correspond respectively to the $T = 0$, $T > 0$ and non-equililbrium formalisms [36]. We start the discussion by defining the one-particle Green's function G on the Schwinger-Keldysh contour γ, and later show how to reduce the formalism to that for equilibrium systems.

Before discussing the equation of motion for G, we need to write the Hamiltonian in terms of the field operators ψ. This gives

$$H(z) = \int d\mathbf{x}\psi^\dagger(\mathbf{x})h(\mathbf{r},z)\psi(\mathbf{x}) + \frac{1}{2}\int d\mathbf{x}d\mathbf{x}'\psi^\dagger(\mathbf{x})\psi^\dagger(\mathbf{x}')u(\mathbf{x},\mathbf{x}')\psi(\mathbf{x}')\psi(\mathbf{x}), \quad (3.1)$$

where z is a complex time that lies on the contour γ of Fig. 3.1, $\mathbf{x} = (\mathbf{r},\sigma)$, and we have assumed that the single particle Hamiltonian h is independent of spin. For complex $z = i\tau$ we take $h(\mathbf{r},i\tau) = h(\mathbf{r},0) - \mu$, with μ the chemical potential, so that $H(z)$ is defined on the full contour. The one-particle Green's function is defined in terms of the field operators as [36]

$$G(1,2) = -\frac{i}{Z}\,\mathrm{Tr}\left[\mathcal{T}e^{-i\int_\gamma dzH(z)}\psi(1)\psi^\dagger(2)\right], \quad (3.2)$$

where we have used the notation $i = (\mathbf{x}_i, z_i)$ as a collective index denoting space, spin and time variables. Here $Z = \mathrm{Tr}\, e^{-\beta H(0)}$ is the partition function describing the initial preparation of the system, and β is the inverse temperature. The operator $\mathcal{T}$ orders time arguments on γ with earlier times to the right, with the convention that the contour begins at $z = i\beta/2$ and ends at $z = -i\beta/2$ (see Fig. 3.1). In this expression the field operators only carry a time index to indicate in which order they should be placed by the time-ordering operator $\mathcal{T}$, and have no explicit time dependence. The equation of motion for the Green's function is obtained be differentiating the expression above and using the Heisenberg equa-

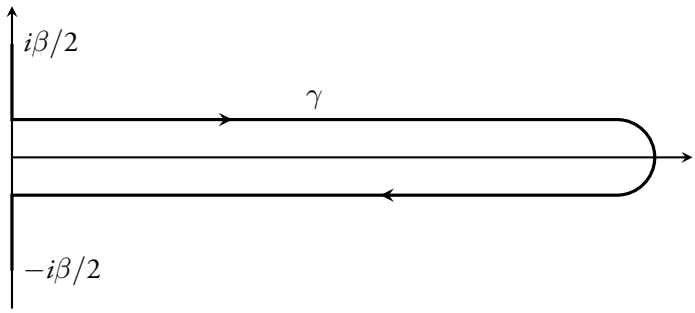

Figure 3.1: The Schwinger-Keldysh contour γ on which the non-equilibrium Green's function $G(1,2)$ has its time arguments. The horizontal axis corresponds to real time $z = t$ and the vertical axis to imaginary time $z = i\tau$.

tion for the field operators. This gives [36]

$$\left[i\frac{\partial}{\partial z_1} - h(1)\right] G(1,2) = \delta(1,2) - i\int_\gamma d3u(1,3)G_2(1,3,2,3^+), \tag{3.3}$$

where the quantity G_2 appearing under the integral is the two-particle Green's function, and is defined similarly to G but contains two creation and two annihilation operators. The presence of G_2 prevents us from closing the equation of motion for G, and to proceed we need to derive an equation also for G_2. It turns out that this expression couples G_2 to G and the three-particle Green's function G_3, and more generally we obtain a set of equations coupling G_n to G_{n-1} and G_{n+1}. These equations are known as the Martin-Schwinger hierarchy, whose solution is equivalent to solving the full many-body problem. A thorough discussion of the hierarchy would take us too far off topic, and we refer the interested reader to [36].

Since we are mainly interested in the one-particle Green's function G, we want to rewrite its equation of motion in such a way that the equation closes for G. It turns out that this is possible if we introduce a new quantity, known as the self energy $\Sigma(1,2)$, that is defined by [36]

$$\int_\gamma d3\Sigma(1,3)G(3,2) = -i\int_\gamma d3u(1,3)G_2(1,3,2,3^+). \tag{3.4}$$

With this definition the equation of motion for G, known as the Kadanoff-Baym equation, takes the form

$$\left[i\frac{\partial}{\partial z_1} - h(1)\right] G(1,2) = \delta(1,2) + \int_\gamma d3\Sigma(1,3)G(3,2). \tag{3.5}$$

This is the fundamental equation of the NEGF method. Much like the exchange-correlation potential of DFT, the self-energy contains all many-body and interaction effects, and also carries the memory of the system. If we were able to find the exact self-energy this equation

would give us the exact time-evolution of the Green's function. However, this is generally not possible, and we will discuss below how to approximate Σ.

To solve the Kadanoff-Baym equation we need to transform it from contour time to real-time variables. Depending on where (z_1, z_2) lie on the contour we differentiate between five different components of G. For (z_1, z_2) on the horizontal (real) axis, we define the lesser Green's function $G^<$ for $z_1 < z_2$, and the greater Green's function $G^>$ for $z_1 > z_2$. If the right argument is on the vertical axis and the left on the horizontal, $(z_1, z_2) = (t_1, i\tau_2)$, we talk of the right Green's function $G^\rceil$, while for $(z_1, z_2) = (i\tau_1, t_2)$ we have the left Green's function $G^\lceil$. Finally if both arguments are on the vertical axis, $(z_1, z_2) = (i\tau_1, i\tau_2)$, we define the Matsubara Green's function G^M. We can now write an equation of motion for each of these components by making use of the so-called Langreth rules [37], that describe how to transform the convolution integral in Eq. 3.5 from contour to real times. Since these equations are quite lengthy we don't reproduce them here, and the reader is referred to [36].

If we are interested in describing equilibrium systems at finite temperature, it is sufficient to consider solely the Matsubara Green's function G^M. This is equivalent to replacing the full Schwinger-Keldysh contour by only the vertical segment. In the zero-temperature ($\beta \to \infty$) formalism it is common to work with the time-ordered Green's function $G^T(1,2) = \theta(t_1 - t_2)G^>(1,2) - \theta(t_2 - t_1)G^<(1,2)$, where the contour is chosen as $\gamma_0 = \mathbb{R}$. Since we are at zero temperature only the ground state contributes to the trace in Eq. 3.2, and we can write $G^T(1,2) = \langle\Psi|\mathcal{T}\psi(1)\psi^\dagger(2)|\Psi\rangle$ with $|\Psi\rangle$ the interacting ground state.

3.1.1 Relation to observables

So far we have defined the Green's function as a mathematical object, and now we discuss its physical content and relation to observables. The time-dependent expectation value of any one-particle operator $O(1) = o(1)\psi^\dagger(\mathbf{x}_1)\psi(\mathbf{x}_1)$ can be written

$$\langle O(1)\rangle = \frac{1}{Z}\,\mathrm{Tr}\left[o(1)\mathcal{T}e^{-i\int_\gamma dz H(z)}\psi^\dagger(1)\psi(1)\right] = -io(1)G^<(1,1). \tag{3.6}$$

The knowledge of G therefore allows us to compute any one-particle expectation value, such as the density $n(\mathbf{x})$ or current density $\mathbf{j}(\mathbf{x})$. In an analogous way the n-particle Green's function gives access to the expectation value of any n-particle operator. If we solve Eq. 3.5 for G we are in general unable to compute the average of two- or many-particle operators. There is however an exception, the total energy of the system, that can be obtained from solely the knowledge of G. This is since the interaction energy, formally a two-body operator, can be extracted from the equation of motion 3.3 for G in the limit $2 \to 1^+$. Restricting

for simplicity to systems in equilibrium, we can write the interaction energy as

$$\langle U \rangle = -\frac{i}{2} \int d\mathbf{x}_1 \lim_{2 \to 1^+} \left[i \frac{\partial}{\partial z_1} - h(1) \right] G(1,2). \tag{3.7}$$

Combined with the average $\langle T \rangle$ of the single-particle term of the Hamiltonian, this gives the so-called Galitskii-Migdal formula for the total energy

$$E = -\frac{i}{2} \int d\mathbf{x}_1 \lim_{2 \to 1^+} \left[i \frac{\partial}{\partial z_1} + h(1) \right] G(1,2). \tag{3.8}$$

For systems in equilibrium the Green's function is invariant under time translations, and so only depends on $z = z_2 - z_1$. This allows us to define the Fourier transform $G(\mathbf{x}_1, \mathbf{x}_2, \omega)$, which in the zero temperature limit gives the lesser and greater components [36]

$$G^<(\mathbf{x}_1, \mathbf{x}_2, \omega) = 2\pi i \sum_m Q_m^*(\mathbf{x}_2) Q_m(\mathbf{x}_1) \delta(\omega - E_0 + E_m^{N-1}) \tag{3.9a}$$

$$G^>(\mathbf{x}_1, \mathbf{x}_2, \omega) = -2\pi i \sum_m P_m^*(\mathbf{x}_2) P_m(\mathbf{x}_1) \delta(\omega - E_m^{N+1} + E_0) \tag{3.9b}$$

These functions have peaks at the exact removal and addition energies $E_0 - E_m^{N-1}$ and $E_m^{N+1} - E_0$ of the interacting many-particle system, weighted by the amplitudes $Q_m(\mathbf{x}) = \langle \Psi_m^{N-1} | \psi(\mathbf{x}) | \Psi_0 \rangle$ and $P_m(\mathbf{x}) = \langle \Psi_0 | \psi(\mathbf{x}) | \Psi_m^{N+1} \rangle$. Using these equations we can find an expression for the so-called spectral function $A(\omega) = i[G^>(\omega) - G^<(\omega)]$ that reads

$$\begin{aligned} A(\mathbf{x}, \mathbf{x}, \omega) = {} & 2\pi \sum_m |Q_m(\mathbf{x})|^2 \delta(\omega - E_0 + E_m^{N-1}) \\ & + 2\pi \sum_m |P_m(\mathbf{x})|^2 \delta(\omega - E_m^{N+1} + E_0). \end{aligned} \tag{3.10}$$

This quantity is important in photoemission and inverse photoemission experiments, as it describes the probability that an electron emitted or absorbed at a point $\mathbf{x}$ will have the energy ω. Knowledge of the Green's function G thus allows us both to extract information about one-particle properties in the system, but also to access its spectral features. Now that we know how to use the Green's function, we discuss in the next section how to construct reasonable approximations to calculate G.

3.1.2 Approximating the self-energy

As pointed out earlier, to solve the Kadanoff-Baym equations for G we need to find an approximate expression for the self-energy Σ. To approach this issue we make the observation

that in the definition of the Green's function (given in Eq. 3.2), the interaction Hamiltonian only enters at one point, namely in the exponent. This allows us to write the trace as an expansion in powers of the interaction according to

$$iZG(a,b) = \sum_k \frac{(-i)^k}{k!} \int_\gamma dz_1 \dots dz_k \, \mathrm{Tr}\left[\mathcal{T} e^{-i\int_\gamma dz T(z)} U(z_1)\dots U(z_k)\psi(a)\psi^\dagger(b)\right]. \tag{3.11}$$

Since in this expression the trace is taken with the non-interacting Hamiltonian T, and the interaction Hamiltonian U contains two pairs of creation and annihilation operators, this equation gives G as an expansion in the non-interacting $(2n+1)$-particle Green's functions $G_{0,2n+1}$. Each such non-interacting Green's function can, using Wick's theorem [38, 39], be written as a $(2n+1)\times(2n+1)$ determinant of non-interacting single-particle Green's functions G_0 [36]. Similarly the partition function Z can be written as an expansion in the non-interacting Green's functions $G_{0,2n}$, and so the interacting single-particle function G is completely determined by an expansion in G_0.

The question now becomes: How can we structure this expansion in such a way that it becomes practical to handle? It was realized by Feynman [31] that the series can be depicted using simple diagrams, today known as Feynman diagrams, and then turned into exact mathematical expressions by a set of prescribed rules. It can be shown that in the expansion for G only the connected and topologically distinct diagrams need to be considered [36, 39], and that the structure of the expansion has the general structure

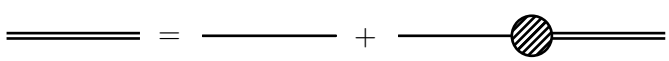

Here the double line denotes G, the single line G_0, and the filled circle the self-energy Σ, and written as an equation we have

$$G(1,2) = G_0(1,2) + \int_\gamma d3d4 G_0(1,3)\Sigma(3,4)G(4,2). \tag{3.12}$$

This is known as Dyson's equation, and is equivalent to the Kadanoff-Baym equation. The equation implicitly defines the self-energy in terms of diagrams, which can be drawn either in terms of the non-interacting G_0 or the interacting G. We will use the later approach for two reasons: Firstly, the explicit expression for Σ in terms of G contains less diagrams than in terms of G_0, and so is easier to handle. Secondly, the expression in terms of G implicitly contains more diagrams, since each line in Σ representing G contains an infinite number of self-energy insertions [36]. In this sense, an expansion of Σ to finite order in G contains a whole class of diagrams from the expansion of Σ in terms of G_0.

We now discuss the most common approximations for Σ. The easiest possible approximation is to truncate the expansion of Σ at first order in the interaction, which corresponds to

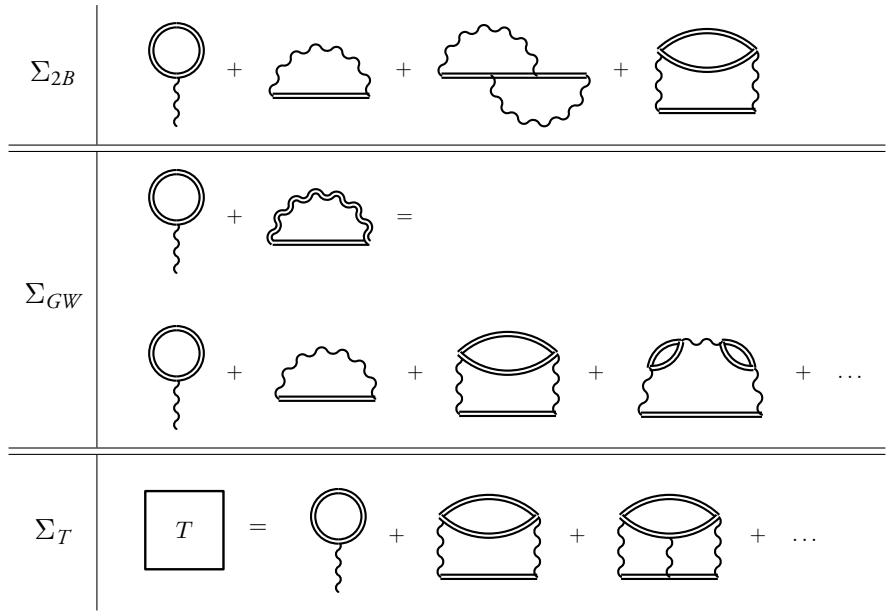

Figure 3.2: Feynman diagrams for the self-energy in second Born, GW and T-matrix approximations. The self-energies Σ_{GW} and Σ_T are obtained by summing the so-called bubble or ladder diagrams to infinite order.

the Hartree-Fock (HF) approximation. If instead the expansion is truncated at second order, we obtain the second Born (2B) approximation corresponding to the diagrams shown in the first row of Fig. 3.2. A different approach to constructing approximations for Σ is to include a whole class of diagrams that can be summed to infinite order. We have used two such approximations, known as the GW and T-matrix approximations, for which the diagrams are shown in Fig. 3.2. In the GW approximation we define an additional quantity, the screened interaction W, which is obtained from the sum of all so-called bubble diagrams (as indicated in Fig. 3.2). These diagrams describe particle-hole excitations in the material, and thus account for polarization effects. However, in contrast to the 2B approximation, the GW diagrams only describe exchange to first order. The screened interaction is usually depicted by a double wavy line, as shown in Fig. 3.2. In the T-matrix approximation we also define an additional quantity, the transfer matrix T, which is obtained from the sum of the so-called ladder diagrams. It describes repeated particle-particle and particle-hole scattering, and is expected to perform well for low particle density and short-range interactions [36, 39]. For brevity we only show the generic structure of the T-matrix diagrams in Fig. 3.2, and neglect both exchange diagrams and the distinction between particle-particle and particle-hole scattering. We note that the GW and T-matrix approximations are computationally more expensive than 2B, since W and T have to be solved for self-consistently together with Σ and G.

3.1.3 Embedding self-energy

An attractive feature of the NEGF method is that it is possible to give an exact treatment of a small system connected to a number of non-interacting heat and particle reservoirs. This is due to the fact that the self-energy Σ_{ij} is non-zero only if both i and j correspond to states in the interacting region (since any self-energy diagram starts and ends with an interaction line). To make this observation more formal, we divide the system into an interacting region c, and a number of non-interacting reservoirs $i = 1, 2, \ldots, n_R$. If we write the matrix elements of the Kadanoff-Baym equation corresponding to two indexes in c, and one each in i and c, we find the equations

$$\begin{aligned}\left[i\frac{\partial}{\partial z} - h_{cc}(z)\right] G_{cc}(z,z') &= \delta(z,z') + \sum_i h_{ci}(z)G_{ic}(z,z') + \int_\gamma d\bar{z}\,\Sigma_{cc}(z,\bar{z})G_{cc}(\bar{z},z') \\ \left[i\frac{\partial}{\partial z} - h_{ii}(z)\right] G_{ic}(z,z') &= h_{ic}(z)G_{cc}(z,z') \end{aligned} \tag{3.13}$$

Since the last equation has a vanishing interaction kernel, it can be solved using the mathematical Green's function method, and is given by

$$G_{ic}(z,z') = \int_\gamma d\bar{z}\, g_{ii}(z,\bar{z})h_{ic}(\bar{z})G_{cc}(\bar{z},z'). \tag{3.14}$$

Here g_{ii} is the solution of the homogeneous equation $[i\partial_z - h_{ii}(z)]g_{ii}(z,z') = \delta(z,z')$, with the same boundary conditions as G. Using this solution in the equation of motion for G_{cc} closes the equation to

$$\left[i\frac{\partial}{\partial z} - h_{cc}(z)\right] G_{cc}(z,z') = \delta(z,z') + \int_\gamma d\bar{z}\,[\Sigma_{emb}(z,\bar{z}) + \Sigma_{cc}(z,\bar{z})]G_{cc}(\bar{z},z'), \tag{3.15}$$

where we have defined the embedding self-energy $\Sigma_{emb} = \sum_i h_{ci}(z)g_{ii}(z,z')h_{ic}(z')$. Since g_{ii} satisfies the equation of a non-interacting Green's function, it can be found analytically from the eigenvalues of the matrix h_{ii}. In other words, the exact dynamics of the central region c can be obtained by solving an equation restricted to this region, even in presence of reservoirs.

3.1.4 Generalized Kadanoff-Baym ansatz

To solve the Kadanoff-Baym equations in practice is very numerically demanding, since the two-time dependence of $G(1,2)$ and the inclusion of memory makes the time-propagation scale with the number of time-steps n_t like $\mathcal{O}(n_t^3)$. This is to be compared with methods like exact diagonalization or TDDFT where the time-evolution scales linearly with the number

of time-steps. Since most observables can be found from the single-particle density matrix $\rho(t) = -iG^<(t,t)$, and propagating this one-time quantity would give a more favorable scaling with n_t, it is reasonable to ask if it is possible to write an equation for ρ starting from the Kadanoff-Baym equations. We will now show that this is the case, by using what is known as the generalized Kadanoff-Baym ansatz (GKBA).

For a system at zero temperature taking the difference between the equation of motion for $G^<$ and its adjoint gives (in matrix form)

$$\frac{\partial}{\partial t}\rho(t) + i[h_{HF}(t), \rho(t)] = -\left(I^<(t,t) + h.c.\right), \tag{3.16}$$

where we have separated out the Hartree-Fock part from the self-energy. The right-hand side is the so-called collision integral $I^<$, which can be written in terms of the retarded and advanced Keldysh components $G^R(t,t') = \theta(t-t')[G^>(t,t') - G^<(t,t')]$ and $G^A(t,t') = [G^R(t',t)]^\dagger$ as

$$I^<(t,t) = \int_{-\infty}^{\infty} dt' \left[\Sigma^<(t,t')G^A(t',t) + \Sigma^R(t,t')G^<(t',t)\right]. \tag{3.17}$$

Since this equation contains $G^<$ for off-diagonal time arguments, it is not a closed equation for ρ. To proceed we use the fact that Dyson's equation for $G^<$ can be reformulated as an expansion in ρ and $G^{R/A}$ [40], which to lowest order reads $G^<(t,t') = -G^R(t,t')\rho(t') + \rho(t)G^A(t,t')$. Keeping only this leading term constitutes the GKBA, and closes the equation for ρ provided we know $G^{R/A}$. These functions are usually taken to be the Hartree-Fock solutions, since then the GKBA is exact when the collision integral vanishes. In the general case this is of course an approximation, and is expected to work well as long as a quasi-particle description of the system is appropriate. It should be noted that other choices are possible for the retarded propagator [41], and that the specific choice can be of particular importance for open systems. As further discussed in Chapter 5, we used the GKBA in Paper IV to study charge-separation in a prototypical donor-acceptor system.

3.2 Density functional theory and GW

In Paper III we studied multi-photon absorption of InAs nanowires by performing ground state DFT calculations. However, to predict the absorption signal it is important to correctly described the band structure and in particular the band gap of the system, which is known to be underestimated by DFT. For InAs, where the experimental band gap is only $E_g \sim 0.6$ eV, the situation is even worse since many calculations predict a vanishing or even negative band gap. To improve upon this situation we extended the DFT treatment to include many-body corrections at the GW level, which renormalizes the quasi-particle energies and opens up a gap. In this section we briefly describe how this is done.

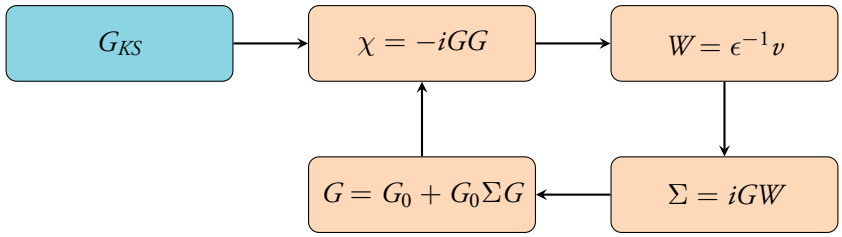

Figure 3.3: Self-consistency cycle of the combined DFT and GW calculations. We start by constructing the Kohn-Sham Green's function G_{KS}, and use it to find the polarization χ. From χ we obtain the dielectric function ϵ and the screened interaction W, which is used to construct the self-energy Σ.

Since the Kohn-Sham system describes non-interacting particles, the Kohn-Sham Green's function G_{KS} satisfies the Kadanoff-Baym equation with $\Sigma = 0$. This makes it possible to solve explicitly for G_{KS}, which can be written in Fourier space as

$$G_{KS}(\mathbf{k},\omega) = \sum_{\epsilon_i<\epsilon_F} \frac{\psi_i(\mathbf{k})\psi_i^*(\mathbf{k})}{\omega - \epsilon_i - i\eta} + \sum_{\epsilon_i>\epsilon_F} \frac{\psi_i(\mathbf{k})\psi_i^*(\mathbf{k})}{\omega - \epsilon_i + i\eta}. \tag{3.18}$$

Here ϵ_i and ψ_i are the Kohn-Sham energies and orbitals, and ϵ_F the Fermi energy of the system. The purpose of the GW corrections is to improve the single-particle energies ϵ_i and wavefunctions ψ_i, through the self-consistency cycle shown in Fig. 3.3. The calculation starts by constructing the polarization $\chi(1,2) = -iG_{KS}(1,2)G_{KS}(2,1^+)$, from which the screened interaction can in principle be found by solving the Dyson equation for W. However in practice it is more efficient to construct the dielectric function $\epsilon(1,2) = \delta(1,2) - \int d3v(1,3)\chi(3,2)$, in terms of which $W = \int d3\epsilon^{-1}(1,3)v(3,2)$. Finally the self-energy is obtained from $\Sigma(1,2) = iG(1,2)W(1^+,2)$. In principle the cycle can be iterated until self-consistency is reached by constructing a new G from the Dyson equation (Eq. 3.12). However, experience has shown that even though self-consistency tends to improve the total energy, it typically does not improve the spectral features of the system. How to apply the GW theory in practice is therefore a complex problem, and depends both on the system we consider and the quantity we are interested in computing [42]. To calculate the single-particle band structure it is common to do only one iteration in order to find Σ (so-called one-shot GW), and then find the energies and wavefunctions by solving the quasi-particle equation [43]

$$[h(\mathbf{r}_1) + v_H(\mathbf{r}_1)]\,\psi(\mathbf{r}_1) + \int d\mathbf{r}_2 \Sigma(\mathbf{r}_1,\mathbf{r}_2,\epsilon_{qp})\psi(\mathbf{r}_2) = \epsilon_{qp}\psi(\mathbf{r}_1). \tag{3.19}$$

If we are only interested in the energies this equation can be solved to first order in $\epsilon_{qp} - \epsilon_{KS}$ by $\epsilon_{qp} = \epsilon_{KS} + Z\langle\psi_{KS}|\Sigma(\epsilon_{KS}) - v_{xc}|\psi_{KS}\rangle$, where Z is the so-called renormalization factor.

3.2.1 Wannier functions and interpolation

To calculate the rate of multiphoton absorption, to be discussed in detail in Chapter 4, it is necessary to find the dipole transition matrix elements $\mathbf{M}_{v\mathbf{k}c\mathbf{k}'} = \langle\psi_{c\mathbf{k}'}|\mathbf{d}|\psi_{v\mathbf{k}}\rangle$. For the calculations in Paper III it was necessary to include on the order of 10^5 k-points for the results to converge, which is far beyond what is feasible to include explicitly in a GW calculation. To address this issue we used an interpolation of the matrix elements based on Wannier functions [44], which will be discussed in this section.

The Wannier functions are localized orbitals centered at a given lattice site $\mathbf{R}$ of the crystal, which can be obtained from the Bloch functions $\psi_{n\mathbf{k}}$ by a unitary transformation

$$w_{n\mathbf{R}}(\mathbf{r}) = \frac{V}{(2\pi)^3}\int d\mathbf{k}\sum_m U^{\mathbf{k}}_{mn}\psi_{m\mathbf{k}}(\mathbf{r})e^{-i\mathbf{k}\cdot\mathbf{R}}. \tag{3.20}$$

This transformation is not unique, since different choices of the Bloch periodic functions $u_{n\mathbf{k}} = \sum_m U^{\mathbf{k}}_{mn}u_{m\mathbf{k}}$ will give different Wannier functions [45]. This gauge freedom can be utilized to find a set of maximally localized Wannier functions, defined as the set that minimizes the spread functional $\Omega = \sum_n[\langle\mathbf{r}_n^2\rangle - \langle\mathbf{r}_n\rangle^2]$. Once the Wannier functions have been constructed we can invert the above transformation to get a new set of Bloch functions $\psi^W_{v\mathbf{k}}$, where the index W indicates that these functions are reconstructed from the Wannier orbitals. Since the transformation is valid for any $\mathbf{k}$, not just those of the original k-point grid, we can now write the matrix elements

$$\mathbf{M}_{v\mathbf{k}c\mathbf{k}} = \langle\psi^W_{c\mathbf{k}}|\mathbf{d}|\psi^W_{v\mathbf{k}}\rangle = \sum_{\mathbf{R}} e^{i\mathbf{k}\cdot\mathbf{R}}\langle w_{c0}|\mathbf{d}|w_{v\mathbf{R}}\rangle. \tag{3.21}$$

This process is known as Wannier interpolation, and we now briefly discuss its validity. Given a set of Bloch functions defined on a k-grid of size $N_k \times N_k \times N_k$, the corresponding Wannier functions will be periodic over a supercell of size $L \times L \times L$, where $L = N_k a$ and where a is the lattice parameter. The purpose of defining maximally localized Wannier functions is that for a given N_k, if the Wannier functions decay fast enough that for $r = L/2$ they are essentially zero, any property computed from the Wannier functions will be insensitive to a further increase of N_k [46]. By converging the Wannier functions with respect to N_k we can then safely use these functions for interpolation. In Paper III the convergence was ensured by demanding that the band structure obtained from the Wannier functions reproduced the band structure of the GW calculations.

Chapter 4

Elements of non-linear spectroscopy

In this chapter we give a brief review of the classical theory of light-matter interactions, and make a distinction between linear and non-linear effects. We then discuss how to connect the classical equations to an underlying microscopic description of matter, which is used to calculate the multi-photon absorption of InAs nanowires (Sec. 4.1). In the following section we address how light is affected by the non-linear interaction with matter (Sec. 4.2). For this purpose we use a quantum description of the light field and study multi-photon effects in a two-level system. Although forbidden in a perturbative treatment, we show that second order harmonics can appear in a non-perturbative description due to mixing of the atomic orbitals by the interaction with light. We also present results for the fluorescence spectrum of a two-level atom, and identify signatures of quantum radiation.

4.1 Multi-photon absorption

The equations that describe the electromagnetic properties of a material are the macroscopic Maxwell equations, which if we neglect the magnetic field and assume no macroscopic currents are given by [47]

$$\epsilon_0 \nabla \cdot \mathbf{E}(\mathbf{r}, t) + \nabla \cdot \mathbf{P}(\mathbf{r}, t) = \rho(\mathbf{r}, t) \tag{4.1a}$$

$$\nabla \times \mathbf{E}(\mathbf{r}, t) = 0. \tag{4.1b}$$

This assumption corresponds to neglecting effects of a finite wavelength, consistent with the dipole approximation discussed below. The macroscopic response of matter to external electromagnetic radiation is contained in the polarization vector $\mathbf{P}(\mathbf{r}, t)$, which is defined as the density of dipole moments. For weak electromagnetic fields the dependence of the polarization on the electric field is linear, and can for a homogeneous system be written

as [48]

$$P_i(t) = \epsilon_0 \int_{-\infty}^{t} dt' \chi_{ij}(t, t') E_j(t'). \tag{4.2}$$

Here $i \in (1, 2, 3)$ denotes the component of the polarization vector, and χ_{ij} is the retarded susceptibility tensor that takes into account the memory of the system as well as its (possibly) non-isotropic response. For systems in equilibrium the susceptibility depends only on the time difference $t - t'$, and the equation above is more conveniently written in frequency space as $P_i(\omega) = \epsilon_0 \chi_{ij}(\omega) E_j(\omega)$. For stronger electromagnetic fields the polarization must be written as an expansion in the electric field, and is with the assumption of an instantaneous material response (to simplify the equations) given by [49]

$$P_i(t) = \chi_{ij}^{(1)} E_j(t) + \chi_{ijk}^{(2)} E_j(t) E_k(t) + \chi_{ijkl}^{(3)} E_j(t) E_k(t) E_l(t) + \dots, \tag{4.3}$$

In this equation the higher order terms define the *non-linear* response of the system. In many cases the electric field strength $E = |\mathbf{E}|$ is weak enough that the non-linear terms become negligible. However, with present technologies is it possible to create pulsed lasers with a duration on the femto- or attosecond scale [50], and to reach field strengths of the same order of magnitude (and significantly stronger) as the characteristic energy scales of atomic and solid-state materials. Under such conditions, the non-linear terms are of great importance for the understanding and interpretation of experiments.

We now show how to calculate the photon absorption to lowest order, and discuss the relation between the total absorption rate and the linear susceptibility. Fundamentally the susceptibility must have its origins in microscopic light-matter processes, where individual electrons absorb or emit photons and thereby change their internal state. The chance for such a process to happen is quantified by the transition probability $\mathcal{P}_{a \to b}$, describing the probability that an electron initially in state $|a\rangle$ transfers into state $|b\rangle$ due to the action of an external perturbing field.

For simplicity we specialize to gapped solid state systems, like semiconductors and insulators, where the total Hamiltonian can be written as $H = H_0 + H(t)$. We assume that the equilibrium Hamiltonian H_0 can be treated using an effective single-particle theory like DFT, and that it has eigenstates $|\psi_{n\mathbf{k}}\rangle$ of energy $\epsilon_{n\mathbf{k}}$. The zero temperature ground state will consist of completely filled valence bands denoted by $n = v$, and completely empty conduction bands denoted by $n = c$, so that the quantum numbers of the initial and final states of the transition probability are $a = v\mathbf{k}$ and $b = c\mathbf{k}'$. The time-dependent perturbation is given by a monochromatic electric field, for which the interaction Hamiltonian can be written as $H(t) = e\mathbf{d} \cdot \mathbf{E} \sin(\omega t)$ in the Göppert-Mayer gauge [49]. To obtain this Hamiltonian we have used the dipole approximation, in which it is assumed that the spatial dependence of the electric field can be neglected since it varies over length scales large

compared to the characteristic lengths of the system. The transition probability for photon absorption is to lowest order given by [51]

$$\mathcal{P}_{v\mathbf{k}\to c\mathbf{k}'}(\omega) = \frac{2\pi}{\hbar}\,(eE)^2\,\delta_{s_c s_v}\,|\mathbf{e}\cdot\mathbf{M}_{v\mathbf{k}c\mathbf{k}'}|^2\,\delta(\epsilon_{c\mathbf{k}'} - \epsilon_{v\mathbf{k}} - \hbar\omega), \tag{4.4}$$

where $\mathbf{M}_{v\mathbf{k}c\mathbf{k}'} = \langle\psi_{c\mathbf{k}'}|\mathbf{d}|\psi_{v\mathbf{k}}\rangle$ is a dipole matrix element.

A consequence of the dipole approximation is that only vertical transitions (where $\mathbf{k}' = \mathbf{k}$) are allowed. This follows directly from group theoretical arguments [51], by noting that since $\mathbf{d}$ is the dipole operator in the primitive unit cell, it transforms according to the identity representation under lattice translations ($T_{\mathbf{R}}\mathbf{d} = \mathbf{d}$). Since a Bloch state with vector $\mathbf{k}$ belongs to the irreducible representation labeled by $\mathbf{k}$, the matrix element $\mathbf{M}_{v\mathbf{k}c\mathbf{k}'}$ is zero unless $\mathbf{k}' = \mathbf{k}$. The transitions are called vertical since they correspond to photons with zero momentum, and therefore connect states of the band structure along a vertical line. The total rate W of absorbed photons is obtained by summing over all possible initial and final states [51],

$$W(\omega) = \frac{4\pi}{\hbar}\,(eE)^2 \sum_{cv\mathbf{k}} |\mathbf{e}\cdot\mathbf{M}_{vc\mathbf{k}}|^2\,\delta(\epsilon_{c\mathbf{k}} - \epsilon_{v\mathbf{k}} - \hbar\omega). \tag{4.5}$$

In the special case where the matrix elements are constant, $\mathbf{M}_{vc\mathbf{k}} = \mathbf{M}$, the rate is proportional to the density of states $\rho(\epsilon_{c\mathbf{k}} - \epsilon_{v\mathbf{k}} - \hbar\omega)$. If we are interested mainly in the absorption rate for energies close to the band gap, taking $\mathbf{M}_{vc\mathbf{k}}$ constant is usually a good approximation, but in the general case effects due to the matrix elements are important.

To find the linear susceptibility we note that it is closely related to the dielectric tensor $\epsilon_{ij}(\omega) = 1 + \chi_{ij}(\omega)$, which has a clear physical interpretation. The real part of $\epsilon(\omega)$ gives the refraction of radiation propagating through a material, while its imaginary part is related to the absorption rate by $\mathrm{Im}\epsilon(\omega) = 2\pi\hbar/(m\omega E)^2\,W(\omega)$ [51]. Due to the causal property of the susceptibility ($\chi = 0$ for $t' > t$), the dielectric function is analytic in the upper half of the complex plane. This allows for the real part to be extracted from the imaginary part by a Hilbert transform, and implies that a full knowledge of either the real or imaginary part of the dielectric function is enough to completely determine the whole function. This is referred to as the Kramers-Kronig relation [52]. To obtain the linear susceptibility it is therefore sufficient to determine the total absorption rate $W(\omega)$ for all values of ω.

For more intense external radiation we need to extend the calculations above to higher orders in the electric field. To simplify the notation we use $\epsilon_{ab\mathbf{k}} = \epsilon_{a\mathbf{k}} - \epsilon_{b\mathbf{k}}$ to denote the transition energies, and assuming all absorbed photons have the same frequency ω the second and third order absorption rates are given by

$$W_{2p}(\omega) = \frac{8\pi}{\hbar}\,(eE)^4 \sum_{cv\mathbf{k}} \left| \sum_{\alpha} \frac{\mathbf{e}\cdot\mathbf{M}_{c\alpha\mathbf{k}}\,\mathbf{e}\cdot\mathbf{M}_{\alpha v\mathbf{k}}}{\epsilon_{\alpha v\mathbf{k}} - \hbar\omega} \right|^2 \delta(\epsilon_{cv\mathbf{k}} - 2\hbar\omega) \tag{4.6a}$$

$$W_{3p}(\omega) = \frac{24\pi}{\hbar}(eE)^6 \sum_{cv\mathbf{k}} \left| \sum_{\beta\alpha} \frac{\mathbf{e}\cdot\mathbf{M}_{c\beta\mathbf{k}}\,\mathbf{e}\cdot\mathbf{M}_{\beta\alpha\mathbf{k}}\,\mathbf{e}\cdot\mathbf{M}_{\alpha v\mathbf{k}}}{(\epsilon_{\beta v\mathbf{k}} - 2\hbar\omega)(\epsilon_{\alpha v\mathbf{k}} - \hbar\omega)} \right|^2 \delta(\epsilon_{cv\mathbf{k}} - 3\hbar\omega). \quad (4.6b)$$

In contrast to the first order absorption rate these expressions contain a sum over virtual transitions. Note however that we have neglected virtual transitions where photons are emitted, which should be taken into account for a general absorption measurement. The reason for this is that we will use the transition rates to model photo-emission from InAs nanowires, where the value of the work function stops these transitions from contributing to the photo-emission process. For this application we need to extract the energies $\epsilon_{n\mathbf{k}}$ and matrix elements $\mathbf{M}_{cv\mathbf{k}}$ from some microscopic calculation, as discussed in the next section.

4.1.1 Polarization dependence in InAs nanowires

One method to study the non-linear response of a material is to exploit the local field enhancement from nanostructures. The field enhancement depends strongly both on the morphology of the structure and the polarization of the incident field, and can be controlled by varying the polarization [53, 54, 55]. Most studies of the non-linear response in nanostructures have used noble metals, which are favorable due to their strong surface-plasmon response. In Paper III we instead study semi-conductor nanostructures, since their response is expected to show an interesting interplay between polarization dependence, morphology and crystal structure [56]. In addition, these materials are important since semi-conductor materials are commonly used in the fabrication of electronic components [57]. Until recently, electronic devices could be made faster by reducing the size of the individual components, but since today their size is close to the atomic scale a further shrinking is no longer possible. A possible way to increase the speed of electronic devices is instead to use plasmons to carry opto-electronic signals, since these are both highly confined and propagate with a high group velocity [58]. This requires an understanding of the non-linear response of semi-conductor nanostructures in the regime where quantum effects become important.

In Paper III we studied the photoabsorption of InAs nanowires with segments selectively grown in the zincblende or wurtzite phase. The nanowires were placed on a SiO substrate and studied by photoemission electron microscopy (PEEM) [59]. The nanowire morphology and experimental setup are shown in Fig. 4.1. As seen in the figure the light grazes the substrate at an angle of 65° and makes an angle α with the nanowire axis. The wires were grown so that the wurtzite c-axis is parallel to the nanowire axis. The non-linear photoemission signal was obtained by subjecting the nanowires to a train of infrared laser pulses with a duration of 6.1 fs and a central frequency of 800 nm. Since the pulses are localized in the time domain their spectral profile becomes broadened, and is non-zero in the range $1.2 < \hbar\omega < 1.8$ eV. The experiment measured the photoemission signal for the zincblende and wurtzite segments as a function of the polarization angle θ, and it was

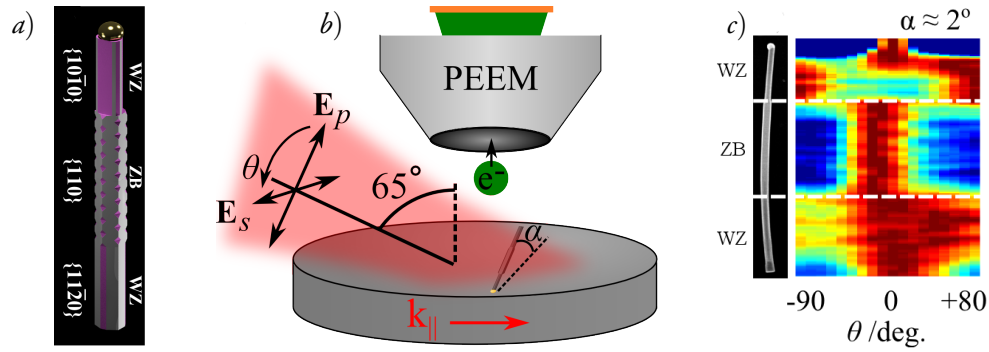

Figure 4.1: Panel (a) shows a a schematic of the nanowire morphology, with a gold nanoparticle at the top, followed by a wurtzite segment, a zincblende segment and a second wurtzite segment. Panel (b) shows the experimental setup used to study the non-linear photoemission signal for InAs nanowires. In panel (c) the photo-emission signal is shown as a function of the polarization angle θ for a nanowire with $\alpha \approx 2^\circ$. The figures are adapted from Paper III.

found that the signal depends differently on the polarization in the two crystal phases (see Figs. 4.1*c* and 4.2*c*). Since the polarization behavior was most clear for nanowires aligned so that $\alpha \approx 0$, we restrict the following discussion to this case. For this alignment of the wires a polarization $\theta = 0^\circ$ corresponds to a field perpendicular to the nanowire axis, while $\theta = 90^\circ$ correspond to a field along the axis. As seen in Fig. 4.1, the measured signal for the zincblende segments is strongest for a polarization angle $\theta = 0^\circ$, while for the wurtzite segments the photoemission is strongest for $\theta = 90^\circ$.

The behavior of the zincblende segment can be understood from the nanowire morphology, that gives a strong field enhancement for $\theta = 0^\circ$. If the system had no microscopic polarization dependence, the strongest signal should be observed at this polarization angle since the photoemission signal is proportional to the local electric field. In the wurtzite segment, where the opposite result is observed, the behavior must therefore be due to the crystal structure. To explain the polarization dependence of the wurtzite segments we calculated the rates for one-, two- and three-photon absorption using a generalized version of Eqs. 4.5 and 4.6. The modified equations take into account the finite pulse envelope, which allows photons of different energy to be absorbed. Since the resulting formulas are quite lengthy they are not reproduced here. We note that our simulations do not cover the entire photoemission process, but only the initial photoabsorption step. Although photoemission can be rigorously addressed in the linear regime [60], a treatment of multi-photon photoemission for realistic systems is currently out of reach (except for model applications, see [61]). Assuming an isotropic photoemission event, we expect any anisotropy of the photoabsorption process to be reflected also in the photoemission signal, and therefore restrict to this process.

To predict the absorption signal we need to extract the energies $\epsilon_{n\mathbf{k}}$ and matrix elements $\mathbf{M}_{cv\mathbf{k}}$ from some microscopic calculation. It is then important to correctly describe the

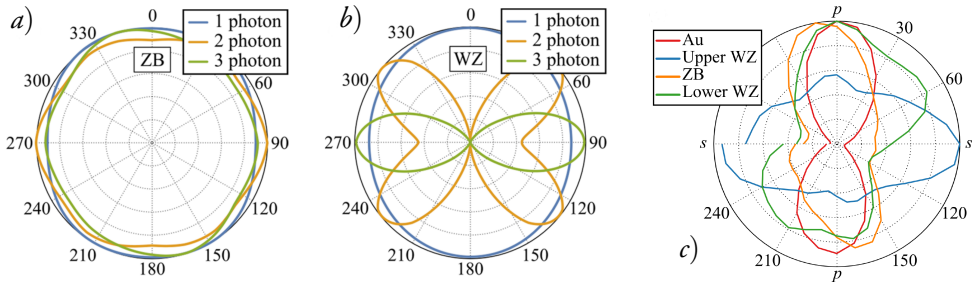

Figure 4.2: In panels (a) and (b) we show the calculated multi-photon absorption rates from the zincblende and wurtzite InAs structures respectively. Panel (c) shows the polarization dependence of the experimental photoemission signal from the nanowire in Fig. 4.1c. The different curves correspond to the segments of the nanowire shown in Fig. 4.1a and 4.1c. The figures are adapted from Paper III.

band structure and in particular the band gap of the system, which is known to be underestimated by DFT. For wurtzite InAs, where the experimental band gap is only $E_g \sim 0.6$ eV, the situation is even worse since many DFT calculations predict a vanishing or even negative band gap. This issue has been discussed in detail in [62], and was found to be due to the neglect of the $4d$ electrons in most common pseudopotentials. To calculate the energies $\epsilon_{n\mathbf{k}}$ and matrix elements $\mathbf{M}_{cv\mathbf{k}}$, we therefore used the ABINIT package to perform self-consistent quasi-particle GW simulations on top of the original DFT results. This was done for both zincblende and wurtzite InAs in bulk. Since the GW calculations are time intensive they were performed on an $8 \times 8 \times 8$ Monkhorst-Pack grid [63] with a total of 512 k-points. However, to converge the absorption rates a grid with about 10^5 k-points is necessary, and for this purpose we used the WANNIER90 and associated POST90 packages to interpolate the energies and matrix elements. A more extensive discussion of the methodology is provided in Sec. 3.2.

The calculated photoabsorption rates for zincblende InAs show no polarization dependence (see Fig. 4.2a), which is expected since the zincblende structure has no preferred crystal axis. For the wurzite structure on the other hand (Fig. 4.2b), the multi-photon absorption rates show a strong polarization dependence, that also varies between the one-, two- and three-photon signals. We find that the three-photon absorption rate is in good agreement with the experimental photo-emission signal (see Fig. 4.2c), showing a strong enhancement for a field along the wurtzite c-axis. Since the work function of InAs is about 4.9 eV [64], we expect at least four photons are necessary to give a photoemission signal. This is also observed experimentally, where the photoemission signal was found to scale as E^{2n} with $n = 4$, which is the expected behavior for a four-photon process. If we assume that three photons are involved in the photoabsorption, while the fourth gives rise to a final isotropic photoemission event, we therefore expect the photoemission signal to resemble the signal of the three-photon absorption rate. From this we conclude that the observed polarization behavior is most likely due to the microscopic features of the wurtzite structure.

4.2 Second harmonic generation

In the previous section we discussed the non-linear response of a system to radiation, under the assumption that the radiation itself is unaffected by the interaction with matter. We now change focus and investigate what happens with the *light* during light-matter interactions. We focus here on the second-order polarization, which can be written [48]

$$P_i^{(2)}(t) = \epsilon_0 \int dt' dt'' \chi_{ijk}^{(2)}(t-t', t-t'') E_j(t') E_k(t''). \tag{4.7}$$

If the incident radiation is monochromatic, so that $\mathbf{E}(t) = \mathbf{E}(e^{i\omega t} + e^{-i\omega t})$, we can rewrite the polarization as [49]

$$P_i^{(2)}(t) = \epsilon_0 \left(\chi_{ijk}^{(2)}(\omega, \omega)[e^{2i\omega t} + e^{-2i\omega t}] + 2\chi_{ijk}^{(2)}(\omega, -\omega) \right) E_j E_k, \tag{4.8}$$

where χ has been transformed to Fourier space. We see that the polarization contains terms oscillating at the twice the original frequency, as well as terms where the time-dependence has canceled out. The first are known as frequency doubling terms, since solving the wave equation with this polarization gives rise to components in the electric field oscillating at twice the frequency of the incoming radiation [49]. The second type of terms are known as optical rectification terms since they give rise to a constant polarization. In an analogous way the nth-order polarization (if non-zero) leads to the production of radiation at frequencies $\pm n\omega$, in a process known as nth-order harmonic generation. Experimentally the high harmonic generation in atomic systems is of great importance, since it underlies the production of laser pulses of sub-femtosecond duration [65]. This however requires high intensities of the driving laser, and for more moderate fields typically the lowest available harmonic will dominate. In particular, second harmonic generation in non-linear crystals is routinely used for up- and down-conversion of incoming light to twice or half the original frequency, which allows to tune laser sources over a large frequency range. In the following we restrict the discussion to second harmonic generation (SHG).

In the perturbative regime we can find an explicit expression for the second order polarization. Writing the Hamiltonian in the dipole approximation as $H = H_0 + \mathbf{d} \cdot \mathbf{E}(t)$, where H_0 describes the material system, the second order Kubo formula gives [39]

$$P_i^{(2)}(t) = \int dt' dt'' \langle \Psi | [[d_i(t), d_j(t')], d_k(t'')] | \Psi \rangle E_j(t') E_k(t''), \tag{4.9}$$

where the dipole operators $\mathbf{d}$ are in the Heisenberg picture with respect to H_0. If H_0 is invariant under parity transformations, the ground state $|\Psi_0\rangle$ and the excited states $|\Psi_i\rangle$ of H_0 will be of definite parity. Inserting a complete set of states between each of the dipole operators, and using that $\langle \Psi_i | \mathbf{d} | \Psi_j \rangle = 0$ for states of equal symmetry, we find that $\chi^{(2)} = 0$ for such systems. Since this argument only relies on the fact that the number

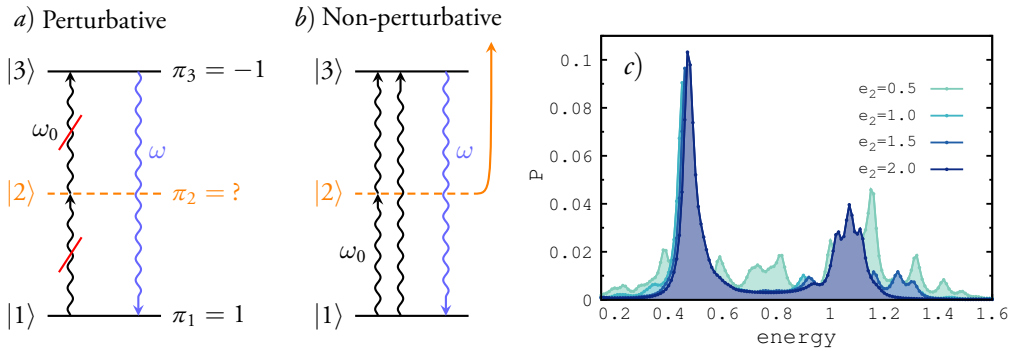

Figure 4.3: Schematic illustration of a three-level system. For a parity invariant Hamiltonian and in the perturbative limit (a), second harmonic generation (SHG) is forbidden. In a non-perturbative treatment (b), level mixing allows for SHG. Panel (c) shows the fluorescence spectrum of the three-level system (see Eq. 4.18) as a function of ω and ϵ_2, for $\epsilon_1 = 0$, $\epsilon_3 = 1$ and $\omega_0 = 0.5$. The figures are adapted from Paper VI.

of dipole operators entering the expression for $\chi^{(2)}$ is odd, it can easily be extended to show that $\chi^{(2n)} = 0$ for all n. If on the other hand the Hamiltonian H_0 breaks parity, the argument no longer holds, and $\chi^{(2n)} \neq 0$.

A common model to study SHG consists of three atomic levels coupled to an incident and a fluorescent electromagnetic field, as schematically illustrated in Fig. 4.3a. In order to obtain a second harmonic signal in the perturbative limit, the parities π_1 and π_3 of levels $|1\rangle$ and $|3\rangle$ need to be different (for the fluorescent transition to be allowed), while the parity π_2 of level $|2\rangle$ needs to be different both from π_1 and π_3 (in order for the exciting transitions to be allowed). For states of definite parity this configuration is impossible to achieve, exemplifying the above conclusion that SHG is forbidden for parity invariant Hamiltonians. It is worthwhile to consider in more detail the limitations of the argument above. By using perturbation theory we have implicitly assumed that the eigenstates of H are similar to the eigenstates of H_0. For weak light-matter interactions this approximation is well justified, and in this regime perturbation theory should give results in close agreement with a non-perturbative solution. However, for stronger interactions, renormalization of the eigenstates becomes important, and there is no *a priori* justification of the perturbative results.

Therefore consider again the three level system in the non-perturbative limit. As we will see below, the light-matter coupling mixes electron-photon states in such a way that the electronic levels no longer have a definite parity. This allows for all transitions in the three-level system discussed above, but also for the additional direct transition from level $|1\rangle$ to $|3\rangle$ (see Fig. 4.3b). Therefore, in the non-pertubative limit, SHG is possible. As a thought experiment we can also consider shifting the intermediate level $|2\rangle$ away from resonance with the incident field. In Paper VI we considered this experiment and studied the fluorescence spectrum as the energy of level $|2\rangle$ is taken to infinity. We find that the second

harmonic signal survives in this limit (see Fig. 4.3c), due to the additional coupling of the incident field to the transition $|1\rangle \leftrightarrow |3\rangle$. This limit is interesting, since it collapses the system onto an effective two-level system. As will be discussed further below, this implies that in the non-perturbative limit SHG in a two-level system is possible.

An interesting question is now how a parity invariant Hamiltonian can sustain electronic states of indefinite electronic parity? The answer is simply that for coupled light-matter systems, the relevant quantity is the parity of the total system, not the parity considered in the electronic and photonic subsystems separately. As we will see below, this leads to SHG for intermediate electron-photon coupling even when the Hamiltonian of the system conserves parity.

4.2.1 Parity in coupled electron-photon systems

We now discuss second harmonic generation in a two-level system, and its relation to parity conservation in the intermediate coupling regime. For this purpose it is most transparent to work with a quantum description of the external radiation, and we therefore consider a two-level system coupled to quantum photons as appropriate for an atom interacting with the field of a cavity. We neglect terms quadratic in the photonic vector potential A, that should be important only for very strong couplings. The same Hamiltonian was discussed by Cini, D'Andrea and Verdozzi [66, 67] and is given by

$$\begin{aligned} H = {} & \epsilon_1 c_1^\dagger c_1 + \epsilon_2 c_2^\dagger c_2 + \omega_0 a^\dagger a + \omega b^\dagger b \\ & + g(t)(c_1^\dagger c_2 + c_2^\dagger c_1)(a^\dagger + a) + g'(t)(c_1^\dagger c_2 + c_2^\dagger c_1)(b^\dagger + b), \end{aligned} \tag{4.10}$$

were c_i destroys an electron in level $|i\rangle$ with energy ϵ_i. The operator a annihilates a photon of an incident field with frequency ω_0, and similarly b annihilates a photon of a fluorescent field with frequency ω. The interaction of the electron with the incident and fluorescent fields are respectively given by the couplings $g(t)$ and $g'(t)$, that can in principle have any time-dependence. In order for g and g' to be non-zero, the levels $|1\rangle$ and $|2\rangle$ need to be of different parity. We also define a parity operator by

$$\Pi = (n_1 - n_2) e^{i\pi n_a} e^{i\pi n_b}, \tag{4.11}$$

where n_i ($n_{a/b}$) are density operators in the electron (photon) space, and Π acts in the coupled electron-photon space. Since Π commutes with the Hamiltonian, the eigenstates of H will be of definite parity. To simplify the discussion we temporarily set $g(t) = g\theta(t)$ and $g'(t) = 0$.

We now consider the parity of the eigenstates of H. If we assume that the incident field is close to resonance with the atomic transition, so that $\omega_0 \approx \epsilon_2 - \epsilon_1$, we can use the rotating wave approximation (RWA) [49]. This corresponds to assuming that the energy

conserving transitions $|1, n_a\rangle \leftrightarrow |2, n_a - 1\rangle$, where $|n_a\rangle$ is a number state of the incident field, dominate over the virtual transitions $|1, n_a\rangle \leftrightarrow |2, n_a + 1\rangle$. In the RWA only the nearly degenerate states $|1, n_a\rangle$ and $|2, n_a - 1\rangle$ are mixed by the light-matter interaction, and we can diagonalize H to find the dressed eigenstates [49]

$$|+, n\rangle = \cos\theta|1, n_a\rangle + \sin\theta|2, n_a - 1\rangle \tag{4.12a}$$

$$|-, n\rangle = -\sin\theta|1, n_a\rangle + \cos\theta|2, n_a - 1\rangle. \tag{4.12b}$$

Here the coefficients are determined by the mixing angle $\tan 2\theta = g\sqrt{n_a}/\delta$, where $\delta = \omega_0 - (\epsilon_2 - \epsilon_1)$ is the detuning. We note that when the detuning is zero, even a very small coupling gives complete mixing of the states (since $\theta = \pi/4$). By applying the parity operator Π defined above, we see that the eigenstates $|\pm, n_a\rangle$ are even (odd) with respect to parity when n_a is even (odd).

If instead we assume that $\omega_0 \approx (\epsilon_2 - \epsilon_1)/2$, two photons are necessary to excite an electron from level $|1\rangle$ to level $|2\rangle$. In this case we cannot apply the RWA, since the transitions $|1, n_a\rangle \leftrightarrow |2, n_a + 1\rangle$ are of the same importance as the transitions $|1, n_a\rangle \leftrightarrow |2, n_a - 1\rangle$. Therefore, an exact analytical solution for the eigenstates is no longer available. However, since the parity operator commutes with the Hamiltonian, the eigenstates can be written on the general form [68]

$$|\Psi_e\rangle = \sum_{n_a} c_{2n_a}|1, 2n_a\rangle + \sum_{n_a} c_{2n_a+1}|2, 2n_a + 1\rangle \tag{4.13a}$$

$$|\Psi_o\rangle = \sum_{n_a} c_{2n_a+1}|1, 2n_a + 1\rangle + \sum_{n_a} c_{2n_a}|2, 2n_a\rangle, \tag{4.13b}$$

where the subscript e (o) denotes a state with even (odd) parity. We note that although these states have a definite parity in the full Hilbert space of the coupled electron-photon system, if projected onto the electronic or photonic subsystems their parity is no longer well defined. In fact, computing the reduced density matrix of the electronic system for either of the above states gives the general structure $\rho_{el} = \alpha|1\rangle\langle 1| + \beta|2\rangle\langle 2|$, showing that the system is in a statistical mixture of the two electronic states.

Now that we know the structure of the eigenstates, we consider the evolution of the system from a given initial state. First consider a system prepared with an electron in the ground state $|1\rangle$ and the incident radiation in a coherent state $|\beta\rangle$. The initial state of the coupled system is then

$$|\Psi\rangle = |1, \beta\rangle = |1\rangle \otimes e^{-|\beta|^2/2} \sum_{n_a} \frac{\beta^{n_a}}{\sqrt{n_a!}}|n_a\rangle, \tag{4.14}$$

which is of indefinite parity with respect to Π. This state will therefore in principle have a non-zero overlap with all eigenstates of H, and the time-evolution will mix these states so

that an electron may be excited from state $|1\rangle$ to $|2\rangle$. In this case, the possibility of second harmonic generation is due to explicit parity breaking by the initial state. However, even if we consider the field to be initially in a number state, so that $|\Psi\rangle = |1, n_a\rangle$, it is possible to excite the electronic system. In this case the evolution will be restricted to the subspace of equal parity as the initial state, but since the initial state is not an eigenstate of H the evolution will induce transitions between the electronic states. In this case, the total parity $\Pi = \pi_{el}\pi_{ph}$ is conserved, but the electronic and photonic parities π_{el} and π_{ph} can change.

Finally we consider the semi-classical limit of light-matter interactions, obtained by starting from the density matrix $\rho = |\psi_{el}, \beta\rangle\langle\psi_{el}, \beta|$ and tracing out the photonic degrees of freedom. In particular, we try to identify the Hamiltonian that satisfies the Liouville-von Neumann equation

$$i\frac{\partial}{\partial t}\rho_{el}(t) = [H_{el}, \rho_{el}(t)] = \mathrm{Tr}[H, \rho(t)] \tag{4.15}$$

for the electronic density matrix $\rho_{el} = |\psi_{el}\rangle\langle\psi_{el}|$. Using the definition of the coherent states as eigenstates of the annihilation operator, $a|\beta(t)\rangle = \beta e^{-i\omega t}|\beta(t)\rangle$, we find

$$\begin{aligned}\mathrm{Tr}[H, \rho(t)] &= \frac{1}{\pi}\int d(\mathrm{Re}\alpha)d(\mathrm{Im}\alpha)\langle\alpha|H\rho(t) - \rho(t)H|\alpha\rangle \\ &= \frac{1}{\pi}\int d(\mathrm{Re}\alpha)d(\mathrm{Im}\alpha)[H(\alpha^*, \beta)\rho_{el}(t) - \rho_{el}(t)H(\beta^*, \alpha)]e^{-|\alpha-\beta|^2},\end{aligned} \tag{4.16}$$

where the Hamiltonian depends parametrically on the values of the coherent fields. In this formula we have used that the coherent states are non-orthogonal, and instead satisfy the relation $|\langle\alpha|\beta\rangle|^2 = e^{-|\alpha-\beta|^2}$. Since this function decays rapidly for $\alpha \neq \beta$, we can in the limit of large β assume $\alpha = \beta$ in the Hamiltonian. Performing the integral over α for the exponential function then gives a contribution π, and the semi-classical Hamiltonian is given by

$$H_{el} = \epsilon_1 c_1^\dagger c_1 + \epsilon_2 c_2^\dagger c_2 + \omega|\beta|^2 + g(c_1^\dagger c_2 + c_2^\dagger c_1)(\beta^* e^{i\omega_0 t} + \beta e^{-i\omega_0 t}). \tag{4.17}$$

Since the semi-classical equations are derived from an initial electron-photon state of indefinite parity, it is not surprising that they can give rise to non-conserving parity processes in the electronic subspace.

4.2.2 Mollow and second harmonic spectra in two-level systems

We now return to the Hamiltonian of Eq. 4.10 and consider the fluorescence spectrum obtained by varying the frequency ω. These results are presented in Paper VI. We define the fluorescence spectrum as [66, 67]

$$\mathcal{P}_n(t, \omega) = \sum_{mi} |\langle i, m, n|\mathcal{T}\left[e^{-i\int_0^t H(t')dt'}\right]|1, \beta, 0\rangle|^2, \tag{4.18}$$

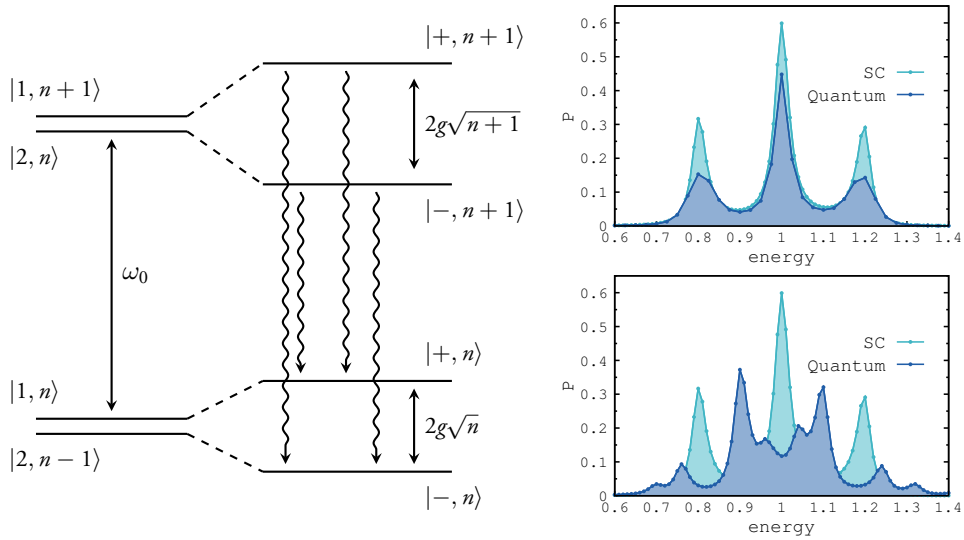

Figure 4.4: Energy spectrum for a two-level atom coupled to an incident field on resonance with the atomic transition (left). The original degenerate energy levels are split by the light-matter interaction. Also indicated are the fluorescent transitions giving rise to the Mollow triplet. To the right are fluorescence spectra for a coherent field with $\beta = 5$ and $g = 0.02$ (top), and with $\beta = 1$ and $g = 0.1$ (bottom). In both cases light blue denotes the semi-classical result, dark blue the quantum result, and $g' = 0.01$. The diagram is adapted from [69] and the figures from Paper VI. The results for the Mollow spectrum also appear in [66, 67].

where i denotes the electronic state, m the number of photons in the incident field and n the photon number in the fluorescent field. The initial state is taken with the electron in its ground state, the incident field in the coherent state $|\beta\rangle$, and zero photons in the fluorescent field. In the following we consider the case $g'(t) = g'e^{-\Gamma t}$, which introduces a phenomenological damping of rate Γ, and take $g(t) = g\theta(t)$.

We first consider the fluorescence spectrum for a coherent field of frequency $\omega_0 = \epsilon_2 - \epsilon_1$. The energies of the dressed states are given in the RWA by $\epsilon_{\pm,n} = n\omega_0 \pm g\sqrt{n}$, as indicated schematically in Fig. 4.4. When the system is probed by a fluorescent field the single spectral line for $g = 0$ is transformed into a so-called Mollow triplet for $g \neq 0$. The name comes from the spectral shape in the limit of large β, where we can make the assumption $\sqrt{n} \approx \beta$ and the energy splittings $\epsilon_{+,n} - \epsilon_{-,n} = 2g\beta$ become independent of n. In this limit there are therefore three possible transition energies between states with consecutive n, and the spectrum shows a three-peaked structure. The fluorescence spectrum for large β is shown in Fig. 4.4 (upper right panel) for both a quantum and semi-classical treatment of the incident field, which are seen to be in good agreement. For an incident field with small β the level splittings are no longer independent of n, and there are four possible transition energies between states with consecutive n. Therefore we expect to see at least four peaks in the fluorescence spectrum, which is indeed the case, as indicated in Fig. 4.4 (lower right panel). In fact, we observe an even more intricate structure, coming from the fact that also

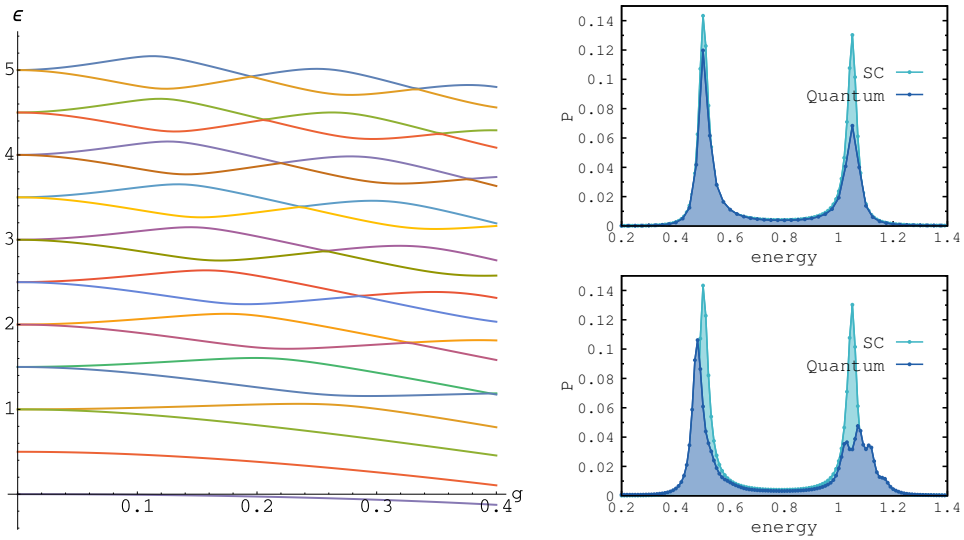

Figure 4.5: Energy spectrum for a two-level atom coupled to an incident field of frequency $\omega_0 = (\epsilon_2 - \epsilon_1)/2$ (left), for different values of the coupling g. To the right are fluorescence spectra for a coherent field with $\beta = 5$ and $g = 0.02$ (top), and with $\beta = 1$ and $g = 0.1$ (bottom). In both cases light blue denotes the semi-classical result, dark blue the quantum result, and $g' = 0.01$. The SHG spectra are adapted from Paper VI and also appear in [66, 67].

transitions with different n contribute to the spectrum. Since the semi-classical results only depend on the product $g\beta$, which is kept constant in the two calculations, it gives the same result as for large β and is not able to reproduce the spectrum in the low-photon regime.

We now consider the fluorescence spectrum for an incident field with the frequency $\omega_0 = (\epsilon_2 - \epsilon_1)/2$. For a coherent field with large β and small g the spectrum shows two peaks, which are nicely reproduced by a semi-classical calculation (see Fig. 4.5). The first peak is due to elastic Rayleigh scattering, where the energy absorbed from the incident field is emitted into the fluorescent field with the same frequency $\omega = \omega_0$. The second peak constitutes the second harmonic generation. For an incident field with small β and large g, the elastic peak is still well described by the semi-classical results. However, for the second harmonic peak the quantum calculation shows a superimposed Mollow structure that is not captured by the semi-classical calculation. This feature can be understood by considering the energy level spectrum for different coupling strengths g (see Fig. 4.5). For $g = 0.02$ the splitting of degenerate levels due to light-matter coupling is very small, so that effectively the SHG spectrum contains a single peak. For $g = 0.1$ the splitting is large enough to be visible in the fluorescence signal.

Chapter 5

Ultrafast spectroscopy

With the advent of laser technologies able to create pulses of femto- and attosecond duration, it is now possible to study and manipulate atomic and solid-state systems on their natural time-scale, and so investigate interacting systems far from equilibrium. However, since pulsed light-fields break the time-translational invariance of the system, it is necessary to use an explicitly time-dependent formulation of the problem. Together with the highly non-adiabatic character of ultrafast processes, this makes a theoretical description challenging. In this chapter we look at three different ultrafast processes: We start by considering adsorbate dynamics (Sec. 5.1), for which a crucial ingredient is the interplay of electronic and nuclear degrees of freedom. In particular, we look at the process of atomic desorption, and discuss how ultrashort laser pulses can be used to study and control this process in time. In the next section we look at the Auger process (Sec. 5.2), and show how the lifetime of the Auger decay can be increased by inducing the quantum Zeno effect. Finally, we discuss the role of electron-electron interactions for charge-separation in a prototypical donor-acceptor system (Sec. 5.3), a process of fundamental importance to solar harvesting materials.

5.1 Desorption dynamics

A process of great physical and technological importance is that of atomic adsorption, in which an atom sticks to the surface of a substrate by forming a bond. Depending on the strength of the bond it is common to distinguish between two types of adsorption, namely physisorption (for weaker bonds) and chemisorption (for stronger bonds) [70]. Of equal interest is the process of atomic desorption, in which an adsorbed atom breaks free from the substrate. How and when an atom is prone to adsorb or desorb is interesting from a

technological stand-point, for example in the catalysis of many chemical reactions. From a theoretical perspective, adsorbate dynamics is of interest since it involves an interaction of electronic and nuclear degrees of freedom beyond the harmonic regime. In this section we discuss how external light-fields can be used to initiate and control the desorption of an initially adsorbed atom.

A description of atomic desorption is in principle within reach of DFT and NEGF, but in practice these methods involve a number of approximations. The first is with regard to the electron-electron interaction, which in DFT is treated by an approximate exchange-correlation potential, and in NEGF by a perturbative expansion of the self-energy (see Secs. 2.3 and 3.1). The second approximation is with regard to the electron-nuclear interaction, that is usually treated within the semi-classical Ehrenfest approximation (see Sec. 2.4). Even though there are extensions beyond this approach, such as surface hopping and trajectory algorithms for wavefunction based methods [71, 72, 73, 74], and the inclusion of quantum vibrations in the framework of NEGF [75, 76], a non-pertubative treatment of general electron-nuclear interactions is still out of reach for first-principle descriptions of matter. Since desorption involves nuclear dynamics in the highly anharmonic regime, we therefore address the desorption process from a model perspective. This allows us to use a full quantum description of the electron-nuclear interaction, but limits the size of the system to a rather small substrate. To address finite size effects, we compare the results of an exact treatment to a description in terms of NEGF together with Ehrenfest dynamics. This later approach, although approximate with regard to the interactions, has the advantage that it makes a treatment of macroscopic systems possible.

Since the physics of adsorbate-substrate systems is quite complex, we start by trying to provide an intuitive understanding of the adsorption process through a simple model. More specifically, we consider the Anderson model [77] described by the Hamiltonian

$$H = \epsilon_0 n_0 + U n_{0\uparrow} n_{0\downarrow} + \sum_k \epsilon_k n_k + \sum_k t_k (c_0^\dagger c_k + h.c.), \tag{5.1}$$

which was originally introduced to describe the effects of localized magnetic impurities in narrow band materials. It was later realized by Newns [78] and Grimley [79] that the same model can be used to study the behavior of an atom adsorbed on a metallic surface. In this context, the state $|0\rangle$ represents an adsorbate atom with a local interaction U, coupled to a substrate of electrons with energies ϵ_k via the matrix elements t_k. By solving for the adsorbate Green's function $G_{0\sigma}(\omega)$ in the Hartree-Fock approximation [78], we can distinguish between two regimes of adsorption depending on the strength of the adsorbate-substrate coupling. In the weak coupling limit we find a single localized orbital at approximately the unperturbed Hartree-Fock energy $\epsilon_{0\sigma} = \epsilon_0 + U\langle n_{0\bar{\sigma}}\rangle$, which largely resembles the atomic state $|0\rangle$. In the strong coupling limit we find two localized states with energies at opposite edges of the substrate band, whose overlap with the atomic state is close to $1/2$. Thus in the weak coupling case the adsorbate level closely resembles that of the isolated atom,

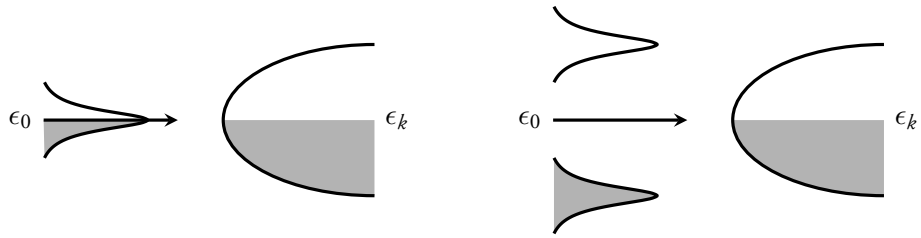

Figure 5.1: Illustration of the energy levels of an adsorbate-substrate system in the weak coupling limit (left) and the strong coupling limit (right). The arrow indicates the bare atomic level of energy ϵ_0, while the broadened spectral lines show the energy of the states localized on the atom in presence of a substrate.

while in the strong coupling limit the atomic level is split into two states resembling the bonding and anti-bonding levels of a surface molecule, formed by the adsorbate and the substrate atoms to which it is directly coupled. The weak and strong coupling limits are schematically shown in Fig. 5.1.

In a dynamical description of adsorbate-substrate systems, we also need to consider the effects of charge fluctuations on the adsorbate atom. Due to the presence of the surface, any local charge fluctuations will be screened by an image charge consisting of the excitation of plasmons and electron-hole pairs. A model to understand plasmon screening of core holes was proposed by Lundqvist [80] based on the Hamiltonian

$$H = \epsilon n_c + \sum_q \omega_q b_q^\dagger b_q + \sum_q (1 - n_c) g_q (b_q^\dagger + b_q), \tag{5.2}$$

where n_c is the density operator for the core state, ω_q is the energy of a plasmon with wave vector q, and g_q is the electron-plasmon coupling. An exact solution for the core level spectral function A of this model was provided by Langreth [81]. Restricting to the lesser part of A and assuming for simplicity that $\omega_q = \omega_p$ for all q, the spectral function can be written

$$A(\omega) = \sum_m \frac{e^{-a} a^m}{m!} \delta(\omega - \epsilon - a\omega_p + m\omega_p), \tag{5.3}$$

where $a = \sum_q (g_q/\omega_p)^2$. The main effect of plasmon screening is therefore the appearance of satellite structures in the spectral function, corresponding to ionization of the core hole with the simultaneous creation of m plasmons. Since these peaks are suppressed by the factor $(g/\omega)^{2m}$, only the lowest plasmon states will be important in the weak coupling regime.

We now formulate a model for dynamical studies of desorption (used in Paper I), aimed at including as many features as possible of a realistic adsorbate-substrate system while still retaining enough simplicity to allow for an exact numerical solution. It contains as limiting cases the Anderson-Newns-Grimley model and the plasmon screening model of Lundqvist,

but also includes a mobile adsorbate along the lines of the charge-transfer model of Shin and Metiu [82]. The total Hamiltonian is given by $H(t) = H_s + H_a + H_{as} + H_{ext}(t)$, and the model is schematically illustrated in Fig. 5.2. Here

$$H_s = -t \sum_{\langle ij \rangle \sigma} c^\dagger_{i\sigma} c_{j\sigma} + \omega_p b^\dagger b \tag{5.4}$$

describes a substrate with nearest neighbor hopping t, and an effective plasmon mode of frequency ω_p. We can think of the tight-binding term as describing a narrow electronic band (of *d*- or *f*-type), while the plasmon arises from a more extended band (of *s*- or *p*-type). The adsorbate is governed by the Hamiltonian

$$H_a = \frac{p^2}{2M} + \epsilon_c n_c + \sum_{v\sigma} \epsilon_v n_{v\sigma} + \sum_{vv'\sigma\sigma'} U_{vv'} n_{v\sigma} n_{v'\sigma'} - w(1 - n_c) N_a \tag{5.5}$$

where p denotes the momentum of the adsorbate nucleus with mass M. The adsorbate has a deep core level of energy ϵ_c, and a number of valence levels with energies ϵ_v interacting via $U_{vv'}$. In the event of core ionization the valence levels are shifted down an energy w, and $N_a = \sum_v n_v$. The coupling between adsorbate and substrate is given by

$$H_{as} = \frac{\kappa}{x^4} - g e^{-\lambda(x-1)} \sum_{v\sigma} \left(a^\dagger_{v\sigma} c_{S\sigma} + h.c. \right) + \gamma \left(N_a - \langle N_a \rangle_0 \right) \left(b^\dagger + b \right), \tag{5.6}$$

where κ is the strength of the nuclear-nuclear repulsion, and the parameters g and λ determine the strength and decay length of an attractive adsorbate-substrate interaction. The index S denotes the first atom of the substrate, to which the adsorbate is connected. The last term describes the coupling between plasmons and charge fluctuations on the adsorbate with strength γ. To perturb the system we use an external field whose coupling to the adsorbate levels is described by $H_{ext}(t) = \sum_{v \neq v'\sigma} \Lambda_{vv'}(t) a^\dagger_{v\sigma} a_{v'\sigma}$, where $\Lambda(t)$ determines the strength and shape of the laser pulse. We used this model in Paper I to investigate desorption dynamics in a finite system, and a simplified version in Paper II to study effects of approximations and finite size. The main results of these papers are discussed in the following sections.

5.1.1 Exact electron-nuclear dynamics

In Paper I we solved the model above using exact diagonalization, as discussed in Section 2.1, in the basis $|n_{i_1\sigma}, n_{i_2\sigma}, \ldots, n_{i_7\sigma}\rangle \otimes |n_k\rangle \otimes |x_n\rangle$ consisting of $L = 7$ electronic orbitals, one plasmon mode k, and a set of grid points x_n describing the distance of the adsorbate from the substrate surface. Out of the electronic orbitals, two describe valence levels on the adsorbate, and the remaining five the substrate (see Fig. 5.2). Since the adsorbate core level

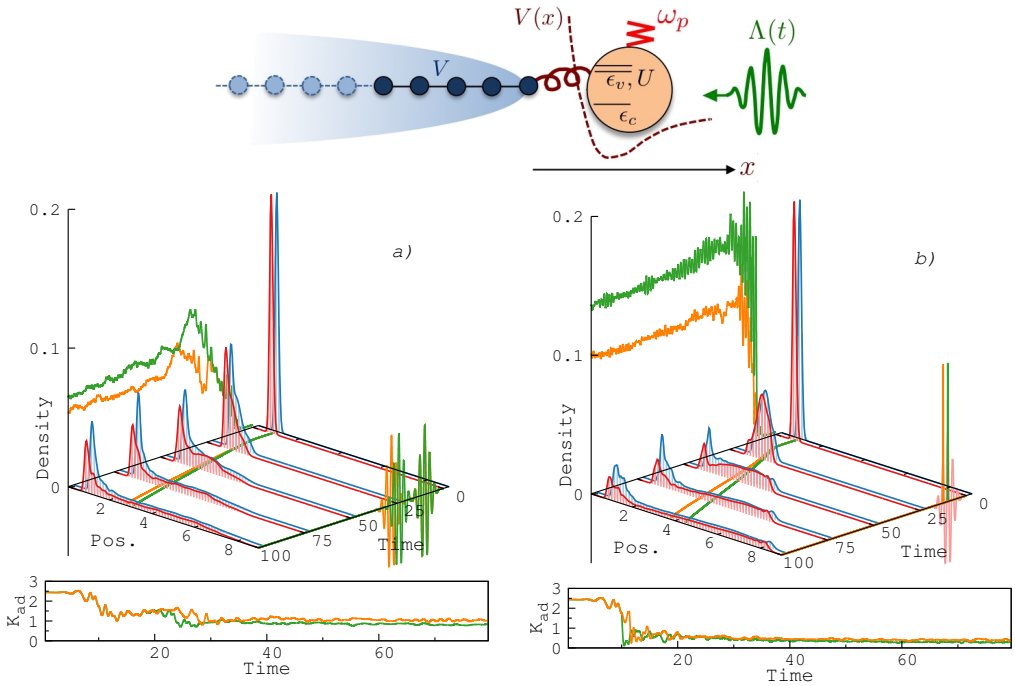

Figure 5.2: The top panel gives a schematic illustration of the desorption model considered in Paper I. Panel (a) shows the time-evolution of the nuclear wavepacket using two different pulse protocols. By varying the delay between the two pulses we can control the response of the plasmon and increase or decrease the associated desorption yield. In panel (b) we show the effect of core ionization during the time evolution. The figures are adapted from Paper I.

has no dynamics, we don't include it explicitly in the description, but treat core ionization as an instantaneous event where $n_c = 1$ is changed to $n_c = 0$. We consider a total of six electrons with $N_\uparrow = N_\downarrow = 3$, and pick the energies ϵ_{v1} and ϵ_{v2} so that in the ground state the level $|v_1\rangle$ is filled, $|v_2\rangle$ is empty and the substrate half-filled.

To quantify the desorption probability resulting from an external field of given shape and intensity, we consider the desorption yield Y defined by $Y(t) = 1 - \int_0^{x_0} P_t(x)dx$. Here $P_t(x)$ is the nuclear probability distribution at time t, and x_0 is chosen as the smallest value for which $Y(0) = 0$. In this way Y measures the fraction of the wavepacket that has left the region where it is initially bound. In particular, we were interested in seeing if it is possible to control the desorption yield by using specific pulse protocols. We therefore considered an external field consisting of two 6 fs pulses with a carrier frequency of 800 nm and a delay τ between their respective peak intensities. As seen in Fig. 5.2a, only a slight shift in the delay time can significantly alter the desorption behavior and give an increased yield on the order of 15%. In both cases we see that part of the nuclear wavepacket is emitted while another part stays bound, an effect that is not possible to describe with a semi-classical method such as the Ehrenfest approximation. We also considered a similar protocol, consisting of a single 800 nm pulse and a much shorter XUV pulse leading to instantaneous ionization

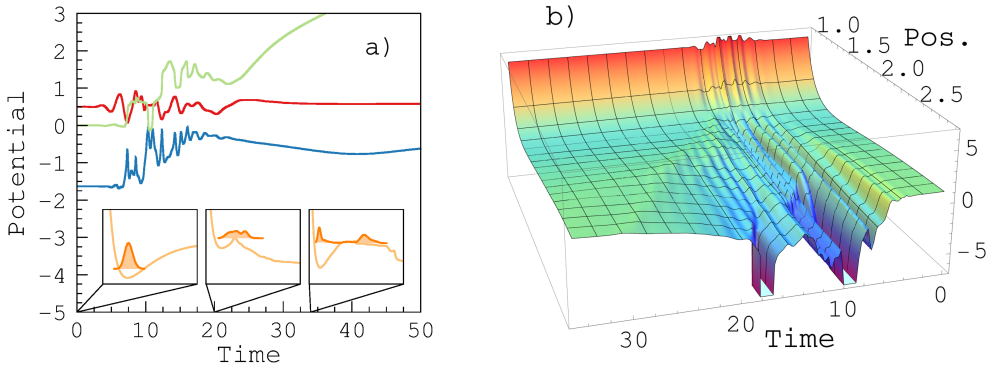

Figure 5.3: Exact electronic and nuclear Kohn-Sham potentials for a dimer system during desorption. Panel (a) shows in red the electron density on the interacting site, with the green curve denoting $\arg(T_{KS})$ and the blue curve $|T_{KS}|$. The snapshot at the bottom shows the nuclear density and nuclear potential at different times. Panel (b) shows the nuclear potential V_{KS} in time. The figures are adapted from Paper I.

of the core level. By similarly varying the delay between the IR and XUV pulses we see significant differences in desorption behavior and in the corresponding desorption yield (Fig. 5.2b). How can these results be understood? Since the nuclear dynamics happen on a long time-scale compared to the shifts in pulse delay, the observed effects must be due to electronic and plasmonic degrees of freedom. In fact, our results indicate that what happens is that the first pulse excites coherent oscillations in the plasmon response, which the second pulse can either enhance or suppress by being in phase or anti-phase with the oscillations. Enhancing the plasmon oscillations in turn leads to a suppression of the bond kinetic energy K_{ad} between the adsorbate and substrate (see Fig. 5.2), giving a larger desorption yield. It is therefore possible to control the desorption yield on very short time-scales by manipulating the plasmonic response.

Another important result of Paper I is the construction of exact electronic and nuclear Kohn-Sham potentials for the multi-component TDDFT framework discussed in detail in Section 2.3. For simplicity we neglect plasmons and consider a two-site system, obtained from the general Hamiltonian by retaining a single level on the adsorbate and in the substrate. The Kohn-Sham system is described by the coupled set of equations

$$H_e^{KS} = \sum_{ij,\sigma} \left(T_{ij}^{KS}[Q_{ij}, \Gamma](t) c_{i,\sigma}^\dagger c_{j,\sigma} + h.c. \right) \tag{5.7a}$$

$$H_n^{KS} = \sum_k \frac{p^2}{2M} + V_{KS}[Q_{ij}, \Gamma](x,t), \tag{5.7b}$$

where the fundamental variables are the diagonal of the nuclear density matrix $\Gamma(x,t)$ and the complex electronic bond current $Q_{ij}(t)$ (for details see Section 2.3). Since the system we consider has a position dependent hopping between adsorbate and substrate, which

for large x tends to zero, the electronic Kohn-Sham potential needs to be complex and have both a phase and modulus that can vary. To extract the exact potential V_{KS} we use the factorization of the electron-nuclear wavefunction introduced by Abedi, Maitra and Gross [29]. Defining the nuclear wavefunction $\chi(x,t) = e^{-iS(x,t)}\xi(x,t)$, the exact nuclear potential is $V = (2M)^{-1}[(\partial_x \ln \xi)^2 + \partial_{xx} \ln \xi - (\partial_x S)^2] - \partial_t S$ in the gauge where the vector potential is zero. Since the potential describes a non-interacting nucleus, it is by definition also equal to the exact Kohn-Sham nuclear potential V_{KS}. The electronic potential is obtained through numerical reverse-engineering, corresponding to a numerical fitting of the Kohn-Sham density to the exact density in time. In Fig. 5.3 we show the Kohn-Sham potentials for a case of substantial desorption, where the nuclear wavepacket almost completely leaves the bound region of the potential. As the external field acts on the system we see how the nuclear potential is lowered to release part of the wavepacket, and then increases to contain the part that stays bound. We also note that just before the wavepacket splits, the whole nuclear density has been shifted to larger adsorbate-substrate distances, leading to a significant reduction in the modulus of the electronic potential.

5.1.2 Desorption in macroscopic systems

The most severe approximation for the system considered above is the truncation of the substrate to a finite (in fact rather short) linear chain. This approximation is necessary to solve the model using exact diagonalization, since the size of the many-body basis scales exponentially with the system size. To address the effects of a finite system and to treat macroscopic systems, we in Paper II used the NEGF method to describe a similar system, with the nuclear coordinate treated classically using the Ehrenfest approximation. By comparing results from exact diagonalization and NEGF, we could also address the effects of an approximate treatment of electron-electron and electron-nuclear interactions. Starting from a full quantum treatment of the finite system, we therefore introduced first the Ehrenfest approximation and then a perturbative treatment of electronic interactions, and in a last step extended the linear chain to a macroscopic substrate using an embedding self-energy. We note that to include classical nuclear coordinates $\mathbf{R}$ in a NEGF description is very similar to the approach discussed in Sec. 2.4 for wavefunction methods. Since the nuclear coordinates enter parametrically into the single-particle Hamiltonian, this amounts to solving the Kadanoff-Baym equation with a Hamiltonian $h = h(\mathbf{R})$, together with the semi-classical equation

$$M\ddot{\mathbf{R}}(t) = -\frac{\partial}{\partial \mathbf{R}}\langle \Psi | h(1,\mathbf{R}) | \Psi \rangle = i\frac{\partial}{\partial \mathbf{R}} \int d\mathbf{x} h(1,\mathbf{R}) G^<(1,1). \tag{5.8}$$

In Fig. 5.4 we show results obtained with the different levels of approximation discussed above. For early times, during which the external field is active, both the electron and

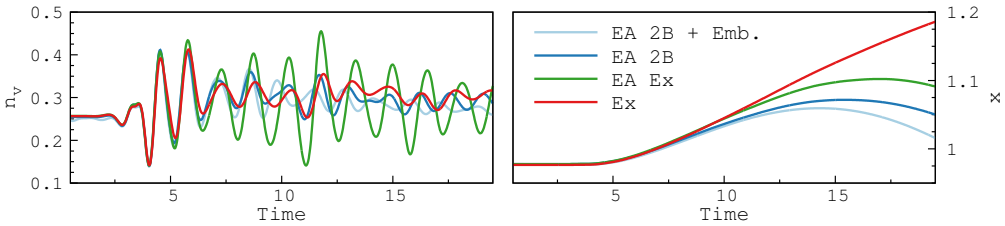

Figure 5.4: Comparison of desorption dynamics in a finite system using exact diagonalization (red), exact electron dynamics with the Ehrenfest approximation (green), and non-equilibrium Green's functions with the second-Born approximation together with the Ehrenfest approximation (blue). The light blue line shows the result for a macroscopic system using NEGF with an embedding self-energy. The figures are adapted from Paper II.

nuclear dynamics are well described in all approximations. At later times however, the electron density of the exact solution is better reproduced by the NEGF results than the exact electronic dynamics together with the Ehrenfest approximation. This is however an artifact of a known problem with NEGF for finite systems [83], namely the appearance of artificial damping due to a sampling of diagrams outside the finite Hilbert space. For the nuclear dynamics the results from using exact electronic dynamics are in better agreement with the exact solution than the results of NEGF. We see that the introduction of a macroscopic substrate has little effect on the electronic dynamics, while it reduces the stretching of the nuclear coordinate. This is most likely due to the additional dissipation channel introduced by the substrate, leading to a smaller energy transfer between the electrons and nuclei. However, the effect of using the Ehrenfest approximation seems to be more severe than the neglect of the infinite substrate, indicating that a good qualitative description of desorption can be expected even in a finite system. As a final caveat, this conclusion is probably dependent on the parameters, but should apply in the strong coupling (surface molecule) limit considered here.

5.2 Auger spectroscopy

In this section we discuss the Auger decay of an atom following photo-ionization of a deep core level. This process, originally discovered by Meitner and later independently by Auger, consists in a valence electron filling the core level with the simultaneous emission of a secondary valence electron. Like in radiative decay, where the atom relaxes through the emission of a photon with energy $\omega = \epsilon_c - \epsilon_v$ corresponding to the difference in binding energy of the core and valence states, the Auger process gives information about the atoms electronic structure. In Auger decay an electron is emitted with the energy $\epsilon_a = \epsilon_c - \epsilon_{v_1 v_2}$, corresponding to the difference in binding energies of the core and the two participating valence levels. This is used in Auger electron spectroscopy to characterize the chemical composition and electronic structure of atomic gases and solids [84].

The theory of Auger decay has been extensively studied both for isolated atoms and systems in the solid state. In atomic systems the Auger spectrum is typically composed of a series of sharp peaks corresponding to a cascade of individual Auger processes [85], while in solid state spectra the lineshapes can have a more complicated form. This is due to the interaction of the holes on the Auger decaying atom with the surrounding electrons in the material [86, 87, 88]. Broadly speaking, the levels of theoretical description can be divided into one-step and two-step models. The former treats the whole Auger decay, including the initial photo-ionization and incomplete relaxation effects, on equal footing. In the latter, the core hole is assumed to be long-lived enough that the system relaxes to a new ground state in presence of the core hole, so that the ionization and decay processes can be treated separately. In the following we briefly discuss some examples of these models, taken from the solid state context.

Before going into details about the Auger process, we recall some general features of a decay process. We consider the Wigner-Weisskopf model of a single level $|0\rangle$ coupled to a continuum of states $|k\rangle$, as described by the Hamiltonian

$$H = \epsilon_0 n_0 + \sum_k \epsilon_k n_k + \sum_k t_k (c_0^\dagger c_k + h.c.). \tag{5.9}$$

Although this model is completely non-interacting, it gives an effective description of the Auger process in the limit where only the Auger interactions are retained. This is seen by identifying $|0\rangle = |v_1 v_2\rangle$ with the state of the decaying valence levels, $|k\rangle = |ck\rangle$ with the state with a filled core level and one electron in the continuum, and the matrix element $t_k = U_{ck21}$ with the Auger matrix element. The model can be solved exactly in frequency space and gives the amplitude $c_0(\omega) = i/[\omega - \epsilon_0 - \Sigma(\omega)]$ to find an electron emitted at energy ω, where the self-energy is $\Sigma(\omega) = \sum_k |t_k|^2/[\omega - \epsilon_k + i\eta]$. From this solution we can extract two key features: First, the coupling with the continuum introduces a shift in the peak of the probability to find an emitted particle from the bare energy ϵ_0 to the energy $\omega = \epsilon_0 + \mathrm{Re}\Sigma(\omega)$. Secondly, the lineshape of the level $|0\rangle$ is broadened into a Lorentzian of width $\Gamma(\omega) = \mathrm{Im}\Sigma(\omega)$. If for simplicity we assume the width to be independent of frequency, this gives rise to an exponential decay of the amplitude $c_0(t) \sim e^{-\Gamma t}$ in time.

Let us now move one step closer to a full description and consider Auger decay in the Anderson model [77] along the lines of Cini [86, 87]. Similar results were obtained by Sawatzky [88] but for a Hubbard model [89]. The Hamiltonian is given by

$$H = \epsilon_0 n_0 + U n_{0\uparrow} n_{0\downarrow} + \sum_k \epsilon_k n_k + \sum_k t_k (c_0^\dagger c_k + h.c.), \tag{5.10}$$

where U is a local interaction at the atom undergoing Auger decay and the continuum states describe a completely filled valence band of bandwidth W. We define the Auger current by

$$j_k = \frac{d}{dt} \langle \Phi(t) | n_k | \Phi(t) \rangle, \tag{5.11}$$

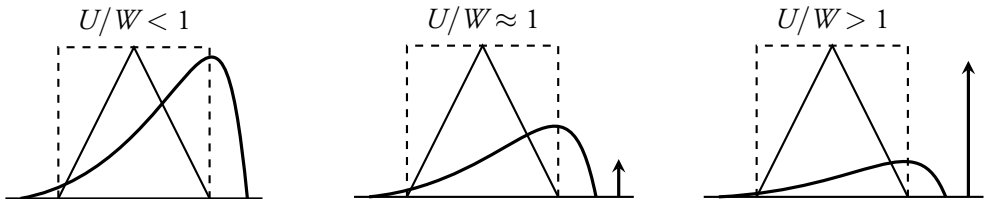

Figure 5.5: Evolution of the Auger lineshape as a function of increasing interaction. For low interactions U compared to the band width W, the lineshape is band-like but asymmetric. When the ratio $U/W > 1$ an atomic like peak appears in the spectrum, and for larger interactions more of the spectral weight is shifted into the atomic peak. The dashed line corresponds to a rough approximation of the one-particle density of states ρ, and the thin solid line to the self-convolution G_0. The results are adapted from [87].

and treat the system in the two-step approximation where $|\Phi(t)\rangle = U(t,-\infty)|\Phi\rangle$ and $|\Phi\rangle = c_c|\Psi\rangle$ is the ground state of the system in presence of a core hole. If the evolution operator U is expanded to lowest order in the Auger interaction, the current is given by

$$j_k = 2\pi\langle\Phi|A_k^\dagger\delta(\omega - H)A_k|\Phi\rangle, \tag{5.12}$$

where the operator $A_k = U_{kc00}c_{0\uparrow}c_{0\downarrow}$ includes the Auger matrix elements U_{kc00}. As can be seen, the current is proportional to the imaginary part of the two-hole Green's function $G(\omega) = \langle\Psi|(\omega - H)^{-1}|\Psi\rangle$, where $|\Psi\rangle = c_{0\uparrow}c_{0\downarrow}|\Phi\rangle$, which can be solved for exactly to find [90]

$$G(\omega) = \frac{G_0(\omega)}{1 - UG_0(\omega)}. \tag{5.13}$$

Here G_0 is the non-interacting two-particle Green's function and can be written as a convolution of the one-particle density of states with itself, $G_0(\omega) = \int d\omega'\rho(\omega - \omega')\rho(\omega')$. The Auger lineshape is now determined by the ratio U/W, as displayed in Fig. 5.5: For $U/W \ll 1$ the lineshape resembles the non-interaction density of states G_0, although slightly asymmetric. On the other hand, for $U/W \gg 1$ a pole appears in G that gives rise to a sharp atomic-like line. For intermediate values of U/W the spectrum will contain both atomic and bandlike features.

In a one-step model of Auger decay the initial ionization has to be explicitly taken into account. As discussed by Almbladh [91] and by Gunnarsson and Schönhammer [92], this can be achieved by treating the state $|\Phi(t)\rangle$ to first order in the external field, giving the current [92]

$$j_k = 2\pi V\sum_p |\tau_{cp}|^2\langle\Phi|\frac{1}{\omega - \epsilon_p - H(0) - i\Gamma}A_k^\dagger\delta(\omega - \epsilon_p - \epsilon_k - H(1))A_k \tag{5.14}$$
$$\times\frac{1}{\omega - \epsilon_p - H(0) + i\Gamma}|\Phi\rangle.$$

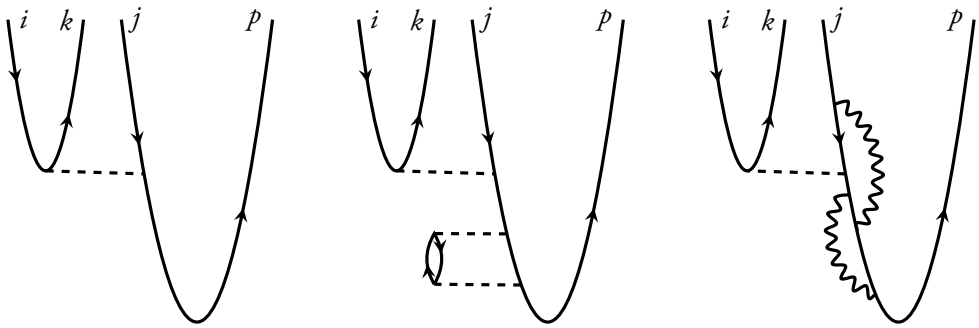

Figure 5.6: Examples of processes contributing to the Auger decay. The solid lines correspond to electrons (with arrows pointing up) and holes (with arrows pointing down), the dashed lines to the Auger interaction, and the wavy lines to excitations of the valence electrons. The left diagram shows the lowest order process, the middle diagram a process with virtual Auger transitions, and the right a process with virtual excitations that do not factorize according to a two-step description. The diagrams are adapted from [92].

In this expression V is the amplitude of the external field with frequency ω, τ_{cp} the dipole matrix elements between the core state and continuum states with energy ϵ_p, and ϵ_k is the energy of the Auger electron. The state $|\Phi\rangle = c_c|\Psi\rangle$ is a linear combination of $(N-1)$-particle eigenstates, and $H(n)$ is the valence electron Hamiltonian for core-hole occupancy n. The operator $A_k = \sum_{ij} U_{kcij} c_i c_j$ is together with the optical potential $\Gamma = \sum_{ijkl} \Gamma_{ijkl} c_i^\dagger c_j^\dagger c_l c_k$ responsible for virtual transitions during the decay, that give rise to effects from so-called incomplete relaxation. This includes spectral features such as satellite structures at higher energy (due to shake-down processes), and features due to screening of the core-hole by plasmon and electron-hole excitations. The formula for the Auger current in the one-step model can also be written in real-time as

$$j_k = 2\pi V \rho(\epsilon_p) |\tau|^2 \int_0^\infty dt dt' \langle \Phi | e^{i(H(0)+i\Gamma)t'} A_k^\dagger e^{i(\epsilon_k - H(1))(t'-t)} A_k e^{-i(H(0)-i\Gamma)t} | \Phi \rangle, \quad (5.15)$$

where ρ and τ are the average density of states and matrix elements at the energy of the photoelectron. For $\Gamma \to 0$ and with the assumption $e^{-H(0)t}|\Phi\rangle = \langle \Phi_0 | \Phi \rangle | \Phi_0 \rangle$ this formula reduces to the form of the Cini-Sawatzky model with a general valence band Hamiltonian $H = H(1)$. In Fig. 5.6 we show some processes contributing to the Auger decay. Due to virtual excitations screening the core-hole, the diagrams can in general not be separated into a photoionization and Auger decay part. Inclusion of such processes thus leads to the breakdown of the two-step approximation.

A benefit with formulating the problem in real-time is that propagation of the Schrödinger equation incorporates in a natural way all screening and relaxation effects of the Auger decay. Also, it is straightforward to include explicitly time-dependent terms in the Hamiltonian. However, due to the computational complexity associated with including the interaction terms responsible for Auger decay in the time-propagation, most studies are done in the frequency domain. In Paper v we studied the Auger decay of a four level atom in

presence of classical radiation, as described by the Hamiltonian

$$H = \sum_i \epsilon_i n_i + \sum_{ij} U_{ij} n_i n_j + \sum_k \epsilon_k n_k + \sum_q \epsilon_q n_q + f(t)\Omega \left(c_3^\dagger c_2 + h.c. \right) \tag{5.16}$$
$$+ \sum_k U_{kc12} \left(c_k^\dagger c_c^\dagger c_2 c_1 + h.c. \right) + \sum_q U_{qc13} \left(c_q^\dagger c_c^\dagger c_3 c_1 + h.c. \right).$$

The first two terms describe the atom with single-particle energies ϵ_i and interactions U_{ij} between the levels. We assume there are three levels $|c\rangle$, $|v_1\rangle$ and $|v_2\rangle$ of s-symmetry involved in the primary Auger decay, and a fourth level $|v_3\rangle$ of p-symmetry involved in an additional decay. The third and fourth terms of the Hamiltonian give the energies of the continuum into which an Auger electron is emitted, with the states $|k\rangle$ representing the s-channel and $|q\rangle$ the p-channel. The two Auger decays are mediated by the terms in the second line, that for simplicity we will denote by $M_k = U_{kc12}$ and $M_q = U_{kc13}$. The two highest valence levels $|2\rangle$ and $|3\rangle$ are coupled via a classical external field with Rabi frequency Ω, a frequency $\omega = \epsilon_3 - \epsilon_2$ and a time-dependence set by $f(t)$.

We study this system in a two-step approach starting from the initial hollow state $|1\rangle = |v_1 v_2\rangle$, which will decay into the states $|k\rangle = |ck\rangle$ with a lifetime τ_1. Similarly, if we would start from the state $|2\rangle = |v_1 v_3\rangle$ we would find a decay into the states $|cq\rangle$ with lifetime τ_2. We note that due to the form of the interactions, it is possible to reformulate the dynamics starting from state $|1\rangle$ in a one-particle language (cf. the discussion about the Wigner-Weisskopf model). The Hamiltonian now takes the form

$$H = \sum_i E_i n_i + \sum_k E_k n_k + \sum_q E_q n_q + f(t)\Omega \left(c_2^\dagger c_1 + h.c. \right) \tag{5.17}$$
$$+ \sum_k M_k \left(c_k^\dagger c_1 + h.c. \right) + \sum_q M_q \left(c_q^\dagger c_2 + h.c. \right),$$

where $E_1 = \epsilon_1 + \epsilon_2 + U_{12}$, $E_2 = \epsilon_1 + \epsilon_3 + U_{13}$ and $E_{k/q} = \epsilon_c + \epsilon_{k/q}$. Since the Hamiltonian only couples states within the two-particle subspace spanned by $|1\rangle$, $|2\rangle$, $|k\rangle$ and $|q\rangle$, we can expand the state vector like

$$|\Psi(t)\rangle = c_1(t) e^{-iE_1 t} |1\rangle + c_2(t) e^{-iE_2 t} |2\rangle + \sum_k c_k(t) e^{-iE_k t} |k\rangle + \sum_q c_q(t) e^{-iE_q t} |q\rangle. \tag{5.18}$$

This allows us to write a closed set of equations for the coefficients c_1 and c_2 on the form

$$(i\partial_t - E_1) c_1(t) = \sum_k \int dt' g_k(t - t') M_k c_1(t') + \Omega f(t) c_2(t) \tag{5.19a}$$

$$(i\partial_t - E_2) c_2(t) = \sum_q \int dt' g_q(t - t') M_q c_2(t') + \Omega f(t) c_1(t), \tag{5.19b}$$

where $g_{k/q}(t-t') = e^{-iE_{k/q}(t-t')}\theta(t-t')$ is the non-interacting Green's function of the continuum states. In Paper v we wanted to investigate how the presence of external driving affects the lifetime τ_1 of the primary Auger decay, and as discussed further in the next section, we found that the lifetime can be prolonged by inducing the quantum Zeno effect.

5.2.1 Quantum Zeno dynamics

The quantum Zeno effect (QZE) is the quantum mechanical analog of the arrow paradox put forward by the antique philosopher Zeno of Elea. As a disciple of the philosophic school of Parmenides, Zeno believed in a static and unchanging world, and meant by his paradoxes to disprove the concept of motion. The paradox of the arrow is that at any instant where it is observed, the arrow is at rest, and since at every instant it is at rest, there can be no motion. The quantum analog of this paradox was first put forward by Misra and Sudarshan [93], who argued that if a quantum system is measured upon frequently enough, its evolution will be inhibited. In a later analysis of Cook [94] an explicit proposal was put forward to measure the QZE in a slowly driven transition between the ground state and an excited state of an atom. By simultaneously driving a second transition that rapidly decays back to the ground state, and in the process emits a photon, a measurement can be performed by observing the outgoing photon. If the measurement cycle is short compared to the time it takes to drive the primary transition, this process should slow down in accordance with the QZE. The protocol of Cook was experimentally realized shortly after in the group of Wineland [95], using Be ions, and indeed a slowdown of the primary transition was observed. Since then the QZE has also been observed in the tunnel decay of ultracold atomic gases [96, 97], but so far not for any naturally occurring decay processes.

The way we expect the QZE to appear in our model of Auger decay is as follows. At the initial time $t = 0$, just after photoionization, we subject the system to a pulse of duration $t_\pi = \pi/\Omega$ (a so-called π-pulse). After this pulse the probability P_{v_3} of finding an electron in the upper valence state $|v_3\rangle$ is given by $P_{v_3}(t_\pi) = P_{v_2}(0)\Omega^2/(\Omega^2+\delta^2)$, where $\delta = \omega - (\epsilon_3 - \epsilon_2)$ is the detuning from resonance and $P_{v_2}(0)$ is the probability that the state $|v_2\rangle$ is initially occupied. At this point, a local projective measurement of the form $\Gamma = \gamma|v_3\rangle\langle v_3|$ can in principle be performed lasting for a time t_m. After the measurement, another π-pulse transfers the electron back to state $|v_2\rangle$ with probability $P_{v_2}(t_\pi + t_m + t_\pi) = P_{v_2}(0)\left[\Omega^2/(\Omega^2+\delta^2)\right]^2$. Since we consider the case of zero detuning, the final probability is $P_{v_2}(2t_\pi + t_m) = P_{v_2}(0)$, and the system returns to its original state.

If the system is subjected to a sequence of N measurements equally spaced in an interval $[0, T]$, this will induce a QZE. For small times the probability evolves quadratically with t, so at the beginning of the first measurement $P_{v_2}(\Delta t) \approx 1 - (\Delta t/\tau_z)^2$, where $1/\tau_z^2 = \langle H^2\rangle - \langle H\rangle^2$ defines the so-called Zeno time τ_z. Since the individual measurements preserve the probability P_{v_2}, the chance of remaining in the initial state at time T can be written

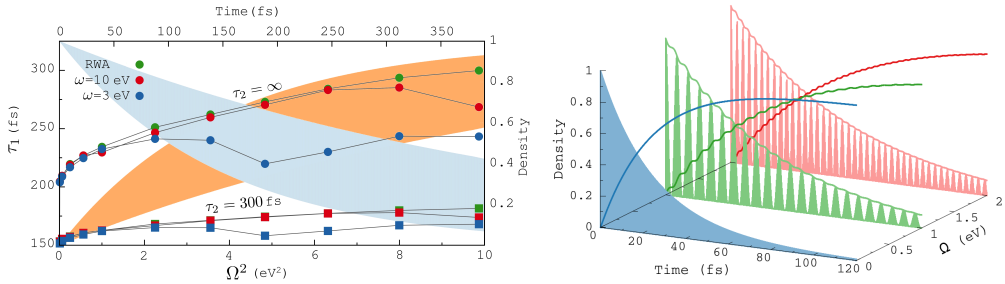

Figure 5.7: Parameter dependence of the quantum Zeno effect in an Auger decaying atom (left). The circles show the effective lifetime as a function of intensity I for a system with unperturbed lifetimes $\tau_1 = 100$ and $\tau_2 = \infty$, as obtained from the RWA (green) and the full field dynamics for $\omega = 10$ (red) and $\omega = 3$ (blue). The shaded areas show n_c (orange) and n_1 as function of time for $\tau_2 = \infty$ and within the RWA. The boundaries of these areas correspond to the decay with no field and with $\Omega = \sqrt{10}$ eV. The squares show the same results but with $\tau_2 = 300$. The figure to the right shows the dynamics of n_c, n_1 and n_2 as function of time for atomic Li. The blue curves are for $I = 0$, the green curves for $I = 5.1$ TW/cm^2 and the red curves for $I = 20.4$ TW/cm^2. The figures are adapted from Paper v.

$P_{v_2}(T) = P_{v_2}(\Delta t)^N$, which in the limit of infinitely many measurements becomes

$$P_{v_2}(T) \approx \lim_{N\to\infty} \left[1 - (T/N\tau_z)^2\right]^N = e^{-T^2/N\tau_z^2}. \tag{5.20}$$

For a large number of measurements the survival probability thus decays exponentially, and for $N \to \infty$ it tends to 1 giving a QZE.

In this argument we have implicitly assumed that the decay of the system can be neglected during the measurement, which is strictly true only in the limit of an infinite number of measurements and a stable upper valence level ($\tau_2 = \infty$). In the more general case, we will see a prolongation of the lifetime τ_1 that increases with the number of measurements, and tends to the value $\tau_1 = \tau_2$ in the limit $N \to \infty$. This is shown in Fig. 5.7 illustrating the lifetime τ_1 as a function of the square of the Rabi frequency Ω. The Rabi frequency is proportional to the intensity I of the external field, meaning that higher Rabi frequencies give a faster measurement cycle. Therefore, by tuning the intensity of the laser we can increase the measurement frequency, and get closer to the QZE regime.

We also applied the QZE protocol to the specific case of atomic Li, by driving the transition between the configurations $1s2s^2$ and $1s2s2p$ with the respective lifetimes $\tau_1 = 17.6$ fs and $\tau_2 = 174$ fs. The results are shown in Fig. 5.7 for a number of different intensities. The maximal slowdown observed for the primary decay is about twice the unperturbed value, for a laser intensity of $I = 20.4$ TW/cm^2. The main reason why it is not possible to increase the lifetime further in this system, is that the Rabi frequency needed to perform measurements faster than τ_1 soon becomes larger that the transition energy $\omega = 2.5$ eV. In the strong coupling regime $\Omega/\omega \approx 1$ the execution of the protocol becomes harder, since the electron is no longer driven between the levels in the smooth fashion predicted by the rotating wave approximation (RWA). This issue should vanish for systems with longer Auger lifetimes, since for systems with a lifetime of ps the intensity could be reduced by

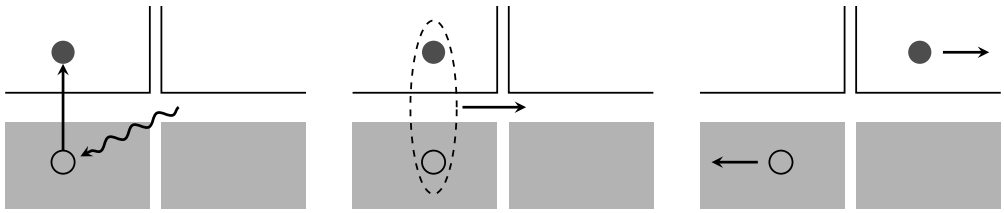

Figure 5.8: Schematic illustration of the charge separation process. In the first step an electron is excited in the donor and an exciton is created. The exciton then travels to the donor-acceptor interface, where it may dissociate into a spatially separated electron and hole.

four orders of magnitude. However, already the slowdown observed for Li should be clearly measurable, either in the time-domain [98] or as a narrowing of the spectral linewidth.

5.3 Charge-transfer dynamics

The importance of understanding the basic mechanisms of light harvesting devices, in which usable energy is extracted through photon absorption, cannot be overestimated. It is responsible for life in all organic matter and carries the potential to revolutionize our supply for energy. The process as it occurs in nature is also fascinating due to its high efficiency in separating the initial photo-induced exciton into electrons and holes [99]. To understand the details of the charge-separation process is therefore of great relevance, and has been a topic of extensive study [100, 101, 102, 103, 104]. To form an intuitive understanding of the light harvesting process we can think of it as consisting of three steps, shown in Fig. 5.8. In the first step an electron is excited from an occupied orbital in the donor system (for molecules typically the highest occupied molecular orbital, HOMO) to an initially empty orbital (typically the lowest unoccupied molecular orbital, LUMO) also in the donor. Due to interactions between the electron and hole they form a bound excitonic state. In the second step the exciton is transported to the donor-acceptor interface, and in the third step the exciton dissociates to create a charge separated state. Once charge separation has occurred, the electron and hole can be extracted as electric currents and used for power supply.

In realistic systems there are several factors complicating this simplified description of charge separation, and affect the question of how to increase its efficiency. Firstly, many features of the process are system dependent, and involve diverse phenomena such as multiple charge-transfer excitons [105, 106], charge delocalization [107], nuclear motion [108, 109] and disorder [110, 111]. Which process that will dominate in a given system is difficult to assess *a priori*, and therefore it is difficult to carry over results found in one system to another. Secondly, it is believed that part of the reason why the charge separation occurring in nature is so efficient, is because the systems are vastly complicated [99]. Starting from the initial excitation there is a large number of pathways available for the charge separation to

happen, and through coherent transport the probability that the system finds a way is very high. However, microscopically simulating these large systems in their entity is typically out of reach, and it is necessary to focus on the process in a single donor-acceptor molecule.

Due to the complexity of even a single donor-acceptor system it is generally not possible to treat their dynamics with numerically exact methods. Many studies have therefore relied on TDDFT for their description, since this allows a first-principle treatment of molecules with a couple of hundred constituent atoms. Further, TDDFT is in principle able to describe on equal footing all electronic excitations, such as Frenkel excitons, charge-transfer excitons and charge separated states, through the solution of the Kohn-Sham equations. It has been argued in several studies that in order to observe fast charge-separation dynamics in organic molecules it is necessary to take into account the effects of nuclear motion [108, 109]. By using two-dimensional coherent electron spectroscopy the authors could show that the oscillations in electron density observed during the charge-separation process was closely correlated with the frequency of a molecular vibrational mode. This was further substantiated by TDDFT simulations that when nuclei were free to move reproduced the experimentally observed charge-separation behavior, while for frozen nuclei gave a vanishing charge transfer.

It is then interesting to ask if these results are general, or if there are other systems where charge separation can occur independently of nuclear motion. From studies on atomic and molecular systems (see e.g. [112]), it is known that ultrafast oscillations in the electron density can be driven solely by electron correlation. Further, as noted already in the works discussed above, it seems that the main effect of nuclear vibrations is to shift the Kohn-Sham energy levels in time, so that they periodically come into contact with the energy levels of the acceptor molecule. However, as the exchange-correlation potential v_{xc} is usually taken within the ALDA, a TDDFT description is unable to account for spatially non-local and memory dependent effects in the interaction. Since including interaction effects beyond those contained in the ALDA could be expected to both shift and broaden the single particle energy levels, it is not unreasonable to think that a similar effect as that induced by nuclear motion could be obtained from a higher order treatment of electron-electron interactions.

In Paper IV we wanted to investigate the role of electronic correlations on the charge-separation process. We used the NEGF method together with the GKBA and treated interactions within second order perturbation theory, which is the simplest approximation going beyond a mean-field treatment (for details see Sec. 3.1). Since we are interested in the conceptual question of the role of interactions, we studied a prototypical donor-acceptor system consisting of a donor molecule with two active levels, a HOMO and a LUMO, coupled to the acceptor molecule C_{60} [113, 114]. We also assumed that the exciton is created at the donor-acceptor interface, so that we can ignore any effects due to exciton transport. The Hamiltonian we consider is $H(t) = H_d + H_a + H_{da} + H_{e-ph} + H_{ext}(t)$,

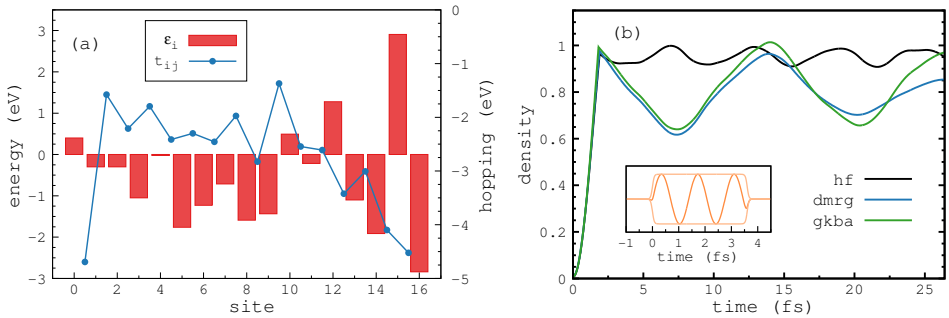

Figure 5.9: Comparison of results using time-dependent Hartree-Fock, non-equilibrium Green's functions with the second-Born approximation, and the time-dependent density matrix renormalization group method. For these calculations the C_{60} molecule is mapped onto a linear chain using the Lanczos method. The effective parameters of the Lanczos chain are shown in panel (a). The time-evolution of the LUMO density is shown in panel (b), with the time-dependent driving field in the inset. The figures are adapted from Paper IV.

where the donor is described by

$$H_d = \epsilon_H n_H + \epsilon_L n_L + U_{HL} n_H n_L. \tag{5.21}$$

Here ϵ_H and ϵ_L are the energies of the HOMO and LUMO levels respectively, and U_{HL} the strength of their mutual interaction. The acceptor is treated with a Pariser-Parr-Pople Hamiltonian [115, 116]

$$H_a = -\sum_{ij\sigma} t_{ij} \left(c^\dagger_{i\sigma} c_{j\sigma} + h.c. \right) + \sum_i V n_{i\uparrow} n_{i\downarrow} + \sum_{i \neq j} \lambda V \frac{n_i n_j}{\sqrt{\lambda^2 + d^2_{ij}}}, \tag{5.22}$$

and describes a single p_z-orbital on each carbon atom. The matrix t_{ij} is assumed to describe nearest-neighbor hopping, with slightly different values for bonds belonging to the same and different pentagons. The form of the interaction is taken from the parametrization of Ohno [117], and takes into account screening from the s- and p-orbitals not included explicitly in the description. We assume the molecules to be distant enough that only the LUMO and the closest carbon atom on the C_{60} have significant overlap. Then the donor-acceptor interaction is given by

$$H_{da} = -t_{da} \sum_\sigma \left(c^\dagger_{L\sigma} c_{1\sigma} + h.c. \right) + \sum_i \left[U_{Hi} \left(n_H - 2 \right) + U_{Li} n_L \right] \left(n_i - 1 \right), \tag{5.23}$$

with t_{da} being the strength of the coupling and U_{Hi} and U_{Li} the interaction of the donor orbitals with the C_{60} levels. The form of the interaction is chosen to vanish in the charge neutral ground state where $n_H = 2$, $n_L = 0$ and $n_i = 1$. We include electron-phonon interactions in the Ehrenfest approximation through the Hamiltonian

$$H_{e-ph} = \frac{p^2}{2M} + \frac{1}{2} M \omega^2_{ph} x^2 + g n_L x, \tag{5.24}$$

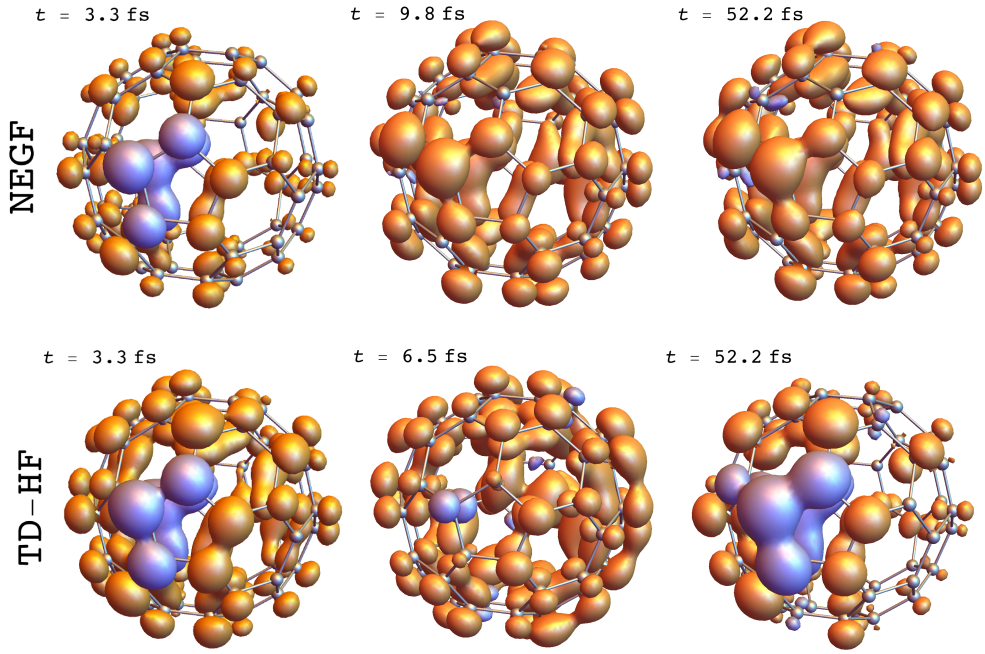

Figure 5.10: Charge dynamics in NEGF (upper row) and TD-HF (lower row) for the C_{60} acceptor. In each row, the three time snapshots depict the excess density in blue for $\Delta n < 0$ and in orange for $\Delta n > 0$. They respectively correspond to the time of maximum photo-charging of the LUMO ($t = 3.26$ fs), the first time the LUMO reaches minimum density (at $t = 9.78$ fs for NEGF and $t = 6.52$ fs in TD-HF) and its later occupation at $t = 52.16$ fs. The figures are adapted from Paper IV.

where x and p are classical variables. In addition M is the nuclear mass, ω_{ph} the phonon frequency and g the electron-phonon coupling. With this approach the equation of motion for the density matrix has to be solved in conjunction with Newtons equations for the classical variables.

To test the accuracy of the time-dependent Hartree-Fock (TD-HF) and NEGF approaches, we benchmarked the calculations towards the numerically exact tDMRG method. Since this method only works for one-dimensional systems, we mapped the C_{60} molecule onto a linear chain using the Lanczos method [2]. Due to limitations in the tDMRG method when treating non-local interactions, we restricted to the case of non-interacting C_{60} and interactions only between the LUMO level and the first atom in the chain. The linear chain resulting from the Lanczos method has the parameters shown in Fig. 5.9a, while the LUMO density is given in Fig. 5.9b. We see that the dynamics coming from tDMRG and NEGF are in very good agreement, while the TD-HF results are qualitatively different. This difference can be attributed to the additional correlation effects included in tDMRG and NEGF as compared to TD-HF.

In our simulations we were able to distinguish between two physical regimes, in which

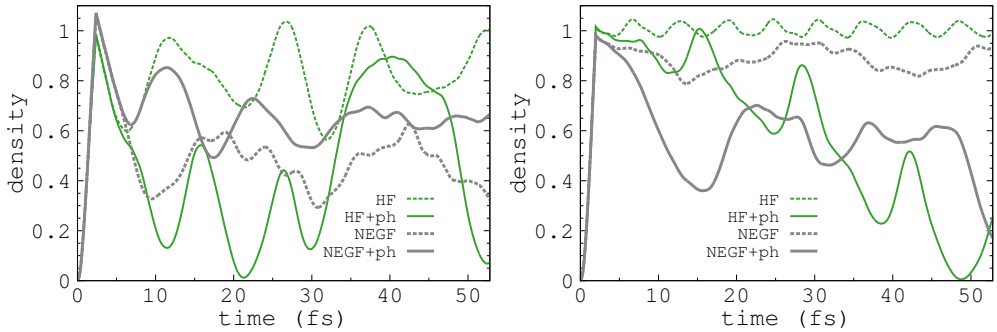

Figure 5.11: Evolution of the LUMO density for a system with HF energies on the donor and acceptor close to alignment (left), and far from alignment (right). The gray curves give the results from NEGF and the green curves those of HF. The solid lines are with electron-nuclear interaction, and the dashed lines without interaction. The figures are adapted from Paper IV.

the electronic correlations play a different role. The first is where the mean-field energy of the LUMO level is slightly out of resonance with the acceptor levels. In this regime, the renormalization of the energy levels coming from an inclusion of interactions beyond the mean-field level is enough to allow for charge transfer between the molecules. This is illustrated in Fig. 5.10 where we use a resonant external field to excite an electron from the HOMO to the LUMO level, and study the subsequent dynamics of the electron densities. In Fig. 5.10 we show the deviation Δn in density from the ground state value, given by

$$\Delta n(\mathbf{r}, t) = \sum_{ij} [\rho_{ij}(t) - \rho_{ij}(0)] \varphi_i^*(\mathbf{r}) \varphi_j(\mathbf{r}), \tag{5.25}$$

as computed with NEGF and TD-HF. In this expression φ_i is the p_z-orbital of the carbon atom labeled by i. For the dynamics including correlations, we see an initial depletion of density on the carbon atoms closest to the LUMO, followed by an increase in density due to charge transfer. After the initial pumping the density oscillates back and forth around a net value of $n_L \approx 0.4$, giving a quasi-stable state with a net charge transfer around 60 %. The initial behavior of the mean-field HF treatment is very similar, while the long time dynamics are quite different. After the initial charge transfer we observe that the LUMO density as found in HF periodically returns to $n_L = 1$, so the system never reaches a steady state and there is no net charge transfer. A way to understand this difference is that in the single-particle HF theory the state space seen by an electron on the LUMO is finite, and due to the high symmetry of C_{60} in fact rather small. The electron therefore oscillates coherently between the states in this finite space, and never thermalizes. In contrast, the correlated NEGF theory explores the full space of many-body states, which is large enough for the system to reach a quasi-steady state.

The other physical regime we explored is where the mean-field energy of the LUMO level is far out of resonance with the acceptor levels. In this case, the correlation effects are not

enough to induce charge transfer, and nuclear motion becomes essential. This is illustrated in Fig. 5.11, where we show both a case where nuclear motion is important and one where it is not. As pointed out earlier, the main effect of the nuclear motion is to renormalize the LUMO energy in time, so that it is periodically brought into contact with the acceptor levels. An interesting feature in the regime where nuclear motion is important, is that the charge transfer predicted by NEGF simulations is lower than that using TD-HF. Thus the effects of correlation in this case is quite different. We can understand this from a quasi-particle picture: Since in HF the quasi-particles have a a sharp energy, or equivalently an infinite life-time, when the HF LUMO level aligns with an unoccupied acceptor level due to phononic motion the charge-transfer is extremely efficient. In the NEGF treatment the quasi-particle weight is broadened over a range of energies, and charge-transfer occurs whenever spectral densities of the donor and acceptor overlap. As this overlap is always smaller than unity, only a fraction of the electron charge can be transferred.

Chapter 6

Conclusions and outlook

In this thesis we have discussed a number of physical processes of relevance for ultrafast and non-linear spectroscopy. In this chapter we summarize the main results of the papers, and discuss some possible extensions and applications for future work.

In Papers I and II we discussed the importance of electron-electron and electron-nuclear interactions for the process of desorption, and showed how a lattice treatment of electrons can be combined with a real-space description of nuclei in order to describe wavepacket splitting. We found that the desorption probability can be controlled by using a two-pulse protocol to manipulate the plasmonic response of the system. The exact numerical solution for a finite system was then compared to an approximate solution for an infinite system based on NEGF and Ehrenfest dynamics. The comparison was used both to assess the finite size effects in the exact solution and to benchmark the performance of the approximate solution. We found a good agreement between the electronic dynamics, while the semi-classical approximation was unable to describe splitting of the nuclear wavepacket, and therefore qualitatively failed to describe the nuclear dynamics in the regime of intermediate desorption yield. We also discussed in Paper I how to construct a current DFT for the combined electron-nuclear system, and extracted the exact Kohn-Sham potentials for the system during desorption. These potential have a highly non-adiabatic structure, with cusps developing for times in the vicinity of the wavepacket splitting, indicating that a description based on TDDFT in the adiabatic approximation might be challenging.

In Paper III we calculated the multi-photon absorption rates from InAs nanowires in the zincblende and wurtzite phase. Our results agree well with experiment and exhibit a strong dependence on the light polarization for the wurtzite phase. To perform these calculations we combined electronic structure calculations based on DFT and quasi-particle *GW* with an interpolation scheme based on Wannier functions. This allowed us to limit the size of

the k-point grid for the expensive GW calculations, while still obtaining good precision for the transition matrix elements. In Paper IV we studied charge-separation in a prototypical donor-acceptor system using NEGF with the GKBA. Being one of the first applications of the GKBA to large scale molecules, we benchmarked the results towards tDMRG and found a favorable agreement. We then investigated the effect of electronic correlations on the charge-separation process: We found that under certain conditions charge-separation can be driven solely by electronic correlations, while in other circumstances an electron-nuclear coupling is necessary to facilitate the process.

In Paper V we looked at Auger decay from a model atom, and computed the decay dynamics both in real-time and in frequency. This allowed us to also introduce an external laser field driving the atomic system during the decay, and to induce the quantum Zeno effect. By varying the intensity of the external field, we showed that the original lifetime of the Auger decay could be increased by about 100 % in Li and about 60 % in hollow Li^+. We presented evidence that the QZE is stronger in systems with longer lifetimes and larger transition energies, and that in such systems the QZE can be induced at moderate field intensities and light-matter coupling. Finally in Paper VI we discussed the process of second harmonic generation in two-level systems. Although parity forbidden in a perturbative treatment, we showed that a numerically exact solution of a two-level system coupled to quantum radiation gives a second harmonic signal. This was analyzed in terms of the parity of the coupled electron-photon states, which mix electronic states of different parity. We also identified distinct structures in the fluorescence spectrum of the two-level system that distinguish a semi-classical from a full quantum treatment.

There are several interesting extensions of this work that could be considered. It would be of interest to consider multi-photon absorption also from other semi-conductor systems. For this purpose it would be relevant to combine the computational elements used for our calculations into a larger framework where such simulations could be automatized. This would amount to constructing a simple interface between the electronic structure code (in our context ABINIT), the Wannier interpolation post-processing tools (in our context WANNIER90 and POST90), and the code calculating the multi-photon rates. Such a package could be of large interest for experiment. To explicitly account for the field enhancement due to nanostructure morphology, these calculations could also be combined with the solution of Maxwell's equations in the specific geometry. Finally, it is not unreasonable to believe that for many systems surface and interface effects could be of relevance, and therefore an extension of the method to take such effects into account could provide further insight into the multi-photon process.

Another possibility is to take advantage of the numerical speed-up provided by using the NEGF method together with the GKBA, and study more realistic adsorbate-surface systems. Based on the results of Papers II and IV, it seems reasonable that a perturbative treatment of electron-electron interactions on the level of second Born is enough to capture the

dominant aspects of electron correlations in such systems. To address desorption dynamics in an approximate fashion, it would be necessary to treat in an approximate manner the splitting of the nuclear wavepacket. For wavefunction based methods there are several routes available for this purpose, such as surface hopping algorithms and semi-classical treatments based on an exact factorization of the electron-nuclear wavefunction. To find a similar approach within Green's function theory would be both an interesting and important development. On the electronic side a GKBA treatment would allow to take explicitly into account the two-dimensional character of the surface. This would give the opportunity to address the effects on electronic and nuclear dynamics of different adsorbate positions relative to the surface (on top, bridge and centered). It would also open the possibility to study Auger decay from adsorbates, and assess the surface's effect on lifetimes and lineshapes.

A related possibility is to study more realistic donor-acceptor systems, where both molecules are explicitly treated in some tight-binding approximation. This would allow to target more specific systems, and identify molecules where electron correlations play a substantial role. As an additional ingredient, the NEGF treatment also allows to attach the donor-acceptor system to external baths, and so to effectively model the chemical environment. This could potentially have a large effect on the charge-separation behavior, both due to a reduction of image charge effects and due to additional decoherence.

The predictions of a quantum Zeno effect in atomic Auger decay would be very interesting to test in experiment. Even though the systems we have considered so far are not ideal candidates for such an experiment, the increase in lifetime both in Li and Li^+ should be clearly measurable. There are however systems where the Auger lifetime is on the order of nano- or even microseconds, which would allow for an experiment to be performed at much lower intensity than suggested in the paper. Similarly the quantum signatures in fluorescence signals from second harmonic generation would be interesting to investigate in experiments. This would require a strong light-matter coupling, that can be achieved either by using intense radiation such as a free electron laser, or by considering a semi-conducting effective two-level system.

In a more general sense, the theoretical modeling of ultrafast processes poses a number of interesting challenges for the future. To address non-adiabatic dynamics in systems of realistic size, a promising way forward seems to be to combine elements of different theories in order to make use of their different strengths. One such example is the hybrid DFT-NEGF introduced in [118], that combines the non-local and memory dependent perturbative self-energy of NEGF with the local non-perturbative exchange-correlation potential of DFT. A similar route could be considered by combining a perturbative non-local self-energy with a local non-perturbative self-energy from dynamical mean-field theory. A different way to combine methods is to partition a system in such a way that various parts are described by different levels of approximations. As an example, an adsorbate-surface could most likely

be described by treating the region close to the adsorbate using a higher order approximation while the region further away is treated in a more simplified manner. This would allow for numerically efficient simulations while retaining a detailed description of the most important parts of the system. Finally we note that hybrid methods could be valuable also for the study of magnetic systems, since magnetism arises from a competition of the Pauli principle and strong correlations. To study such systems with the Green's function method is both within reach and of interest to a large number of experiments. Among other things, it would allow for a microscopic simulations of spin dynamics and time-dependent magnetic response.

References

[1] W. Kohn. Nobel lecture: Electronic structure of matter-wave functions and density functionals. *Rev. Mod. Phys.*, 71:1253–1266, Oct 1999.

[2] Cornelius Lanczos. An iteration method for the solution of the eigenvalue problem of linear differential and integral operators. *J. Res. Natl. Bur. Stand. B*, 45:255–282, 1950.

[3] Kenneth G. Wilson. Renormalization group and critical phenomena. I. Renormalization group and the Kadanoff scaling picture. *Phys. Rev. B*, 4:3174–3183, Nov 1971.

[4] Kenneth G. Wilson. Renormalization group and critical phenomena. II. Phase-space cell analysis of critical behavior. *Phys. Rev. B*, 4:3184–3205, Nov 1971.

[5] S. R. White and R. M. Noack. Real-space quantum renormalization groups. *Phys. Rev. Lett.*, 68:3487–3490, Jun 1992.

[6] Steven R. White. Density matrix formulation for quantum renormalization groups. *Phys. Rev. Lett.*, 69:2863–2866, Nov 1992.

[7] Steven R. White. Density-matrix algorithms for quantum renormalization groups. *Phys. Rev. B*, 48:10345–10356, Oct 1993.

[8] Ulrich Schollwöck. The density-matrix renormalization group: a short introduction. *Philos. Trans. Royal Soc. A*, 369(1946):2643–2661, 2011.

[9] J. Eisert, M. Cramer, and M. B. Plenio. Area laws for the entanglement entropy. *Rev. Mod. Phys.*, 82:277–306, Feb 2010.

[10] Ulrich Schollwöck. Time-dependent density-matrix renormalization-group methods. *Journal of the Physical Society of Japan*, 74:246–255, 2005.

[11] P. Hohenberg and W. Kohn. Inhomogeneous electron gas. *Phys. Rev.*, 136:B864–B871, Nov 1964.

[12] W. Kohn and L. J. Sham. Self-consistent equations including exchange and correlation effects. *Phys. Rev.*, 140:A1133–A1138, Nov 1965.

[13] Mel Levy. Universal variational functionals of electron densities, first-order density matrices, and natural spin-orbitals and solution of the v-representability problem. *Proceedings of the National Academy of Sciences*, 76(12):6062–6065, 1979.

[14] U von Barth and L Hedin. A local exchange-correlation potential for the spin polarized case. i. *Journal of Physics C: Solid State Physics*, 5(13):1629, 1972.

[15] G. Vignale and Mark Rasolt. Density-functional theory in strong magnetic fields. *Phys. Rev. Lett.*, 59:2360–2363, Nov 1987.

[16] O. Gunnarsson and K. Schönhammer. Density-functional treatment of an exactly solvable semiconductor model. *Phys. Rev. Lett.*, 56:1968–1971, May 1986.

[17] Erich Runge and E. K. U. Gross. Density-functional theory for time-dependent systems. *Phys. Rev. Lett.*, 52:997–1000, Mar 1984.

[18] Robert van Leeuwen. Mapping from densities to potentials in time-dependent density-functional theory. *Phys. Rev. Lett.*, 82:3863–3866, May 1999.

[19] Claudio Verdozzi. Time-dependent density-functional theory and strongly correlated systems: Insight from numerical studies. *Phys. Rev. Lett.*, 101:166401, Oct 2008.

[20] I. V. Tokatly. Time-dependent current density functional theory on a lattice. *Phys. Rev. B*, 83:035127, Jan 2011.

[21] M. Farzanehpour and I. V. Tokatly. Time-dependent density functional theory on a lattice. *Phys. Rev. B*, 86:125130, Sep 2012.

[22] K. Schönhammer, O. Gunnarsson, and R. M. Noack. Density-functional theory on a lattice: Comparison with exact numerical results for a model with strongly correlated electrons. *Phys. Rev. B*, 52:2504–2510, Jul 1995.

[23] C.-O. Almbladh and U. von Barth. Exact results for the charge and spin densities, exchange-correlation potentials, and density-functional eigenvalues. *Phys. Rev. B*, 31:3231–3244, Mar 1985.

[24] T. Kreibich and E. K. U. Gross. Multicomponent density-functional theory for electrons and nuclei. *Phys. Rev. Lett.*, 86:2984–2987, Apr 2001.

[25] Thomas Kreibich, Robert van Leeuwen, and E. K. U. Gross. Multicomponent density-functional theory for electrons and nuclei. *Phys. Rev. A*, 78:022501, Aug 2008.

[26] I. V. Tokatly. Time-dependent density functional theory for many-electron systems interacting with cavity photons. *Phys. Rev. Lett.*, 110:233001, Jun 2013.

[27] M. Farzanehpour and I. V. Tokatly. Quantum electrodynamical time-dependent density-functional theory for many-electron systems on a lattice. *Phys. Rev. B*, 90:195149, Nov 2014.

[28] Michael Ruggenthaler, Johannes Flick, Camilla Pellegrini, Heiko Appel, Ilya V. Tokatly, and Angel Rubio. Quantum-electrodynamical density-functional theory: Bridging quantum optics and electronic-structure theory. *Phys. Rev. A*, 90:012508, Jul 2014.

[29] Ali Abedi, Neepa T. Maitra, and E. K. U. Gross. Exact factorization of the time-dependent electron-nuclear wave function. *Phys. Rev. Lett.*, 105:123002, Sep 2010.

[30] Julian Schwinger. Quantum electrodynamics. I. A covariant formulation. *Phys. Rev.*, 74:1439–1461, Nov 1948.

[31] R. P. Feynman. Space-time approach to quantum electrodynamics. *Phys. Rev.*, 76:769–789, Sep 1949.

[32] Takeo Matsubara. A new approach to quantum-statistical mechanics. *Progress of Theoretical Physics*, 14(4):351–378, 1955.

[33] L.P. Kadanoff and G. Baym. *Quantum statistical mechanics: Green's function methods in equilibrium and nonequilibrium problems*. Frontiers in physics. W.A. Benjamin, 1962.

[34] Julian Schwinger. Brownian motion of a quantum oscillator. *Journal of Mathematical Physics*, 2(3):407–432, 1961.

[35] L. V. Keldysh. Diagram technique for nonequilibrium processes. *Zh. Eksp. Teor. Fiz.*, 47:1515–1527, 1964. [Sov. Phys. JETP 20, 1018 (1965)].

[36] G. Stefanucci and R. van Leeuwen. *Nonequilibrium Many-Body Theory of Quantum Systems: A Modern Introduction*. Cambridge University Press, 2013.

[37] D. C. Langreth. *Linear and Nonlinear Electron Transport in Solids*. Plenum, New York, 1976.

[38] G. C. Wick. The evaluation of the collision matrix. *Phys. Rev.*, 80:268–272, Oct 1950.

[39] A.L. Fetter and J.D. Walecka. *Quantum Theory of Many-particle Systems*. Dover Books on Physics. Dover Publications, 2003.

[40] P. Lipavský, V. Špička, and B. Velický. Generalized Kadanoff-Baym ansatz for deriving quantum transport equations. *Phys. Rev. B*, 34:6933–6942, Nov 1986.

[41] S. Latini, E. Perfetto, A.-M. Uimonen, R. van Leeuwen, and G. Stefanucci. Charge dynamics in molecular junctions: Nonequilibrium Green's function approach made fast. *Phys. Rev. B*, 89:075306, Feb 2014.

[42] Fabien Bruneval, Nathalie Vast, and Lucia Reining. Effect of self-consistency on quasiparticles in solids. *Phys. Rev. B*, 74:045102, Jul 2006.

[43] G. Onida, L. Reining, and A. Rubio. Electronic excitations: density-functional versus many-body Green's-function approaches. *Rev. Mod. Phys.*, 74:601–659, 2002.

[44] Gregory H. Wannier. The structure of electronic excitation levels in insulating crystals. *Phys. Rev.*, 52:191–197, Aug 1937.

[45] Nicola Marzari and David Vanderbilt. Maximally localized generalized Wannier functions for composite energy bands. *Phys. Rev. B*, 56:12847–12865, Nov 1997.

[46] Xinjie Wang, Jonathan R. Yates, Ivo Souza, and David Vanderbilt. Ab initio calculation of the anomalous Hall conductivity by Wannier interpolation. *Phys. Rev. B*, 74:195118, Nov 2006.

[47] J.D. Jackson. *Classical electrodynamics*. Wiley, 1975.

[48] Aleksei Zheltikov, Anne L'Huillier, and Ferenc Krausz. *Nonlinear optics*. Springer, New York, 2007.

[49] G. Grynberg, A. Aspect, C. Fabre, and C. Cohen-Tannoudji. *Introduction to Quantum Optics: From the Semi-classical Approach to Quantized Light*. Cambridge University Press, 2010.

[50] Chen Guo, Anne Harth, Stefanos Carlström, Yu-Chen Cheng, Sara Mikaelsson, Erik Mårsell, Christoph Heyl, Miguel Miranda, Mathieu Gisselbrecht, Mette B Gaarde, Kenneth J Schafer, Anders Mikkelsen, Johan Mauritsson, Cord L Arnold, and Anne L'Huillier. Phase control of attosecond pulses in a train. *Journal of Physics B: Atomic, Molecular and Optical Physics*, 51(3):034006, 2018.

[51] G. F Bassani and G. P. Parravicini. *Electronic states and optical transitions in solids*. Pergamon Press, 1975.

[52] N.W. Ashcroft and N.D. Mermin. *Solid State Physics*. Holt, Rinehart and Winston, 1976.

[53] M. Aeschlimann, M. Bauer, D. Bayer, T. Brixner, F. J. Garcia de Abajo, W. Pfeiffer, M. Rohmer, C. Spindler, and F. Steeb. Adaptive subwavelength control of nano-optical fields. *Nature*, 446:301, 2007.

[54] E. Mårsell, R. Svärd, M. Miranda, C. Guo, A. Harth, E. Lorek, J. Mauritsson, C. L. Arnold, H. Xu, A. L'Huillier, A. Mikkelsen, and A. Losquin. Direct subwavelength imaging and control of near-field localization in individual silver nanocubes. *Applied Physics Letters*, 107(20):201111, 2015.

[55] E. Mårsell, A. Losquin, R. Svärd, M. Miranda, C. Guo, A. Harth, E. Lorek, J. Mauritsson, C. L Arnold, H. Xu, A. L'Huillier, and A. Mikkelsen. Nanoscale imaging of local few-femtosecond near-field dynamics within a single plasmonic nanoantenna. *Nano letters*, 15(10):6601–6608, October 2015.

[56] Michele Amato, Thanayut Kaewmaraya, Alberto Zobelli, Maurizia Palummo, and Riccardo Rurali. Crystal phase effects in si nanowire polytypes and their homojunctions. *Nano Letters*, 16(9):5694–5700, 2016. PMID: 27530077.

[57] Michele Amato, Maurizia Palummo, Riccardo Rurali, and Stefano Ossicini. Silicon-germanium nanowires: Chemistry and physics in play, from basic principles to advanced applications. *Chemical Reviews*, 114(2):1371–1412, 2014. PMID: 24266833.

[58] Zhiqiang Liang, Jun Sun, Yueyue Jiang, Lin Jiang, and Xiaodong Chen. Plasmonic enhanced optoelectronic devices. *Plasmonics*, 9(4):859–866, Aug 2014.

[59] Soo Hoon Chew, Kellie Pearce, Christian Späth, Alexander Guggenmos, Jürgen Schmidt, Frederik Süßmann, Matthias F. Kling, Ulf Kleineberg, Erik Mårsell, Cord L. Arnold, Eleonora Lorek, Piotr Rudawski, Chen Guo, Miguel Miranda, Fernando Ardana, Johan Mauritsson, Anne L'Huillier, and Anders Mikkelsen. *Imaging Localized Surface Plasmons by Femtosecond to Attosecond Time-Resolved Photoelectron Emission Microscopy - "ATTO-PEEM"*, chapter 10, pages 325–364. Wiley-Blackwell, 2015.

[60] Y. Pavlyukh, M. Schüler, and J. Berakdar. Single- or double-electron emission within the Keldysh nonequilibrium Green's function and Feshbach projection operator techniques. *Phys. Rev. B*, 91:155116, Apr 2015.

[61] F. Sirotti, N. Beaulieu, A. Bendounan, M. G. Silly, C. Chauvet, G. Malinowski, G. Fratesi, V. Véniard, and G. Onida. Multiphoton k-resolved photoemission from gold surface states with 800-nm femtosecond laser pulses. *Phys. Rev. B*, 90:035401, Jul 2014.

[62] Z. Zanolli, F. Fuchs, J. Furthmüller, U. von Barth, and F. Bechstedt. Model GW band structure of InAs and GaAs in the wurtzite phase. *Phys. Rev. B*, 75:245121, Jun 2007.

[63] Hendrik J. Monkhorst and James D. Pack. Special points for brillouin-zone integrations. *Phys. Rev. B*, 13:5188–5192, Jun 1976.

[64] A. G. Milnes and D. L. Feucht. *Heterojunctions and Metal-Semiconductor Junctions*. Academic, New York, 1972.

[65] M. Lewenstein, Ph. Balcou, M. Yu. Ivanov, Anne L'Huillier, and P. B. Corkum. Theory of high-harmonic generation by low-frequency laser fields. *Phys. Rev. A*, 49:2117–2132, Mar 1994.

[66] Michele Cini, Andrea D'Andrea, and Claudio Verdozzi. Many-photon effects in inelastic light scattering. *Physics Letters A*, 180(6):430–434, 1993.

[67] Michele Cini, Andrea D'Andrea, and Claudio Verdozzi. Many-photon effects in inelastic light scattering: Theory and model applications. *International Journal of Modern Physics B*, 09(10):1185–1204, 1995.

[68] Shu He, Chen Wang, Qing-Hu Chen, Xue-Zao Ren, Tao Liu, and Ke-Lin Wang. First-order corrections to the rotating-wave approximation in the jaynes-cummings model. *Phys. Rev. A*, 86:033837, Sep 2012.

[69] Cohen-Tannoudji C. N. *The Autler-Townes Effect Revisited*. Springer, New York, 1996.

[70] S. Holloway and J.K. Nørskov. *Bonding at Surfaces*. Surface science lecture notes. Liverpool University Press, 1991.

[71] John C. Tully. Molecular dynamics with electronic transitions. *The Journal of Chemical Physics*, 93(2):1061–1071, 1990.

[72] Linjun Wang, Alexey Akimov, and Oleg V. Prezhdo. Recent progress in surface hopping: 2011-2015. *The Journal of Physical Chemistry Letters*, 7(11):2100–2112, 2016. PMID: 27171314.

[73] Federica Agostini, Seung Kyu Min, Ali Abedi, and E. K. U. Gross. Quantum-classical nonadiabatic dynamics: Coupled- vs independent-trajectory methods. *Journal of Chemical Theory and Computation*, 12(5):2127–2143, 2016. PMID: 27030209.

[74] Seung Kyu Min, Federica Agostini, Ivano Tavernelli, and E. K. U. Gross. Ab initio nonadiabatic dynamics with coupled trajectories: A rigorous approach to quantum (de)coherence. *The Journal of Physical Chemistry Letters*, 8(13):3048–3055, 2017. PMID: 28618782.

[75] M. Schüler, J. Berakdar, and Y. Pavlyukh. Time-dependent many-body treatment of electron-boson dynamics: Application to plasmon-accompanied photoemission. *Phys. Rev. B*, 93:054303, Feb 2016.

[76] Niko Säkkinen, Yang Peng, Heiko Appel, and Robert van Leeuwen. Many-body Green's function theory for electron-phonon interactions: Ground state properties of the Holstein dimer. *The Journal of Chemical Physics*, 143(23):234101, 2015.

[77] P. W. Anderson. Localized magnetic states in metals. *Phys. Rev.*, 124:41–53, Oct 1961.

[78] D. M. Newns. Self-consistent model of hydrogen chemisorption. *Phys. Rev.*, 178:1123–1135, Feb 1969.

[79] T B Grimley. The electron density in a metal near a chemisorbed atom or molecule. *Proceedings of the Physical Society*, 92(3):776, 1967.

[80] B. I. Lundqvist. Characteristic structure in core electron spectra of metals due to the electron-plasmon coupling. *Physik der kondensierten Materie*, 9(3):236–248, Jul 1969.

[81] David C. Langreth. Singularities in the x-ray spectra of metals. *Phys. Rev. B*, 1:471–477, Jan 1970.

[82] Seokmin Shin and Horia Metiu. Nonadiabatic effects on the charge transfer rate constant: A numerical study of a simple model system. *The Journal of Chemical Physics*, 102(23):9285–9295, 1995.

[83] Marc Puig von Friesen, C. Verdozzi, and C.-O. Almbladh. Kadanoff-Baym dynamics of Hubbard clusters: Performance of many-body schemes, correlation-induced damping and multiple steady and quasi-steady states. *Phys. Rev. B*, 82:155108, Oct 2010.

[84] Charles S. Fadley. Angle-resolved x-ray photoelectron spectroscopy. *Progress in Surface Science*, 16(30):275 – 3880, 1984.

[85] D. Chattarji. *The Theory of Auger Transitions*. Elsevier Science, 2012.

[86] M. Cini. Density of states of two interacting holes in a solid. *Solid State Communications*, 20(6):605 – 607, 1976.

[87] M. Cini. Two hole resonances in the XVV Auger spectra of solids. *Solid State Communications*, 88(11):1101 – 1104, 1993. Special Issue A Celebratory Issue to Commemorate 30 Years of Solid State Communications.

[88] G. A. Sawatzky. Quasiatomic Auger spectra in narrow-band metals. *Phys. Rev. Lett.*, 39:504–507, Aug 1977.

[89] Electron correlations in narrow energy bands. *Proceedings of the Royal Society of London A*, 276(1365):238–257, 1963.

[90] Claudio Verdozzi, Michele Cini, and Andrea Marini. Auger spectroscopy of strongly correlated systems: present status and future trends. *Journal of Electron Spectroscopy and Related Phenomena*, 117-118:41 – 55, 2001. Strongly correlated systems.

[91] C. O. Almbladh. Incomplete relaxation in a model problem for the Auger process. *Il Nuovo Cimento B (1971-1996)*, 23(1):75–89, Sep 1974.

[92] O. Gunnarsson and K. Schönhammer. Dynamical theory of Auger processes. *Phys. Rev. B*, 22:3710–3733, Oct 1980.

[93] B. Misra and E. C. G. Sudarshan. The Zeno's paradox in quantum theory. *Journal of Mathematical Physics*, 18(4):756–763, 1977.

[94] Richard J Cook. What are quantum jumps? *Physica Scripta*, 1988(T21):49, 1988.

[95] Wayne M. Itano, D. J. Heinzen, J. J. Bollinger, and D. J. Wineland. Quantum Zeno effect. *Phys. Rev. A*, 41:2295–2300, Mar 1990.

[96] M. C. Fischer, B. Gutiérrez-Medina, and M. G. Raizen. Observation of the quantum Zeno and anti-Zeno effects in an unstable system. *Phys. Rev. Lett.*, 87:040402, Jul 2001.

[97] Y. S. Patil, S. Chakram, and M. Vengalattore. Measurement-induced localization of an ultracold lattice gas. *Phys. Rev. Lett.*, 115:140402, Oct 2015.

[98] M. Drescher, M. Hentschel, R. Kienberger, M. Uiberacker, V. Yakovlev, A. Scrinzi, Th. Westerwalbesloh, U. Kleineberg, U. Heinzmann, and F. Krausz. Time-resolved atomic inner-shell spectroscopy. *Nature*, 419:803, Sep 2002.

[99] Gregory S. Engel, Tessa R. Calhoun, Elizabeth L. Read, Tae-Kyu Ahn, Tomas Mancal, Yuan-Chung Cheng, Robert E. Blankenship, and Graham R. Fleming. Evidence for wavelike energy transfer through quantum coherence in photosynthetic systems. *Nature*, 446:782, Apr 2007.

[100] H. Sirringhaus, P. J. Brown, R. H. Friend, M. M. Nielsen, K. Bechgaard, B. M. W. Langeveld-Voss, A. J. H. Spiering, R. A. J. Janssen, E. W. Meijer, P. Herwig, and D. M. de Leeuw. Two-dimensional charge transport in self-organized, high-mobility conjugated polymers. *Nature*, 401:685, 1999/10/14/online.

[101] Gang Li, Rui Zhu, and Yang Yang. Polymer solar cells. *Nature Photonics*, 6:153, Feb 2012.

[102] Marco Bernardi, Maurizia Palummo, and Jeffrey C. Grossman. Extraordinary sunlight absorption and one nanometer thick photovoltaics using two-dimensional monolayer materials. *Nano Letters*, 13(8):3664–3670, 2013. PMID: 23750910.

[103] S. E. Canton, K. S. Kjær, G. Vankó, T. B. van Driel, S.-I. Adachi, A. Bordage, C. Bressler, P. Chabera, M. Christensen, A. O. Dohn, A. Galler, W. Gawelda, D. Gosztola, K. Haldrup, T. Harlang, Y. Liu, K. B. Møller, Z. Németh, S. Nozawa, M. Pápai, T. Sato, T. Sato, K. Suarez-Alcantara, T. Togashi, K. Tono, J. Uhlig, D. A. Vithanage, K. Wärnmark, M. Yabashi, J. Zhang, V. Sundström, and M. M. Nielsen. Visualizing the non-equilibrium dynamics of photoinduced intramolecular electron transfer with femtosecond x-ray pulses. *Nature Communications*, 6:6359, 2015.

[104] Albert Polman, Mark Knight, Erik C. Garnett, Bruno Ehrler, and Wim C. Sinke. Photovoltaic materials: Present efficiencies and future challenges. *Science*, 352(6283), 2016.

[105] G. Grancini, M. Maiuri, D. Fazzi, A. Petrozza, H-J. Egelhaaf, D. Brida, G. Cerullo, and G. Lanzani. Hot exciton dissociation in polymer solar cells. *Nature Materials*, 12:29–33, 2013.

[106] Maurizia Palummo, Marco Bernardi, and Jeffrey C. Grossman. Exciton radiative lifetimes in two-dimensional transition metal dichalcogenides. *Nano Letters*, 15(5):2794–2800, 2015. PMID: 25798735.

[107] Artem A. Bakulin, Akshay Rao, Vlad G. Pavelyev, Paul H. M. van Loosdrecht, Maxim S. Pshenichnikov, Dorota Niedzialek, Jérôme Cornil, David Beljonne, and Richard H. Friend. The role of driving energy and delocalized states for charge separation in organic semiconductors. *Science*, 335(6074):1340–1344, 2012.

[108] C. A. Rozzi, S. M. Falke, N. Spallanzani, R. Angel, E. Molinari, D. Brida, M. Maiuri, H. Cerullo, G. Schramm, J. Christoffers, and C. Lienau. Quantum coherence controls the charge separation in a prototypical artificial light-harvesting system. *Nature Communications*, 4, Mar 2013.

[109] Sarah Maria Falke, Carlo Andrea Rozzi, Daniele Brida, Margherita Maiuri, Michele Amato, Ephraim Sommer, Antonietta De Sio, Angel Rubio, Giulio Cerullo, Elisa Molinari, and Christoph Lienau. Coherent ultrafast charge transfer in an organic photovoltaic blend. *Science*, 344(6187):1001–1005, 2014.

[110] Gregory L. Whiting, Henry J. Snaith, Saghar Khodabakhsh, Jens W. Andreasen, Dag W. Breiby, Martin M. Nielsen, Neil C. Greenham, Richard H. Friend, and Wilhelm T. S. Huck. Enhancement of charge-transport characteristics in polymeric films using polymer brushes. *Nano Letters*, 6(3):573–578, 2006. PMID: 16522065.

[111] Samantha N. Hood and Ivan Kassal. Entropy and disorder enable charge separation in organic solar cells. *The Journal of Physical Chemistry Letters*, 7(22):4495–4500, 2016. PMID: 27783509.

[112] Giuseppe Sansone, Thomas Pfeifer, Konstantinos Simeonidis, and Alexander I. Kuleff. Electron correlation in real time. *ChemPhysChem*, 13(3):661–680, 2012.

[113] Y. Pavlyukh and J. Berakdar. Communication: Superatom molecular orbitals: New types of long-lived electronic states. *The Journal of Chemical Physics*, 135(20):201103, 2011.

[114] Sergey Usenko, Michael Schüler, Armin Azima, Markus Jakob, Leslie L Lazzarino, Yaroslav Pavlyukh, Andreas Przystawik, Markus Drescher, Tim Laarmann, and Jamal Berakdar. Femtosecond dynamics of correlated many-body states in C_{60} fullerenes. *New Journal of Physics*, 18(11):113055, 2016.

[115] Rudolph Pariser and Robert G. Parr. A semi-empirical theory of the electronic spectra and electronic structure of complex unsaturated molecules. I. *The Journal of Chemical Physics*, 21(3):466–471, 1953.

[116] J. A. Pople. Electron interaction in unsaturated hydrocarbons. *Trans. Faraday Soc.*, 49:1375–1385, 1953.

[117] Kimio Ohno. Some remarks on the Pariser-Parr-Pople method. *Theoretica chimica acta*, 2(3):219–227, 1964.

[118] M. Hopjan, D. Karlsson, S. Ydman, C. Verdozzi, and C.-O. Almbladh. Merging features from Green's functions and time dependent density functional theory: A route to the description of correlated materials out of equilibrium? *Phys. Rev. Lett.*, 116:236402, Jun 2016.

Scientific publications

Paper 1

Paper II

Paper III

Paper IV

Paper v

Paper VI

Appendix

Appendix A

Matrix structure in exact diagonalization

We now give a brief description of the structure of the Hamiltonian matrix, as used in our numerical implementation. Given the many-body basis discussed in the section 2.1, we want to order the states in such a way as to keep the non-zero matrix elements of H as close as possible to the diagonal. In general the matrix H will have a block form (see Fig. A.1), and since the electronic matrix H_e is typically more dense than H_{e-b} and H_{e-n}, we want to limit the size of the blocks corresponding to H_e. This is achieved by the following ordering procedure, where we start by fixing the bosonic states to their lowest values $n_{k_i} = 0$ and $n = 1$:

1. Run through all electronic states. This gives the first N_e basis states $|l\rangle$.
2. Update $k_i = k_i + 1$ and repeat step 1, until $k_i = N_{k_i}$. This gives the first $N_e \prod_{j=1}^{i} N_{k_j}$ basis states $|l\rangle$.
3. Update $i = i + 1$ and repeat steps 1 and 2, until $i = K$. This gives the first $N_e N_b$ basis states $|l\rangle$.
4. Update $n = n + 1$ and repeat steps 1, 2 and 3, until $n = N_n$.

An example of the Hamiltonian matrix for a single boson mode ($K = 1$) with diagonal electron-boson coupling $g_{ijk} = g\delta_{ij}$ is given in Fig. A.1. Here the size of the shaded blocks is N_e, corresponding to the size of H_e. Due to the form of the electron-boson coupling, this particular ordering of the basis gives $H_{ij} = 0$ for $|i - j| > 2N_e$. Also in the general case, the non-zero elements of H will be confined to lie along the diagonal.

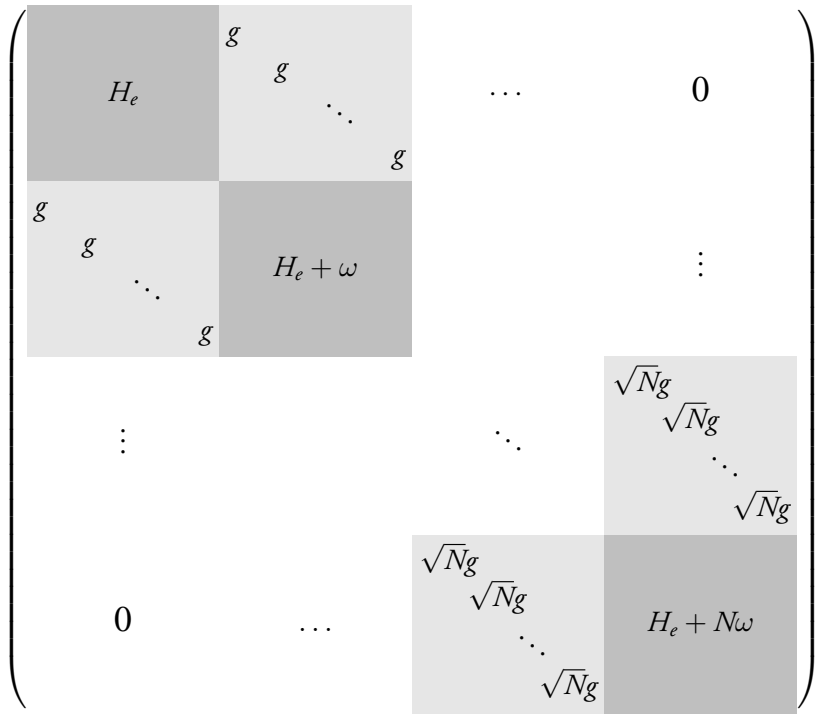

Figure A.1: The Hamiltonian matrix $H = H_e + H_{e-b}$ for a single boson mode with diagonal coupling $g_{ijk} = g\delta_{ij}$ and a cutoff $N_{k_1} = N$.

Appendix B

TDDFT for lattice electrons and nuclei

Consider a system of n interacting electrons on a lattice coupled to N interacting nuclei, described by the collective coordinates $r = \{r_1, \ldots, r_n\}$ and $R = \{R_1, \ldots, R_N\}$ where $r_i = (\mathbf{r}_i, \sigma_i)$ and $R_i = (\mathbf{R}_i, \zeta_i)$ includes both position and spin. For a Hubbard type system the Hamiltonian is written

$$H = \sum_{i,\sigma} U n_{i,\sigma} n_{i,-\sigma} + \sum_{ij,\sigma} \left(T_{ij}^{ext}(t) c_{i,\sigma}^{\dagger} c_{j,\sigma} + h.c. \right) + \sum_{i} \left[\frac{\mathbf{P}_i^2}{2m} + V_n^{ext}(\mathbf{R}_i, t) \right] \tag{B.1}$$
$$+ \sum_{ij} V(\mathbf{R}_i, \mathbf{R}_j) + \sum_{ij,\sigma} H_{ij}^{int}(\mathbf{R}) \left(c_{i,\sigma}^{\dagger} c_{j,\sigma} + h.c. \right),$$

where the electrons can move on a lattice with M sites $\mathbf{x} = \{\mathbf{x}_1, \ldots, \mathbf{x}_M\}$ under the action of the operators c_i and $\mathbf{R} = (\mathbf{R}_1, \ldots, \mathbf{R}_N)$. The state of the system is uniquely determined from the Schrödinger equation once we specify the two external fields T_{ij}^{ext} and V_n^{ext} as well as the initial state $|\psi_0\rangle$. Using the lattice basis for the electrons and the position basis for the nuclei the Schrödinger equation is explicitly given by

$$i\frac{\partial}{\partial t}\psi(r, R, t) = \left[\sum_{ij} U \delta_{\mathbf{r}_i, \mathbf{r}_j} \delta_{\sigma_i, -\sigma_j} + \sum_{i} \left(-\frac{1}{2m} \nabla_{\mathbf{R}_i}^2 + V_n^{ext}(\mathbf{R}_i, t) \right) \right. \tag{B.2}$$
$$\left. + \sum_{ij} V(\mathbf{R}_i, \mathbf{R}_j) \right] \psi(r, R, t) + \sum_{ij} \left[H_{ij}^{int}(\mathbf{R}) + T_{ij}^{ext}(t) \right] \psi(\{\mathbf{r}_i \to \mathbf{r}_j\}, R, t),$$

where the sum in the last line is over all possible configurations of the electrons originally at $\mathbf{r} = (\mathbf{r}_1, \ldots, \mathbf{r}_n)$ that can be reached by moving a single electron. Given the wavefunc-

tion at time t we generalize the complex electronic current of [20] and define the nuclear probability density [25] by

$$Q_{ij}^{\sigma}(t) = T_{ij}^{ext}(t)\rho_{ij}^{\sigma}(t) + \tilde{\rho}_{ij}^{\sigma}(t) \tag{B.3a}$$

$$\Gamma(X,t) = \sum_{r} \int \prod_{i=2}^{N} dR_i \, |\psi(r, X, R_2, \ldots, R_N, t)|^2, \tag{B.3b}$$

where the sum over r_i and integral over R_i are assumed to include a sum over the spins σ_i and ζ_i respectively. The variable X is used to denote the single nuclear coordinate not integrated over. The element $\rho_{ij}^{\sigma}(t)$ of the density matrix for the link between sites $\mathbf{x}_i$ and $\mathbf{x}_j$ and the quantity $\tilde{\rho}_{ij}^{\sigma}(t)$ are defined by

$$\rho_{ij}^{\sigma}(t) = \sum_{r_2,\ldots,r_n} \int dR \, \psi^*(\mathbf{x}_i\sigma, r_2, \ldots, r_n, R, t)\psi(\mathbf{x}_j\sigma, r_2, \ldots, r_n, R, t) \tag{B.4a}$$

$$\tilde{\rho}_{ij}^{\sigma}(t) = \sum_{r_2,\ldots,r_n} \int dR \, H_{ij}^{int}(\mathbf{R})\psi^*(\mathbf{x}_i\sigma, r_2, \ldots, r_n, R, t)\psi(\mathbf{x}_j\sigma, r_2, \ldots, r_n, R, t). \tag{B.4b}$$

The solution of the Schrödinger equation provides the wavefunction at each $t \geq t_0$ and so gives a unique a mapping $\{\psi_0, T_{ij}^{ext}, V_n^{ext}\} \rightarrow \{\psi, Q_{ij}, \Gamma(\mathbf{X})\}$, where Q_{ij} and $\Gamma(\mathbf{X})$ are respectively the spin averaged electronic current and nuclear density. To define a current density functional theory (CDFT) for this system we want to prove the existence and uniqueness of the inverse mapping, which is done below.

To simplify notation in the following we assume $R = \{\mathbf{X}\zeta, R_2, \ldots, R_N\}$. Taking the derivative of the nuclear probability density with respect to time, and using the Schrödinger equation, we find

$$\begin{aligned}
\frac{\partial\Gamma(\mathbf{X})}{\partial t} &= \sum_{r\zeta} \int \prod_{i=2}^{N} dR_i \left[\psi^*(r,R)\frac{\partial\psi(r,R)}{\partial t} + \frac{\partial\psi^*(r,R)}{\partial t}\psi(r,R)\right] \qquad \text{(B.5)}\\
&= \sum_{r\zeta} \int \prod_{i=2}^{N} dR_i \sum_{j} \left[\frac{i}{2m}\psi^*(r,R)\nabla_{\mathbf{R}_j}^2\psi(r,R) - \frac{i}{2m}\nabla_{\mathbf{R}_j}^2\psi^*(r,R)\psi(r,R)\right]\\
&= \sum_{r\zeta} \int \prod_{i=2}^{N} dR_i \left[\frac{i}{2m}\psi^*(r,R)\nabla_{\mathbf{X}}^2\psi(r,R) - \frac{i}{2m}\nabla_{\mathbf{X}}^2\psi^*(r,R)\psi(r,R)\right]\\
&= \sum_{r\zeta} \int \prod_{i=2}^{N} dR_i \, \frac{1}{2m}\nabla_{\mathbf{X}}\left[i\psi^*(r,R)\nabla_{\mathbf{X}}\psi(r,R) - i\nabla_{\mathbf{X}}\psi^*(r,R)\psi(r,R)\right]\\
&= -\frac{1}{2m}\nabla_{\mathbf{X}} \sum_{r\zeta} \int \prod_{i=2}^{N} dR_i \, \mathrm{Im}\left[\psi^*(r,R)\nabla_{\mathbf{X}}\psi(r,R)\right].
\end{aligned}$$

From the first to the second row we have used the Schrödinger equation and the fact that all terms in the Hamiltonian cancel when the two terms are added, except for the kinetic energy. From the second to third row we have integrated by parts to get zero for all variables except $\mathbf{X}$. We now take the second time derivative of Γ which gives

$$\begin{aligned}
\frac{\partial^2\Gamma(\mathbf{X})}{\partial t^2} &= -\frac{1}{2m}\nabla_{\mathbf{X}}\sum_{r\zeta}\int\prod_{i=2}^{N}dR_i\,\mathrm{Im}\left[\psi^*(r,R)\nabla_{\mathbf{X}}\frac{\partial\psi(r,R)}{\partial t}+\frac{\partial\psi^*(r,R)}{\partial t}\nabla_{\mathbf{X}}\psi(r,R)\right]\\
&= -\frac{1}{2m}\nabla_{\mathbf{X}}\sum_{r\zeta}\int\prod_{i=2}^{N}dR_i\,\mathrm{Im}\Bigg[\frac{i}{2m}\sum_j\left(\psi^*(r,R)\nabla_{\mathbf{X}}\nabla^2_{\mathbf{R}_j}\psi(r,R)-\nabla^2_{\mathbf{R}_j}\psi^*(r,R)\nabla_{\mathbf{X}}\psi(r,R)\right)\\
&\quad - i\nabla_{\mathbf{X}}V_n^{ext}|\psi(r,R)|^2 - i\sum_{jk}\nabla_{\mathbf{X}}V(\mathbf{R}_j,\mathbf{R}_k)|\psi(r,R)|^2\\
&\quad - i\sum_{jk}\nabla_{\mathbf{X}}H^{int}_{jk}(\mathbf{R})\psi^*(r,R)\psi(\{\mathbf{r}_j\to\mathbf{r}_k\},R)\Bigg]\\
&= -\frac{1}{2m}\nabla_{\mathbf{X}}\sum_{r\zeta}\int\prod_{i=2}^{N}dR_i\,\mathrm{Im}\Bigg[\frac{i}{2m}\nabla_{\mathbf{X}}\left(\nabla_{\mathbf{X}}\psi^*(r,R)\nabla_{\mathbf{X}}\psi(r,R)-\psi^*(r,R)\nabla^2_{\mathbf{X}}\psi(r,R)\right)\\
&\quad - i\sum_{jk}\nabla_{\mathbf{X}}V(\mathbf{R}_j,\mathbf{R}_k)|\psi(r,R)|^2 - i\sum_{jk}\nabla_{\mathbf{X}}H^{int}_{jk}(\mathbf{R})\psi^*(r,R)\psi(\{\mathbf{r}_j\to\mathbf{r}_k\},R)\Bigg]\\
&\quad + \frac{1}{2m}\nabla_{\mathbf{X}}\left(\Gamma(\mathbf{X})\nabla_{\mathbf{X}}V_n^{ext}(\mathbf{X})\right)\\
&= \frac{1}{2m}\nabla_{\mathbf{X}}\left[F(\mathbf{X})+H(\mathbf{X})\right]+\frac{1}{2m}\nabla_{\mathbf{X}}\left[\Gamma(\mathbf{X})\nabla_{\mathbf{X}}V_n^{ext}(\mathbf{X})\right] \qquad \text{(B.6)}
\end{aligned}$$

In the first row we have used the Schrödinger equation to replace the time derivatives, and only included the terms that don't cancel in the sum of the two terms. Next we have integrated by parts all derivatives that are not with respect to $\mathbf{X}$, and used the fact that only the part of V_n^{ext} depending on $\mathbf{X}$ survives and can be taken out of the integral. Lastly we have collected all terms diagonal in the electronic coordinates in the function F and called the remaining term H. These are explicitly given by

$$\begin{aligned}
F(\mathbf{X}) &= \sum_{r\zeta}\int\prod_{i=2}^{N}dR_i\,\mathrm{Im}\Bigg(\frac{i}{2m}\nabla_{\mathbf{X}}\left[\psi^*(r,R)\nabla^2_{\mathbf{X}}\psi(r,R)-\nabla_{\mathbf{X}}\psi^*(r,R)\nabla_{\mathbf{X}}\psi(r,R)\right]\\
&\qquad + i|\psi(r,R)|^2\sum_{jk}\nabla_{\mathbf{X}}V(\mathbf{R}_j,\mathbf{R}_k)\Bigg) \qquad \text{(B.7)}\\
H(\mathbf{X}) &= \sum_{r\zeta}\int\prod_{i=2}^{N}dR_i\,\mathrm{Im}\left(i\sum_{jk}\nabla_{\mathbf{X}}H^{int}_{jk}(\mathbf{R})\psi^*(r,R)\psi(\{\mathbf{r}_j\to\mathbf{r}_k\},R)\right) \qquad \text{(B.8)}
\end{aligned}$$

As will be discussed in more detail below we can in the case where these functions are assumed to be continuous in $\mathbf{X}$ solve Eq. B.6 for the external potential V_n^{ext}, which defines a functional $V_n^{ext}[\psi, \Gamma]$ of the instantaneous wavefunction and the nuclear probability density. Also the equation defining the complex electronic current can be inverted to give the external field T_{ij}^{ext} as a functional of the current and the wavefunction, $T_{ij}^{ext}[\psi, Q_{ij}]$. Using these functional expressions in the Schrödinger equation we obtain a non-linear equation [27] of the form

$$i\frac{\partial}{\partial t}\psi(r, R, t) = H[Q, \Gamma, \psi]\psi(r, R, t). \tag{B.9}$$

To show that this equation has a unique solution we follow the argument in [27] and split the Hamiltonian into two parts where the second carries all time dependence, $H(t) = H_0 + H_1(t)$. With this separation we can use the method of integrating factor to reformulate the non-linear Schrödinger equation as an integral equation of the general form

$$u(t) = w(t, t_0)u(t_0) + \int_{t_0}^{t} dsw(t, s)K_s(u(s)), \tag{B.10}$$

where in our case the propagator is $w(t, s) = e^{-iH_0(t-s)}$ and the kernel $K_s(u(s)) = H_1(s)u(s)$. The general theory of PDE guarantees the existence of a unique solution to this equation as long as $w(t, s)$ and $K_s(u(s))$ are continuous functions of time and $K_s(u(s))$ is locally Lipschitz in the argument u. These conditions are obviously satisfied for w, and will hold for K as long as the functional dependencies of the external fields T_{ij}^{ext} and V_n^{ext} on Q and Γ are well defined and continuous in time [27]. From the relation

$$T_{ij}^{ext}(t) = \frac{Q_{ij}(t) - \tilde{\rho}_{ij}(t)}{\rho_{ij}(t)} \tag{B.11}$$

we see that the condition $|\rho_{ij}(t)| \neq 0$ is sufficient for $T_{ij}^{ext}[\psi, Q_{ij}]$. To see if we need to impose any further restrictions we invert Eq. B.6 for the field V_n^{ext} and integrate from $-\infty$ to $\mathbf{X}$ to obtain

$$\Gamma(\mathbf{X})\nabla_{\mathbf{X}} V^{ext}(\mathbf{X}) = F(\mathbf{X}) + H(\mathbf{X}) - 2m\int_{-\infty}^{\mathbf{X}} \frac{\partial^2 \Gamma(\mathbf{Z})}{\partial t^2} d\mathbf{Z}, \tag{B.12}$$

where we have used that Γ,F and H vanish at $-\infty$. This equation has a continuous solution as long as $|\Gamma(\mathbf{X})| \neq 0$ and $\ddot{\Gamma}(\mathbf{X})$ is continuous. We thus arrive at the following theorem:

Theorem (Existence of TDCDFT for electron-nuclear system). *Let $Q_{ij}(t)$ be a complex continuous function of time and $\Gamma(\mathbf{X}, t)$ be a continuous function with a continuous second derivative with respect to time. Further let Ω be a subspace of the Hilbert space where $|\rho_{ij}(t)|$*

and $|\Gamma(\mathbf{X})|$ *are strictly positive. Given an initial state* ψ_0 *of the system such that* $Q_{ij}(t)$ *and* $\Gamma(\mathbf{X}, t)$ *can be found from Eq. B.3, there is an interval around* t_0 *where the equation*

$$i\frac{\partial}{\partial t}\psi(r, R, t) = H[Q, \Gamma, \psi]\psi(r, R, t).$$

has a unique solution $\psi \in \Omega$*, and so there exists a unique mapping* $\{\psi_0, Q_{ij}, \Gamma(\mathbf{X})\} \to \{\psi, T_{ij}^{ext}, V_n^{ext}\}$*. If the solution is not global in time, it has reached the boundary of the region* Ω*, meaning either* $|\rho_{ij}(t)|$ *or* $|\Gamma(\mathbf{X}, t)|$ *have become zero.*

Proof. The existence of a local solution follows from the argument above the theorem. That the breakdown of a solution is due to its approach of the boundary of Ω follows from the general theorem saying that either this is the case or the solution has become unbounded. Since the wavefunction is normalized at all times, it is always bounded, so only the first option is left. □

Since the argument above is independent of the structure of the electron-electron and nuclear-nuclear interaction, it carries through also when both these are put to zero. If it is possible to find a non-interacting state ψ_0 that gives the correct ground state complex electronic current and nuclear probability density, the theorem therefore guarantees at least locally the existence of a time-dependent Kohn-Sham system.